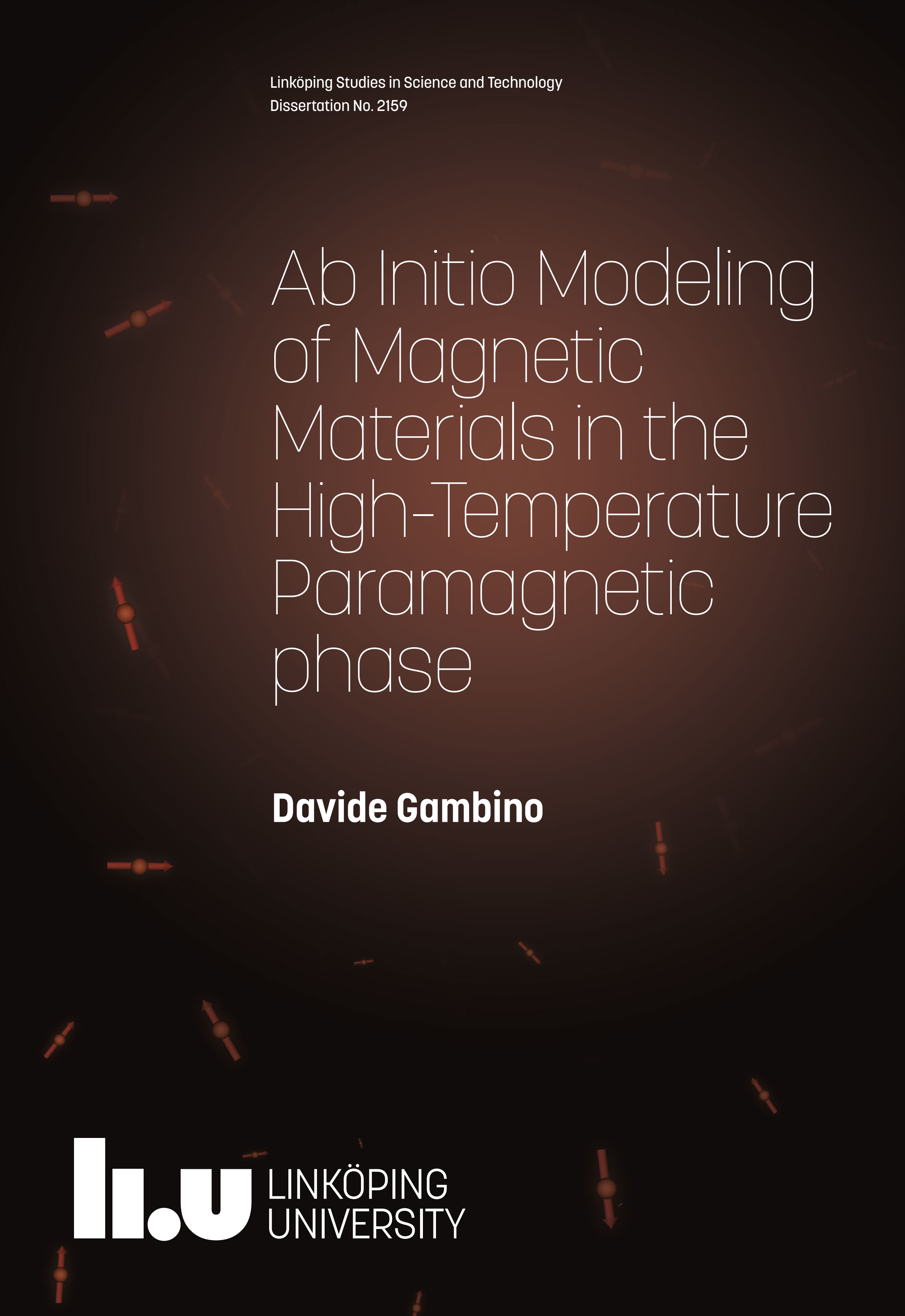

Linköping Studies in Science and Technology
Dissertation No. 2159

Ab Initio Modeling of Magnetic Materials in the High-Temperature Paramagnetic phase

Davide Gambino

LINKÖPING
UNIVERSITY

Linköping Studies in Science and Technology
Dissertations, No. 2159

Ab Initio Modeling of Magnetic Materials in the High-Temperature Paramagnetic Phase

Davide Gambino

Linköping University
Department of Physics, Chemistry and Biology
Theoretical Physics Division
SE-581 83 Linköping, Sweden

Linköping 2021

Front cover: Art work representing atoms with magnetic moments, by Mia Shu (www.miashu.com).

This work is licensed under a Creative Commons Attribution-NonCommercial 4.0 International License.
https://creativecommons.org/licenses/by-nc/4.0/

© Davide Gambino, 2021
ISBN 978-91-7929-003-0
ISSN 0345-7524
Published articles have been reprinted with permission from the respective copyright holder.
Typeset using LaTeX

Printed by LiU-Tryck, Linköping 2021

"Nothing in life is certain except death, taxes
and the second law of thermodynamics"
Seth Lloyd

Abstract

The modeling of magnetic materials at finite temperatures is an ongoing challenge in the field of theoretical physics. This field has strongly benefited from the development of computational methods, which allow to predict material's properties and explain physical effects on the atomic scale, and are now employed to direct the design of new materials. However, simulations need to be as accurate as possible to give reliable insights into solid-state phenomena, which means that, most desirably, all competing effects occurring in a system at realistic conditions should be included. This task is particularly difficult in the modeling of magnetic materials from first principles, due to the quantum nature of magnetism and its interplay with other phenomena related to the atomic degrees of freedom. The aim of this thesis is therefore to develop methods that enable the inclusion of magnetic effects in finite temperature simulations based on density functional theory (DFT), while considering on the same footing vibrational and structural degrees of freedom, with a particular focus on the high-temperature paramagnetic phase. The type of couplings investigated in this thesis can be separated in two big categories: interplay between magnetism and structure, and between magnetism and vibrations.

Regarding the former category, I have tried to shine some light on the effect of the paramagnetic state on atomic positions in a crystal in the presence of defects or for complicated systems, as opposed to the ordered magnetic state. To model the high-temperature paramagnetic phase of magnetic materials, the disordered local moment (DLM) approach is employed in the whole work. In this framework, I have developed a method to perform local lattice relaxations in the disordered magnetic state, which consists of a stepwise partial relaxation of the atomic positions, while changing the configuration of the magnetic moments at each step of the procedure. This method has been tested on point defects in paramagnetic bcc Fe, namely the single vacancy and, separately, the C interstitial in octahedral position, and on $Fe_{1-x}Cr_x$ alloys, finding non-negligible effects on formation energies. In addition, the feasibility of investigating extended defects like dislocations in the paramagnetic state with this method has also been proven by studying the screw dislocation in bcc Fe. The DLM-relaxation method has then been used to investigate intrinsic and extrinsic defects in CrN, an antiferromag-

netic semiconductor studied for thermoelectric applications, found in the paramagnetic state at operating temperature, and a newly synthesized compound, Fe_3CO_7, which features a complicated crystal structure and unusual electronic properties, with possible important implications for the chemistry of Earth's mantle.

The other focus of this thesis is the coupling between magnetism and lattice vibrations. As a pre-step to perform fully coupled atomistic spin dynamics-ab initio molecular dynamics (ASD-AIMD) simulations, I have first investigated the effect of vibrations on the so called longitudinal spin fluctuations, a mechanism occurring at finite temperatures and important for itinerant electron magnetic systems. I have developed a framework to investigate the dependence of the local moment's energy landscapes on the instantaneous positions of the atoms, testing it on Fe at different temperature and pressure conditions. This study has laid the foundation to apply machine learning techniques to the prediction of the energy landscapes during an ASD-AIMD simulation. Finally, I have investigated the phase stability of Fe at ambient pressure from the theoretical Curie temperature up to its melting point with ASD-AIMD. This task is carried out by applying a pool of thermodynamic techniques to calculate free energy differences, and therefore I have defined a strategy to discern the thermodynamic equilibrium structure in magnetic materials in the high temperature paramagnetic phase based on first principles dynamical simulations.

The methodologies developed and applied in this work constitute an improvement towards the simulation of magnetic materials accounting for the coupling of all effects, and the hope is to bridge a gap between theory and experiments.

Populärvetenskaplig sammanfattning

“Om du håller i två magneter och för dem samman så kan du känna ett tryck mellan dem. Vänd dem åt andra hållet och de smäller ihop. Vad är detta, den känslan mellan de två magneterna?" Frågan ställdes till den berömda fysikern Richard Feynman i en intervju[1] i samband med ett populärvetenskapligt TV-program som sändes 1983. Svaret som gavs när intervjun led mot sitt slut var: “Men jag kan verkligen inte göra ett bra jobb, på något sätt, om jag ska försöka förklara magnetisk kraft i termer av något annat som du är mer bekant med [...]". Att Feynman vägrar att förklara effekten - vilket han också noggrant redogör för under intervjun - beror på att förklaringen av hur två magneter interagerar med varandra rör sig igenom flera nivåer av komplexitet, där varje ny nivå leder till en ny “varför"-fråga. För att ge ett svar utifrån den djupaste nivån i denna trappa av “varför"-frågor krävs en förklaring av den (elektro)magnetiska kraftens ursprung. Denna kraft är en av de grundläggande krafterna inom fysiken, och en förklaring av den är omöjlig utan kunskap om mycket avancerade fysikaliska teorier. Olika intressanta fenomen kan däremot förklaras utifrån vart och ett av stegen i trappan. Därför krävs det lyckligtvis inte att vi går på djupet med fysikens grundläggande krafter för att introducera denna avhandling som syftar till att utveckla lämpliga metoder för att med datorsimuleringar beskriva magnetiska material på atomnivå.

Ett vanligt vetenskapligt tillvägagångssätt för att undersöka ett specifikt fenomen är att utgå från ett visst steg i “varför"-trappan och ta allt under denna nivå för givet. Från ett sådant antagande fortsätter en med olika approximationer som bortser från sådant som anses vara irrelevant för att förklara den effekt som undersöks. För de beskrivningar av magnetiska material som är relevanta för denna avhandling är det huvudsakliga antagandet att elektroner beter sig som mikroskopiska magneter. Elektroner är en av huvudingredienserna i de atomer som bygger upp fasta ämnen, och de är också “limmet" som håller atomerna samman. I vissa specialfall samverkar elektronerna på så sätt att det magnetfält de genererar sammantaget bildar så kallade atommagnetiska moment, vilka i sin tur ger upphov till materials magnetiska egenskaper. I detta skede kan vi därför anta att magnetiska atomerna i fasta ämnen utgör den minsta magnetiska beståndsdelen, och därmed för tillfället strunta i de individuella elektronerna. För att underlätta illustrationen av ett sådant system kan de magnetiska momenten föreställas som pilar. Pilarnas riktning indikerar riktningen hos det magnetfält som genereras av motsvarande atom, och deras storlek indikerar fältets styrka.

---

[1] https://www.youtube.com/watch?v=wMFPe-DwULM

För att förstå avhandlingens ämnesområde är det fördelaktigt att utföra ett tankeexperiment och föreställa sig vad som händer med ett magnetiskt material vid en temperaturförändring. Föreställ dig exempelvis en bit järn - ett av de mest välkända fasta magnetiska ämnena - och föreställ dig vidare att du kyler ner den till en mycket låg temperatur (mycket lägre än 0°C) under påverkan av ett magnetfält. Om det yttre magnetfältet i detta läge stängs av så kommer järnbiten att vara magnetiserad, det vill säga den genererar sitt eget magnetfält. Om temperaturen därefter sakta höjs förblir magnetiseringen av järnprovet mer eller mindre konstant tills dess att vi når en viss temperatur (cirka 770°C) när den plötsligt försvinner. Over denna temperatur sägs systemet vara i det paramagnetiska tillståndet (eller fasen) vilket innebär att det förlorar sin förmåga att spontant generera magnetfält. Det som sker på mikroskopisk nivå i detta (tanke)experiment är att vid låga temperaturer så pekar atomernas magnetiska moment (som vi föreställt oss som pilar enligt ovan) i samma riktning vilket ger upphov till en övergripande magnetisering. Ett system som järn - med en sådan konfiguration av de magnetiska momenten vid låga temperaturer - sägs vara ferromagnetiskt. Och den fas där systemet har förmågan att generera ett magnetfält kallas motsvarande för den ferromagnetiska fasen. Med ökande temperatur börjar momenten pendla i riktning. Till att börja med är dessa svängningar små och har ingen stark påverkan på provets övergripande magnetisering. Ju högre temperatur, desto starkare blir svängningarna, tills vi når den punkt där de magnetiska momenten befinner sig i total oordning i förhållande till varandra. På lokal atomnivå kan denna oordning beskrivas som en slät funktion med avseende på temperaturen. Om vi istället betraktar en makroskopisk nivå är effekten plötslig (vilket illustreras i tankeexperiement ovan).

Denna illustration av processen används ofta för att skildra den magnetiska övergången för ferromagnetiska system från ett tillstånd (ferromagnetiskt) till det andra (paramagnetiskt). Illustrationen fungerar förvånansvärt bra med tanke på att den bygger på antaganden om dels att atomerna är orörliga på fasta positioner, dels att pilarna som representerar de magnetiska momenten alltid har samma storlek. Som tidigare nämnts bygger vetenskapliga tillvägagångssätt ofta på antaganden och approximationer, och vetenskaplig utveckling består därmed ofta i att lyfta dessa approximationer. I ovanstående beskrivning är atomernas orörlighet den första approximationen som kan lyftas. I verkligheten vibrerar atomerna, och vibrationerna blir dessutom starkare med ökande temperatur. Dessa atomvibrationer kan påverka hur de magnetiska momenten interagerar med varandra, och omvänt kan interaktionen mellan momenten påverka hur atomerna vibrerar. För det andra kan de magnetiska momentens svängningar variera både i riktning (som illustrerats i tankeexperimentet) och i storlek. Den senare mekanismen - som inom fältet fasta tillståndets magnetism kallas longitudinella kvantfluktuationer - är mycket mer komplicerad än de tidigare beskrivna effekterna på grund av dess nära relation till elektronernas kvantnatur. Emellertid är de longitudinella kvantfluktuationerna, på samma sätt som svängningar i riktning, relaterade till temperaturförändingar, och de uppvisar även ett komplex samspel med atomvibrationerna. Slutligen har verkliga material alltid defekter i sin mikroskopiska struktur, och dessa defekters interaktion med de magnetiska momenten påverkar även materialets egenskaper på makroskopisk nivå.

De tre ovan beskrivna effekterna och deras intrikata och ömsesidiga samspel är huvudämnet i denna avhandling. Mitt fokus ligger på hur en kan inkludera dem i, och undersöka dem med, de datorsimuleringar som behövs för att lösa fysikaliska ekvationer vilka möjliggör förutsägelser av materialegenskaper. Metoderna som utvecklas i min forskning syftar till att förbättra beskrivningen av fasta magnetiska ämnen under realistiska förhållanden. Ambitionen är att sådana metoder ska göra det möjligt att förklara fenomen som förekommer under förhållanden som är svåra att undersöka i experiment, och därmed bidra till upptäckter av nya material med tekniskt användbara egenskaper. Min huvudsakliga motivation är dock att lägga en bit till det stora pussel som är fasta tillståndets magnetism. Jag hoppas att min forskning ska bidra till att förbättra svaret utifrån ett specifik steg i den “varför"-trappa som utgår från frågan “Vad är detta, den känslan mellan de två magneterna?"

Popular science summary

“If you get hold of two magnets, and you push them, you can feel this pushing between them. Turn them around the other way, and they slam together. Now, what is it, the feeling between those two magnets?" This question was asked to the famous physicist Richard Feynman in an interview[2] for a popular-science TV show in 1983. The final answer, which comes only towards the end of the interview, was: “But I really can’t do a good job, any job, of explaining magnetic force in terms of something else you’re more familiar with [...]". Feynman’s refusal of explaining this effect, as he thoroughly clarifies during the interview, is that the explanation of why two magnets interact with each other goes through several levels of complexity, where each level leads to a new “why" question. To give an answer at the deepest level of this ladder of “why" questions, one would need to explain the origin of the (electro)magnetic force, which is one of the fundamental forces of physics, and such an explanation is impossible to understand without knowledge of very advanced physical theories. However, different interesting phenomena are located at each step of the ladder. Fortunately, there is no need to go into the depths of the fundamental forces of physics to introduce this thesis, which is aimed at the development of methods to accurately describe magnetic materials on the atomic scale with computer simulations.

As is commonly done in science, in order to study a specific effect, one needs to start at a certain rung of the “why" ladder, taking for granted everything beneath this level. From this assumption, one then proceeds with approximations that neglect what is thought to be irrelevant to explain the effect under investigation. For the description of magnetic materials relevant to this thesis, the main assumption is that electrons behave as microscopic magnets. Electrons are one of the main ingredients of the atoms that compose solids, and they are also the “glue" that keeps the atoms together. In some special cases, the electrons interact with each other in a way so that the magnetic field they generate sum up to form the so-called atomic magnetic moments, giving rise to magnetic properties in materials. At this point, one can think of the magnetic atoms in the solid as the smallest magnetic unit, and momentarily forget about the electrons. To facilitate the illustration of these systems, the magnetic moments can be imagined as arrows. The direction of the arrows indicates the direction of the magnetic field generated by the corresponding atom, and the size indicates the strength of the field.

---

[2] https://www.youtube.com/watch?v=wMFPe-DwULM

For understanding the subject of this thesis, it is useful to perform a thought experiment by thinking about what happens to a magnetic material as temperature changes. As an example, consider a piece of iron, one of the most known magnetic solids, and imagine cooling it down to very low temperature (much lower than 0°C) under the effect of a magnetic field. At this point, if the external magnetic field is turned off, the iron sample is found to be magnetized, i.e., it generates its own magnetic field. If the temperature is now slowly increased, the magnetization of the sample remains more or less constant up to a certain temperature, around 770°C, when it suddenly disappears. Above this temperature, the system is said to be in the paramagnetic state or phase, which means that it has lost its ability to spontaneously generate magnetic fields. What is happening on the microscopic scale in this experiment is that, at low temperatures, the magnetic moments of the atoms (represented with the arrows described earlier) are all pointing in the same direction, therefore giving rise to an overall magnetization. A system like iron, having such an arrangement of the magnetic moments at low temperatures, is said to be ferromagnetic. The phase in which it has the ability to generate magnetic fields is correspondingly called the ferromagnetic phase. With increasing temperature, the moments start fluctuating in direction. Initially, these fluctuations are small, and there is no strong effect on the overall magnetization of the sample. The higher the temperature is, the stronger these fluctuations become, up to the point where the magnetic moments are completely disordered with respect to each other. On a local atomic scale, this disordering happens smoothly as a function of temperature, but on a macroscopic scale the effect is sudden, as illustrated in the thought experiment.

This illustration of the process is often used to the describe the magnetic transition of ferromagnetic systems from one state (ferromagnetic) to the other (paramagnetic), and it works surprisingly well even considering the assumption of the atoms as being still on fixed positions, and of the arrows representing the magnetic moments always being of the same size. However, as mentioned previously, science is based on assumptions and approximations, and the scientific progress often consists in lifting these approximations. In the previous description, a first approximation that can be lifted is the stillness of the atoms. In reality, atoms vibrate, and the vibrations become stronger with increasing temperature. These atomic vibrations can affect how the magnetic moments interact with each other and, vice versa, the interaction between moments can affect the way the atoms vibrate. Second, the fluctuations of the magnetic moments can be both in direction, as already described in the thought experiment, and in size. This latest mechanism is known in the field of solid-state magnetism as longitudinal spin fluctuations, and is much more complicated than the previously described effects, due to their close relation to the quantum nature of the electrons. Nonetheless, the longitudinal fluctuations, similarly to the fluctuations in direction, are related to changes in temperature and they can display as well a complicated interplay with vibrations. Finally, real materials always have defects in their microscopic structure, and the way these imperfections interact with the magnetic moments also affects the properties at the macroscopic scale.

The three competitions of effects just described and their intricate mutual influence is the main subject of this thesis. I focus on how to include them and investigate them with computer simulations that are needed to solve the physical equations that allow the prediction of materials properties. The methods developed in this work are aimed at improving the description of magnetic solids at realistic conditions. The ambition is that such methods will enable to explain phenomena occurring in conditions not reproducible by experiments, and help in the discovery of new materials with technologically useful properties. However, my main motivation is to add one piece to the puzzle of solid-state magnetism. I hope with my work I will contribute to the improvement of the answer to a specific rung in the “why" ladder starting from the question “what is it, the feeling between those two magnets?"

Preface

This doctoral thesis concludes my Ph.D studies carried out between 2017 and 2021 in the Theoretical Physics Division, Theory of Disordered Materials Unit, at the Department of Physics, Chemistry and Biology, Linköping University, Sweden. The introductory part of this thesis gives an overview of the theories and methods employed to study magnetic materials in their high-temperature paramagnetic phase with first principles techniques, followed by the main results from my own work regarding the interplay between magnetism and other degrees of freedom, namely structural and vibrational degrees of freedom. Extensive parts of these chapters are taken from my Licenciate Thesis (No. 1837, Linköping Studies in Science and Technology), published in 2019. During the course of research underlying this thesis, I was enrolled in Agora Materiae, a multidiciplinary doctoral program at Linköping University, Sweden.

Acknowledgments

No one can go through the long journey of the PhD studies alone; here I want to thank all those that helped me achieve this goal.

Not only because it is due, but because I really want to, I first must acknowledge my supervisor Björn Alling. You have been a true advisor, always putting my personal development first. I feel like I grew a lot in these four years and a half, both personally and academically, and I really need/want to thank you for this.

Many thanks to the Head of the Theoretical Physics Division Igor Abrikosov for initially offering me the opportunity to be part of this group, and to my co-supervisor Marcus Ekholm for the help and spontaneous projects that appeared on the way. I would like to thank all the members of the Theoretical Physics Division, in particular Johan K., Johan T., Johan J., Joel D. and Luis C., for sharing lively physics discussions, conference experiences (sorry for those) and more informal, very fun gatherings. A special mention to Davide S., who introduced me to the world of research quite a few years ago at this point: it is always a pleasure to discuss with you and see your passion in what you do!

To achieve a goal such as a PhD degree, one needs to disconnect every now and then from work. This task has been greatly achieved thanks to many, many people from the international community that gravitates around IFM, and beyond. Many people have passed in these years, and I will for sure forget to mention someone for which I am very sorry, nonetheless thanks to Anna-Giulia, Hassan, Andreas, Arnaud, Tim, Clio, Nikos, Alexis, Marius, Laurent, Claudia, Mattias, Nerijus, Lida, Judit, Johan, Julia, Ivan, Tejaswi, Karina, all the friends from the jam sessions, Sara, Camille, Nicolas, Jeby, Guillem, Daniel and Giacomo. I was definitely not a "dull boy" thanks to you all! Thanks a lot to Mia for helping me with the cover of this thesis, I would have never been able to produce such a beautiful thing on my own. A special thank to Toby, who helped me and supported me so much in these last months!

In addition, one needs to live somewhere, and I cannot think of a better way of living than with my amazing flatmates Marianne, Alex and Victor (and, of course, Bacon)! We have been through some tough times between work stress and the pandemic, but together we managed to survive them!

Infine, il mio riconoscimento piú grande va come sempre all mia famiglia. Gianlu, Marta, Gioelino e la nuova arrivata Emi, grazie mille! É quasi come non fossi mai partito. Ai miei genitori, che mi sono sempre stati vicini e mi hanno permesso di arrivare fino a questo traguardo, il merito di questa tesi é anche vostro!

Contents

Abstract iv

Populärvetenskap sammanfattning ix

Popular science summary xiii

Preface xv

Acknowledgments xviii

Contents xix

1 Introduction 1
- 1.1 Materials modelling with computer simulations 1
- 1.2 Modelling of solid state magnetism 2
- 1.3 The importance of defects 4
- 1.4 What is this thesis about 5

2 The electronic structure problem 7
- 2.1 The Schrödinger equation 8
- 2.2 Density Functional Theory 10
  - 2.2.1 Hohenberg-Kohn theorems 10
  - 2.2.2 Kohn-Sham ansatz 11
  - 2.2.3 Exchange and correlation term 12
  - 2.2.4 Some practical details 13
- 2.3 Spin-polarized DFT 13
  - 2.3.1 Constrained DFT: magnetic moments direction 14
- 2.4 Approximations to the exchange and correlation functional . . 15
  - 2.4.1 Strong correlations: the DFT+U approach 16
  - 2.4.2 The strongly constrained and appropriately normed (SCAN) functional 17

3 Statistical mechanics and thermodynamics 19
- 3.1 Partition function and thermodynamic potentials 20
- 3.2 Sampling the phase space 22

3.2.1 Ab initio molecular dynamics 22
3.2.1.1 Nonequilibrium molecular dynamics - Color Diffusion algorithm 24
3.2.2 Monte Carlo simulations 25
3.3 Free energy calculation 27
3.3.1 Thermodynamic integration (TI) 27
3.3.1.1 TI over temperature 28
3.3.1.2 Stress-strain TI 29
3.3.2 Thermodynamic perturbation theory (TPT) 31

4 Microscopic description of magnetism 33
4.1 Magnetism in the ground state 34
4.2 Magnetism at finite temperature 35
4.3 The generalized Heisenberg Hamiltonian 36
4.3.1 Calculation of transition temperature with the Heisenberg model 39
4.3.2 Longitudinal spin fluctuations 42
4.4 Disordered local moment approach 45
4.5 Spin dynamics and coupling with lattice vibrations 46

5 Structural disorder 51
5.1 Defects in crystalline materials 51
5.1.1 Point defects 52
5.1.2 Dislocations 55
5.2 Diffusion in bulk systems 57
5.2.1 Diffusion close to the melting point: Ti vacancy diffusion in TiN investigated with the color diffusion (CD) algorithm 58
5.2.2 Concerted migration in bcc Ti 58
5.3 Random alloys 59

6 Magnetic disorder coupled with structural and vibrational degrees of freedom 61
6.1 Local lattice relaxations in the paramagnetic phase 62
6.1.1 DLM relaxation 62
6.1.2 Application to defects in bcc Fe and to $Fe_{1-x}Cr_x$ 64
6.1.3 Intrinsic and extrinsic defects in CrN for thermoelectric applications 67
6.1.4 Fe_3CO_7 70
6.2 Coupling of magnetic disorder and vibrations 71
6.2.1 LSF on a vibrating lattice and prediction of LSF landscapes with a machine learning algorithm 72
6.2.2 Phase stability in Fe 76

7 Conclusions and outlook 83

Bibliography 87

8 List of included articles and contributions 99

9 Related, not included publications 103

Paper I 107

Paper II 123

Paper III 135

Paper IV 145

Paper V 155

Paper VI 169

Paper VII 179

Paper VIII 187

Paper IX 217

Paper X 245

Paper XI 261

1 | Introduction

Condensed-matter physics is one of the largest sub-fields of physics. Its birth can be traced back to the creation of the solid-state physics division in the American Physical Society in the mid 1940s [1], later on renamed condensed-matter physics division to include closely related non-solid systems and quantum many-body phenomena. Many physicists were initially skeptical about the definition of this field, since it was and still is very broad and involves previously defined disciplines of physics such as electromagnetism, optics and quantum physics, to name a few. The feeling at that time about this new field can be summarized with the words of Gregory Wannier: "Solid state physics sounds kind of funny" [1].

This thesis follows this tradition by investigating a broad range of systems and phenomena. Starting from the study of mass transport in technologically important materials, it passes through the characterization of compounds and elements present in the Earth's interior, to end with phase stability in Fe. Besides the fact that my contributions are based on computer simulations, the thread connecting all these investigations is the focus on "high" temperature, intended in this context as "high compared to some other reference temperature". Nonetheless, as the title of this thesis suggests, the main focus is magnetism at high temperatures. In particular, my aim is to improve the description of the paramagnetic phase in these conditions with computer simulations, in order to achieve a unified treatment of material systems that display disorder in magnetic as well as vibrational or structural degrees of freedom.

1.1 Materials modelling with computer simulations

The work presented in this thesis consists of a theoretical perspective on materials aided by the use of computer simulations. Computational methods, together with the formulation of fundamental theories, have greatly helped condensed matter theory. These methods enable solving the quantum-mechanical problem of electrons in a solid, at least approximately, and calculating the properties of materials with great insights at the atomic scale and at very short timescales. Currently, computer simulations are starting to drive the research and application of advanced functional materials [2], with the aim of predicting properties of unknown compounds [3] rather than just explaining phenomena in existing materials, as effectively achieved in the past decades [4].

The task of computational methods is two-fold. On the one hand, they enable numerically solving very complicated equations that we cannot solve in any other way; on the other hand, they allow us to sample very large spaces of possibilities, with these being simply the space of atomic positions and velocities at finite temperatures, or the chemical space consisting of compounds with exceptional properties.

The first task is related with the solution of the quantum problem for ions and electrons, for which computer code implementations of several different quantum-mechanical theories and methods at different levels of approximation are available[1]. In this context, density functional theory (DFT) [5, 6] has been the main workhorse in materials research for the past 30 years. Its success is based on the reformulation of the quantum-mechanical problem of N electrons, into the comparatively easy problem of an electron density (see Chapter 2), enabling the fast solution of Schrödinger's equation.

The second task instead is related more closely to the behavior of the atoms at finite temperatures, and it involves a collection of methods based on statistical mechanics [7]. Within this framework, in order to calculate properties, one needs to explore the so-called phase space of the system, *i.e.*, all the possible configurations of atomic positions and velocities, and magnetic moments when these are present. The main techniques that enable this exploration are Monte Carlo and molecular dynamics simulations, where the first is based on a stochastic sampling, and the second provides a realistic dynamics of the system. Which technique to use depends on the problem at hand, however assuming infinite simulation time, the two techniques give the same results for static properties.

The combination of quantum mechanical and statistical mechanics methods in computer simulations enables, in principle, the investigation of any material's property as a function of internal and external conditions. In particular, magnetism, defects and vibrations in crystalline and, on a smaller scale, liquid systems are the topics investigated in this thesis.

1.2 Modelling of solid state magnetism

When we think of a magnetic material, the first thing that might come to mind is a magnet such as the souvenirs that can be attached to the refrigerator. Magnets are fundamental in many applications, such as in generators, audio equipment and hard drives, for their ability of generating a permanent magnetic fields. However, magnetic materials are much more widespread than one could think. This is because they sometimes show excellent properties not directly related to magnetism. Steels are probably the best example of a material system belonging to this later category.

---

[1] `https://en.wikipedia.org/wiki/List_of_quantum_chemistry_and_solid-state_physics_software`

In general, all materials respond in some way to an applied magnetic field. The historical classification of the magnetic character of materials is based on their response to an applied magnetic field [8]: if they are slightly repelled by the field, they are called diamagnetic; if they are slightly attracted, they are called paramagnetic; if they are strongly attracted, they are called ferromagnetic. This classification is highly reductive, in fact many other types of magnetism occur in materials, and a more modern classification is based on the magnetic ordering at the microscopic scale, if such magnetic effect is present. As an example, magnetite (Fe_3O_4) is the oldest known permanent magnet [9], but it is not ferromagnetic, it is ferrimagnetic (see below).

To have an idea of the plethora of possible magnetic orderings at the microscopic scale, one can imagine that if an atom shows magnetic properties in a solid, the magnetic field it generates can be represented with a vector called magnetic moment. The magnetic moment is strongly related to the quantum nature of the electrons, in particular to their spin. The magnetic moments in a ferromagnetic material are all pointing in the same direction, which can lead to the generation of an external macroscopic magnetic field. In some other materials, the magnetic moments are coupled antiparallel to each other, with neighboring moments pointing in opposite directions. This type of ordering is called antiferromagnetic, and on a macroscopic scale such a material would not respond strongly to an external magnetic field as the local moments cancel each other out. The previously mentioned ferrimagnetic ordering is similar to the antiferromagnetic ordering, with moments coupled antiparallel to each other, however the moments in one direction are smaller than the moments in the other direction. A net magnetization arises from this imperfect compensation of magnetic moments, and therefore a strong response to magnetic fields is obtained. As one can imagine, from this description of a few possible types of magnetic ordering, many other can be constructed. As an example, the moments do not always need to be parallel or antiparallel to each other, but they can form many different noncollinear arrangements such as spirals, or waves, or they may even lack any ordering [10].

The above description is only fully valid in the lowest energy state, the *ground* state, which is in principle achievable at zero temperature, neglecting zero-point effects. The ground state can be difficult to determine with DFT, since for noncollinear orderings one needs a good initial guess about the arrangement of the moments. Further on, difficulties with the behavior of magnetism as a function of temperature are encountered. In general, one can assume that, with increasing temperature, the magnetic moments start fluctuating in direction and, possibly, in size, and above a certain critical temperature the long-range order is completely destroyed. This latest phase is known as paramagnetic, since it follows the behavior of paramagnetic systems of the old classification when subject to an external magnetic field. This is a difficult phase to model with DFT, due to the ground state nature of this method. However, one can implement knowledge from other theories, such as statistical mechanics, to include proper treatment of temperature effects on the magnetic fluctuations.

1.3 The importance of defects

Defects are all around. They can be both beneficial and disruptive. They come in different shapes and dimensionality. Their concentration can sometimes be controlled, and some other times not. Understanding the role of defects in affecting mechanical, electronic, magnetic and optical properties is central in technological applications.

One of the best examples of the use of defects in everyday life is in electronics. Silicon technology could not have been developed without a proper understanding and control of doping, *i.e.*, the controlled introduction of impurities in a crystalline structure. In this case, the impurities affect the semiconducting electronic properties of the silicon crystal, changing its ability to conduct currents; this effect is at the basis of the operation of any electronic circuit. Importantly, in order to produce this beneficial effect, defects need to be introduce in just the right amount, since, e.g., a too high concentration would lead to uncontrolled metallic-like conductivity and the breakdown of the electronic device.

Although the employment of defects in electronics might be the most well-known example, the effect defects have on mechanical properties such as hardness, toughness and brittleness can be found in many applications. As an example, steels in their most basic form are made of iron with some carbon impurities: after processing of the material, these impurities make steels much harder than pure iron. In addition, the one-dimensional defects known as dislocations control how materials behave in conditions of stress, allowing plastic deformations to take place and avoid fractures. However, other defects can lead to the opposite result: induce desired hardening or detrimental embrittlement of the material. An example of the latter is the effect of hydrogen impurities in many metals [11].

Defects are among the candidates for driving a new revolution in the field of quantum technology. As doping enabled the development of classical computing with silicon as a host, other types of defects in different host materials are currently investigated for the development of quantum devices that actively control quantum states of matter, one possible application of which is quantum computing [12]. These defects affect the optical properties of the system, similarly to what happens in colored diamonds. An example of a current research field related to this effect involves defects in silicon carbide [13], which are investigated as, for example, emitters of single photons.

The most important type of defect in this thesis is the vacancy, which consists of a missing atom in the regular structure of a crystalline solid. This type of defect is important because it occurs naturally, as a result of increasing temperature, and it may affect the mechanical properties of a material. In this context, vacancies are the main protagonist of diffusion in certain types of solids, a phenomenon that controls the internal state of a material. Therefore, knowledge of the influence of vacancies on mass transport is crucial due to, e.g., the involvement in most types of phase transitions [8].

1.4 What is this thesis about

The aim of this thesis is to explore the interplay between magnetism in solids, especially in the high-temperature paramagnetic phase, alongside other effects that occur in real applications and experiments. Historically, these interplays have been neglected, assuming that magnetism in solids could be treated as decoupled from the structure or vibrations.

As hinted by the previous sections, one of the main topics is the interplay between magnetism and crystal defects; together with this, the interplay between magnetism and the crystal structure itself is also a relevant topic. Another focus in this thesis is the coupling between magnetism and atomic vibrations at finite temperatures. Atomic vibrations are ubiquitous, and are particularly important at high temperatures, where magnetic systems are often in the paramagnetic state. The achievement of a proper treatment of these two effects in a unified framework is still ongoing research, and with my work I try to improve the simultaneous description of these effects in the same computer simulation. My research employs many different theories and methods with the aim of lifting approximations that treat magnetic and structural or vibrational disorder as decoupled phenomena.

This thesis starts with two chapters on basic theories that are widely employed in my simulations, the previously mentioned DFT (Chapter 2), and statistical mechanics and thermodynamics (Chapter 3). Methods and tools from these two chapters are extensively employed and referred to in the following chapters. In Chapter 4, the microscopic description of magnetism is presented, starting from the ground state and going to finite temperatures. Particularly important is here the modelling of the high-temperature paramagnetic phase of magnetic materials. Chapter 5 is concerned with defects in crystalline structures and random alloys. This chapter starts with a brief overview of the main defects investigated in this thesis and continues with a description of different mechanisms for diffusion in bulk systems. Chapter 6 combines concepts from all the previous chapters, and is mainly concerned with the coupling of magnetism with crystal structure, defects and vibrations. Finally, in Chapter 7, the conclusions of my work are drawn, and some possible future outlooks are indicated.

2 The electronic structure problem

The main laws of quantum mechanics needed to calculate the properties of atoms, molecules and materials have been established in the end of the 1920s [14]. Almost one hundred years later, we employ these laws every day to unravel new physical mechanisms and explain old ones, calculate properties of known and unknown compounds, and design new materials with outstanding features to be used in various technological applications. A leading role for this great advancement was played by the huge growth of computing power; however, the employment of computers in research is not solely responsible for our development of the understanding of matter. In fact, even with present supercomputers, solving the Schrödinger equation exactly for more than a few atoms [15] is practically impossible. Theories that allow to simplify these equations or devise new ways to solve them are needed, and the most used method in materials science is density functional theory (DFT) [2, 4]. DFT is in principle an exact method to solve the quantum mechanical problem of electrons in a solid; however, in practice, it involves the use of approximations which enables handling the many-body complications intrinsic to the Schrödinger equation.

In this chapter I will outline how the problem of electrons and nuclei in a solid is solved, starting from common underlying approximations to the Schrödinger equation and then moving to DFT. The discussion of DFT is initially carried out without accounting for the electron spin to make the notation easier, and in Sec. 2.3 I will explain how the theory is complemented with spin-polarization, which is fundamental in the investigation of magnetic materials. In addition, for the sake of clarity, I will discuss only the Schrödinger equation, although the Dirac equation should be used whenever electrons are involved.

2.1 The Schrödinger equation

The time-dependent Schrödinger equation for a collection of nuclei and electrons in a system is:

$$i\hbar\frac{\partial}{\partial t}\Psi(\{\mathbf{R}_I\},\{\mathbf{r}_i\},t) = \hat{H}\Psi(\{\mathbf{R}_I\},\{\mathbf{r}_i\}t), \tag{2.1}$$

where Ψ is the many-body wavefunction at time t for the whole system containing nuclei and electrons at positions $\mathbf{R}_I$ and $\mathbf{r}_i$, respectively, and $\hat{H}$ is the Hamiltonian for the system. In principle, knowledge of the full many-body wavefunction gives access to any property of the system. The Hamiltonian can be written in general (in atomic units) as:

$$\begin{aligned}\hat{H} = -\frac{1}{2}\sum_{i=1}^{n}\nabla_i^2 - \frac{1}{2}\sum_{I=1}^{N}\frac{1}{M_I}\nabla_I^2 - \sum_{i,I}\frac{Z_I}{|\mathbf{r}_i - \mathbf{R}_I|} + \frac{1}{2}\sum_{i\neq j}\frac{1}{|\mathbf{r}_i - \mathbf{r}_j|} + \\ + \frac{1}{2}\sum_{I\neq J}\frac{Z_I Z_J}{|\mathbf{R}_I - \mathbf{R}_J|} + \hat{V}(\mathbf{r},t).\end{aligned} \tag{2.2}$$

The terms here are, in order from left to right, the kinetic energy of the electrons (lowercase labels) and of the nuclei (capital labels), the attractive interaction between electrons and nuclei, the electron-electron and nucleus-nucleus repulsion, and a possible external potential, which can in general depend on space and time. M_I and Z_I are mass and charge of nucleus I, respectively.

If the Hamiltonian does not depend explicitly on time, the equation can be separated to obtain the time-independent Schrödinger equation:

$$\hat{H}\Psi(\{\mathbf{R}_I\},\{\mathbf{r}_i\}) = E\Psi(\{\mathbf{R}_I\},\{\mathbf{r}_i\}), \tag{2.3}$$

where E is the energy of the system and the time dependence has already been taken out. This equation can be solved analytically only for few systems[1], numerically for small molecules (see, *e.g.*, Ref. [16] and references [26-62] therein), and it can in no way be solved exactly for a real solid. In order to calculate anything from this equation, one needs to employ approximations to simplify the problem.

The first approximation that is commonly employed is the so-called Born-Oppenheimer approximation: since the mass of the electrons m_e is much smaller than the mass of the nuclei M_I, then as soon as the nuclei move, the relaxation of the electrons to their ground state is approximated to happen instantaneously . This consideration allows to partially separate the problem in two parts, one for the electrons and one for the nuclei, with the wavefunction becoming:

---

[1] A list of systems that can be solved analytically can be found on Wikipedia at this link: `https://en.wikipedia.org/wiki/List_of_quantum-mechanical_systems_with_analytical_solutions`

$$\Psi(\{\mathbf{R}_I\},\{\mathbf{r}_i\}) = \Phi(\{\mathbf{R}_I\})\psi(\{\mathbf{r}_i\};\{\mathbf{R}_I\}), \tag{2.4}$$

where the first wavefunction on the right hand side describes the nuclei and the second describes the electrons, with the latter depending parametrically on the nuclear positions $\{\mathbf{R}_I\}$. The Schrödinger equation can therefore be separated in two equations:

$$\begin{aligned} \hat{H}_{\mathrm{el}}\psi(\{\mathbf{r}_i\};\{\mathbf{R}_I\}) = & \left[-\frac{1}{2}\sum_{i=1}^{n}\nabla_i^2 - \sum_{i,I}\frac{Z_I}{|\mathbf{r}_i-\mathbf{R}_I|} + \frac{1}{2}\sum_{i\neq j}\frac{1}{|\mathbf{r}_i-\mathbf{r}_j|}\right. \\ & \left. +\frac{1}{2}\sum_{I\neq J}\frac{Z_I Z_J}{|\mathbf{R}_I-\mathbf{R}_J|}\right]\psi(\{\mathbf{r}_i\};\{\mathbf{R}_I\}) = E_{\mathrm{el}}\psi(\{\mathbf{r}_i\};\{\mathbf{R}_I\}); \end{aligned} \tag{2.5}$$

$$\hat{H}_{\mathrm{nuc}}\Phi(\{\mathbf{R}_I\}) = \left[-\frac{1}{2}\sum_{I=1}^{n}\frac{1}{M_I}\nabla_I^2 + E_{\mathrm{el}}\right]\Phi(\{\mathbf{R}_I\}). \tag{2.6}$$

These equations clarify the parametrical dependence of the electronic wavefunction (Eq. 2.5) and the dependence of the nuclear wavefunction on the electronic energy E_{el}, which enters in Eq. 2.6 as a potential energy term. Terms depending on the derivative with respect to nuclear positions of the electronic wavefunctions, which are small whenever there are no excited states close to the ground state, are neglected within this approximations. As it can be imagined, this last condition breaks down in the case of metals; nonetheless, the Born-Oppenheimer approximation is widely used also in these systems with good results. The repulsion between nuclei is included in the electronic energy because otherwise this expression becomes ill-defined due to divergences appearing (see Ref. [4] for a comprehensive explanation of this issue).

In the spirit of the Born-Oppenheimer approximation, it is also customary to calculate electronic properties with fixed atomic positions; although atoms are always moving, effects on properties related strictly to electrons are often well reproduced with this approximation.

If instead the thermal behavior of the atoms is under consideration one simplification to Eqs. 2.4 and 2.6 can be to consider the nuclei (or ions) as classical particles, so that the quantum problem has to be solved “only" for the electronic system. This approximation is widely employed in *ab initio* molecular dynamics (see next chapter), and it is motivated whenever the atoms in the system are “heavy"; in case of light atoms like H, or strong bonds like the C-C bond in graphene, nuclear quantum effects can be important, and more advanced and expensive methods such as path integral molecular dynamics [17, 18] are needed.

For what concerns the solution of the electronic problem for a crystalline solid, it is customary to consider the lattice as an infinite repetition of unit cells. Of course, real systems are not infinite, but they contain so many atoms that from the point of view of quantum mechanics, they can be considered as infinite; application of periodic boundary conditions in this context greatly simplifies the problem. Moreover, defects are always present in real materials (as mentioned in Sec. 1.3), therefore the lattice is not perfect; however, for the calculation of certain properties, there is no need to include defects in the model. Whenever this approximation is employed, Bloch's theorem comes at help to solve the problem of an electron in an infinite periodic solid taking into account only the primitive cell of the lattice. This theorem states that, for an electron i in a periodic potential (in this case due to the nuclei), its wavefunction ψ can be expressed as:

$$\psi(\mathbf{r}_i) = e^{i\mathbf{k}\cdot\mathbf{r}_i} u_{l\mathbf{k}}(\mathbf{r}), \tag{2.7}$$

where $\mathbf{k}$ is a reciprocal lattice vector, $\mathbf{r}_i$ is the position of the electron, l is the quantum number (band index) of the wavefunction, and $u_{l\mathbf{k}}(\mathbf{r})$ is a function with the periodicity of the potential. In common cases, we do not deal only with one electron, therefore one needs to know how to put together many of these single-particle wavefunctions for a system of interacting electrons.

Nonetheless, all these approximations do not yet enable to solve the Schrödinger equation for a solid.

2.2 Density Functional Theory

Thomas [19] and Fermi [20] in 1927 separately proposed a scheme to solve approximately the Schrödinger equation bypassing the problem of the many-body electronic wavefunction. Their main idea was to change the focus from the electrons as individual particles to the electronic density $n(\mathbf{r})$ at each point $\mathbf{r}$ in the solid . In this model, the electron density is assumed to be locally constant and the kinetic energy is taken as the kinetic energy of a homogeneous electron gas. This model fails quite badly to predict properties of molecules and materials, but it was a first step towards the birth of DFT, introducing the fundamental concept of electron density as the important physical quantity to calculate.

2.2.1 Hohenberg-Kohn theorems

The foundations of modern DFT were laid by Hohenberg and Kohn with their seminal paper [5] in which they proved that, for an electronic system under the action of an external potential V_{ext}, there is a one-to-one relation between the potential and the electron density n. In addition, the energy of the system is a universal functional of the electron density, $E[n]$, which can be found variationally.

Unfortunately, the Hohenberg-Kohn theorems do not provide any scheme to find the universal functional of the density. At this point, the only thing that can be said is that the energy functional $E[n]$ can be written as:

$$E[n] = T[n] + E_{\text{int}}[n] + \int d\mathbf{r}\, V_{\text{ext}}(\mathbf{r})n(\mathbf{r}) + E_{II}, \tag{2.8}$$

where T is the kinetic energy of the electrons, E_{int} is the electron-electron interaction, the integral expression (extended over all space) is the interaction of the electrons with the external potential V_{ext} due to the nuclei, and E_{II} is the repulsion between nuclei. This functional is not known in general, so that Eq. 2.8 is in fact useless as it is.

2.2.2 Kohn-Sham ansatz

Kohn and Sham suggested a practical scheme [6] to derive the functional in Eq. 2.8, based on the ansatz that we can calculate the properties of the real electronic system by taking into account an auxiliary system of noninteracting "electrons". The auxiliary system is subject to an effective potential V_{eff}, and it can be constructed such that the density of the independent electrons is the same as the density of the real electronic system. In this way, the many-body wavefunction for all the electrons can be written in terms of independent single-particle wavefunctions ψ_i, and one needs to solve a system of coupled equations [6]:

$$\left(-\frac{1}{2}\nabla_i^2 + V_{\text{eff}}\right)\psi_i = \varepsilon_i\psi_i, \tag{2.9}$$

where the single-particle wavefunctions ψ_i are related to the electron density by:

$$n(\mathbf{r}) = \sum_i |\psi_i(\mathbf{r})|^2. \tag{2.10}$$

Using this electronic density, one can derive an expression of the energy functional for the whole system:

$$E[n] = T_S[n] + \int d\mathbf{r}\, V_{\text{ext}}(\mathbf{r})n(\mathbf{r}) + E_{\text{Hartree}}[n] + E_{II} + E_{\text{xc}}[n], \tag{2.11}$$

with

$$T_S[n] = \frac{1}{2}\sum_i |\nabla_i\psi_i|^2, \tag{2.12}$$

$$E_{\text{Hartree}}[n] = \frac{1}{2} \int \int \mathbf{dr}\, \mathbf{dr}' \, \frac{n(\mathbf{r})n(\mathbf{r}')}{|\mathbf{r} - \mathbf{r}'|}. \tag{2.13}$$

From these equations the effective potential acting on the independent particles can now be recognized to be:

$$V_{\text{eff}} = V_{\text{ext}} + \frac{\delta E_{\text{Hartree}}}{\delta n(\mathbf{r})} + \frac{\delta E_{\text{xc}}}{\delta n(\mathbf{r})}. \tag{2.14}$$

The functional in Eq. 2.11 now contains the kinetic energy of the independent electrons T_S, the classical Coulomb interaction of the electron density with itself (E_{Hartree}), the interaction of the density with the external potential, the interaction between nuclei, and a last term which is called exchange and correlation functional. All effects that are not included in the independent particles approximation are collected in this term. In general, the first four terms can be calculated exactly; the last one, on the contrary, is unknown and one needs to find a good approximation to the exchange and correlation energy in order to predict properties.

2.2.3 Exchange and correlation term

The origin of the exchange and correlation term can be more clearly grasped by introducing the expression of the energy functional from Eq. 2.8 into Eq. 2.11, giving:

$$E_{\text{xc}}[n] = (T[n] - T_S[n]) + (E_{\text{int}}[n] - E_{\text{Hartree}}[n])\,. \tag{2.15}$$

As it can be seen from this expression, the terms missing in the energy functional due to the independent particle approximation come both from the kinetic energy and from the electronic repulsion. The physical interpretation of the exchange and correlation term can be explained by comparison of the properties of the real electrons and the independent particles: on the one hand, E_{xc} takes into account the Pauli exclusion principle, not included in the Hartree term since it considers only the electrostatic repulsion, and therefore partly neglects the interaction between electrons with same spin (the so called exchange); on the other hand, E_{xc} includes the Coulomb repulsion between electrons of opposite spin, which is partly included in the kinetic energy and partly in the electron-electron repulsion (correlation). Approximations to the exchange and correlation term will be treated in the Sec. 2.4.

As previously mentioned, this procedure to calculate the functional of the density is an ansatz: this means that there is no rigorous proof that a correspondence between the real interacting electron system and the auxiliary non-interacting system exist. However, the Kohn-Sham method has been widely used with success, and its better performances as compared to

Thomas-Fermi theory is in the fact that the kinetic energy of the electrons is not approximated as the homogeneous electron gas at every point in space, rather it is the actual kinetic energy of independent electrons, on top of which one adds exchange and correlation. In addition, this last term in the functional in Eq. 2.11 is usually small, therefore an approximated expression can give accurate results. It is known that some quantities cannot be reproduced by the Kohn-Sham method[4]; however, when inaccuracies are present, it is most often due to the employed approximation to the exchange and correlation functional.

2.2.4 Some practical details

Methods to practically solve the Kohn-Sham equations rely on expansion of the wavefunctions ψ_i in some basis set. In my work I have used plane-waves as basis, since they are highly compatible with the periodic nature of crystalline solids and Bloch's theorem.

In addition, the projector augmented wave (PAW) method [21] has been used to represent the single-particle wavefunctions. In this method, space is separated in two regions: an augmentation region around nuclei, and an interstitial region in between the atoms. In general, the wavefunction of valence electrons is fairly smooth in the interstitial region, but oscillates rapidly near the nuclei, due to orthogonality with the wavefunctions of core electrons. Therefore, an all-electron wavefunction must respect this rapid oscillations as well as the smooth part in the interstitial region. Smooth wavefunctions need less plane-waves to be well represented, and therefore they are preferred in order to speed up calculations. To achieve this compromise between efficiency and accuracy, the PAW method prescribes a transformation from the original wavefunctions to auxiliary ones, exemplified by the the following equation (Dirac notation is here used for simplicity in representing projections) [21]:

$$|\psi\rangle = \mathcal{T}|\tilde{\psi}\rangle = |\tilde{\psi}\rangle + \sum_m \left\{|\psi_m\rangle - |\tilde{\psi}_m\rangle\right\}\langle p_m|\tilde{\psi}\rangle, \tag{2.16}$$

where the projectors $\langle p_m|$ project the pseudo-wavefunction $\tilde{\psi}$ onto the original wavefunction ψ. Calculations are performed with the pseudo-wavefunctions, which coincide with the original ones in the interstitial region, and finally the results for the original wavefunctions are recovered by the inverse transformation $\mathcal{T}^{-1}$.

2.3 Spin-polarized DFT

In principle, all that is needed in DFT is the electron density. However, in calculations of magnetic systems, consideration of the electrons' spin is useful in order to obtain the magnetic solution of the problem at hand. Practically, the electron density is separated in a spin-up and a spin-down electron density, namely:

$$n(\mathbf{r}) = n^{\uparrow}(\mathbf{r}) + n^{\downarrow}(\mathbf{r}) \tag{2.17}$$

and all the equations are solved for the two spin-polarized densities separately; however, the full electron density n is still determining the properties of the ground state.

If noncollinear magnetic moments are to be employed in the calculations, the electron density can be represented in terms of a spin vector at every point in space, with elements defined by:

$$n^{\alpha\beta}(\mathbf{r}) = \left[n_{\mathrm{Tr}}(\mathbf{r})\delta_{\alpha\beta} + \vec{m}(\mathbf{r}) \cdot \vec{\sigma}^{\alpha\beta} \right] /2, \tag{2.18}$$

where α and β are spin indices, n_{Tr} is the total electron density and is obtained as the trace of this 2x2 matrix, $\vec{m}(\mathbf{r})$ is the magnetization density at every point in space, and $\vec{\sigma}^{\alpha\beta}$ represents a vector with components from the Pauli matrices. Employing this definition of electron density, the single-particle Hamiltonian becomes a 2x2 matrix:

$$H_{\mathrm{KS}}^{\alpha\beta} = -\frac{1}{2}\nabla^2 + V_{\mathrm{eff}}^{\alpha\beta}, \tag{2.19}$$

where the only nondiagonal term in the effective potential is the exchange and correlation term. In calculations, this procedure is carried out by finding the local axis of spin quantization and then using the spin-polarized exchange and correlation energy for that axis. In this framework, the magnetic moment associated to a particular atom is in general calculated by integration of the magnetization density within a sphere defined *a priori*.

Importance of noncollinearity in real systems is often attributed only to noncollinear ground state, arising from geometric frustration or competing interactions between magnetic moments, as well as more complex interactions such as Dzyaloshinskii–Moriya interactions [10]. However, at finite temperatures, models with noncollinear arrangement of the magnetic moments can give a good representation of, for example, experimental transition temperatures, therefore the role of noncollinear moments should be much more stressed within DFT calculations.

2.3.1 Constrained DFT: magnetic moments direction

It can be difficult to obtain a specific noncollinear arrangements of the moments as solutions of DFT calculations, therefore constraints are often needed to stabilize these configurations. In this work, a constrained formulation of DFT has been used in order to select the direction of the atomic magnetic moments. Constrained DFT consists in adding a Lagrange multiplier to the energy of the system, so that the obtained solution will minimize the energy subject to the constraint. The method used in this work to constrain the direction of the moments has been developed by Ma and Dudarev [22], in which a penalty energy E_I^p at site I is added to the DFT energy:

$$E_I^p = \sum_I \lambda_I |\mathbf{M}_I^F| - \mathbf{e}_I \cdot \mathbf{M}_I^F, \tag{2.20}$$

where λ_I is a Lagrange multiplier, $\mathbf{e}_I$ is a unit vector in the direction along which the moment has to be constrained, and $\mathbf{M}_I^F$ is the magnetic moment defined as:

$$\mathbf{M}_I^F = \int_{\Omega_I} d\mathbf{r}\, \mathbf{m}(\mathbf{r}) F_I(|\mathbf{r} - \mathbf{r}_I|). \tag{2.21}$$

Here, $\mathbf{m}(\mathbf{r})$ is the magnetization density at point $\mathbf{r}$, Ω_I is the atomic sphere, and $F_I(|\mathbf{r} - \mathbf{r}_I|)$ is a function that decreases monotonically to zero towards the boundary. With this method, the direction of the moments can be constrained at will, and it can be improved by increasing further and further the value of the Lagrange multiplier λ_I. In addition, within this formulation, it is less favorable for the magnetic moment to change sign maintaining the same direction, in contrast with other methods that do not penalize spin flips. It can also be shown that the obtained penalty energy tends to zero for increasing λ_S.

2.4 Approximations to the exchange and correlation functional

As mentioned in Sec. 2.2, the exchange and correlation functional is the approximated term in DFT which determines a limit to the accuracy of calculations.

Historically, the first approximation developed for the exchange and correlation energy is the local density approximation (LDA). Within this approximation, the electron density at each point is assumed to have exchange and correlation energy equal to that of a homogeneous electron gas. This is expressed as:

$$\begin{aligned} E_{\mathrm{xc}}^{\mathrm{LDA}} &= \int d\mathbf{r}\, n(\mathbf{r}) \epsilon_{\mathrm{xc}}^{\mathrm{hom}}(n(\mathbf{r})) \\ &= \int d\mathbf{r}\, n(\mathbf{r}) \left[\epsilon_{\mathrm{x}}^{\mathrm{hom}}(n(\mathbf{r})) + \epsilon_{\mathrm{c}}^{\mathrm{hom}}(n(\mathbf{r})) \right]. \end{aligned} \tag{2.22}$$

The exchange energy for a homogeneous electron gas is here calculated analytically, whereas the correlation energy has to be calculated numerically with higher-level theory methods. The first quantitatively accurate calculation of $\epsilon_{\mathrm{c}}^{\mathrm{hom}}$ was performed by Ceperley and Alder [23] with quantum Monte Carlo calculations.

Despite the crude approximation, the LDA functional is often capable of capturing the correct main features of solid systems, and it is still used at times. What makes LDA capable of capturing at least trends in properties is the fact that it is based on a real electronic Hamiltonian: for this reason, it satisfies constraints regarding the properties of the exchange and correlation hole [4]. In addition, only the spherical average of the exchange and correlation hole enters the energy, so that detailed knowledge of its shape is not needed.

The obvious way to improve the exchange and correlation functional is to include the gradient of the electron density; however this has been historically more difficult than expected. The problem is that gradients of the density can be very large in real materials [4], so that a simple power expansion breaks down; therefore, a generalized gradient approximation (GGA) has to be used, imposing the expected behavior at large gradients. GGA functionals, in particular the formulation by Perdew, Burke, and Ernzerhof (PBE) [24], have lead to great improvements compared to LDA, especially in the calculation of equilibrium volumes and atomization energies of molecules [24]. GGAs are semi-local functionals, because they require the density in an infinitesimal neighborhood of $\mathbf{r}$ in order to get derivatives, in contrast to LDA which requires the density only at $\mathbf{r}$, therefore is local.

Since then, the quest to develop improved exchange and correlation functionals has continued: the final functional should reach chemical accuracy (1 kcal/mol=0.044 eV/formula unit) [25] as compared to experimental results. A way to improve the functionals is by designing them such that they satisfy as many exact constraints [26] as possible. Following this approach, the improvement to GGAs is represented by meta-GGA functionals, which include also the electron kinetic energy density. This term is related to the second derivative of the electron density, and meta-GGAs are designed to satisfy limits of this quantity. Further improvements include exact exchange and compatible or exact partial correlation in the approximated term, but they are often too computationally expensive for extensive investigations, although recent advances are making feasible the employment of these methods for more complicated calculations [27]. For what concerns meta-GGAs, they are comparable in terms of cost with semilocal functionals, but they often provide a better description of electron correlation because of the direct inclusion of the kinetic energy density in the functional.

2.4.1 Strong correlations: the DFT+U approach

LDA and GGAs are known to describe badly some 3d and 4f elements in strongly correlated compounds because they are not able to reproduce the localization of these orbitals. A simple method [28–30] that has been devised to make this problem less serious is the so called ”DFT+U” approach, where an Hubbard-like U^{eff} term is added in the energy functional for localized orbitals:

$$E^{\text{DFT+U}} = E^{\text{DFT}} + \frac{U^{\text{eff}}}{2} \sum_{I,\sigma} \left[\left(\sum_{m_1} n^{I,\sigma}_{m_1,m_1} \right) - \left(\sum_{m_1,m_2} \hat{n}^{I,\sigma}_{m_1,m_2} \hat{n}^{I,\sigma}_{m_2,m_1} \right) \right], \quad (2.23)$$

where $\hat{n}^{I,\sigma}_{m_1,m_2}$ is the occupancy operator at site I with spin σ and orbital characters m_1 and m_2, with these latest indices depending on the orbital quantum number l for which the correction is added; in this term, a double-counting correction is also included. In practice, the U^{eff} term tends to localize electrons by adding an energy cost for an electron in an individually occupied state to jump onto another state which is already singly occupied, therefore keeping the electrons apart. The main effect of the U term is to split the energy levels of these orbitals, and often it is used to open an electronic bandgap in semiconductors or insulators that are predicted to be metals with conventional DFT. First principles methods to calculate U^{eff} for a specific system are available [31], however it is very common to employ a value of U^{eff} that gives a good fit to a certain property such as the bandgap, while reproducing well also other properties (like the equilibrium lattice parameter). In my work, I have employed this method for the 3d states of Cr in CrN, and for the 3d states of Fe in Fe_3CO_7.

2.4.2 The strongly constrained and appropriately normed (SCAN) functional

One of the most recent meta-GGAs that has been discussed quite widely is the strongly constrained and appropriately normed (SCAN) [32] functional, which is the only meta-GGA at this time that satisfies all the known constraints for this category of functionals. Tests [33] on materials based on main group compounds have shown that this functional improves greatly the description of phase stability and ground state properties, and also for transition metal compounds an improvement as compared to the GGA-PBE functional was observed. However, some issues with this last class of compounds was observed already short after the SCAN functional became available (Paper III, Ref. [33–35]).

In Paper III we showed the shortcomings of the SCAN functional in the description of ground state properties of the elemental ferromagnetic metals, *i.e.*, bcc Fe, fcc Ni, and hcp Co, and we compared with results from LDA and PBE calculations. In particular, for Fe, SCAN finds the right ground state as FM bcc Fe and improves slightly the equilibrium volume as compared to PBE; however, it predicts Fe to be a strong ferromagnet, with the majority-spin band fully occupied (see Fig. 2.1). The moments are best predicted by LDA at the experimental volume, although it severely underestimates the

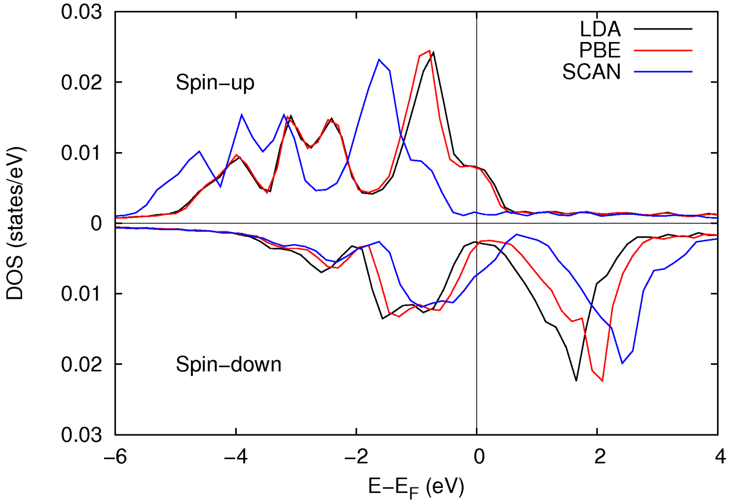

Figure 2.1: Electronic density of states (DOS) for FM bcc Fe as calculated with LDA, PBE, and SCAN functional at the experimental lattice parameter. The DOS for spin-up electrons, which are the majority spin carriers, is represented in the top part of the plot, spin-down in the bottom. Figure from Paper III.

equilibrium volume. For fcc Ni and hcp Co, SCAN does not give any kind of improvements as compared to PBE: it tends to underestimate the equilibrium volume and overestimate the magnetic moments. Also in these cases, SCAN shifts the majority-spin bands towards lower energies in the density of states (DOS).

Even though SCAN does not improve predictions as compared to PBE for elemental itinerant ferromagnets, it still provides an acceptable description of these systems. In Ref. [35], it has been shown that SCAN predicts Pd, which is a metal on the verge of ferromagnetism, to be a ferromagnet, whereas its ground state is nonmagnetic. This is a severe problem, and therefore magnetism should be a property to take more into account in the development of new exchange and correlation functionals.

3 Statistical mechanics and thermodynamics

Prediction of stable structures with exceptional properties at experimental conditions by means of *ab initio* calculations is one of the main goals of the electronic structure theory community. The machinery described in the previous chapter enables the calculation of ground state properties, which are in principle relevant only at zero temperature (neglecting zero-point effects). The ground state character of DFT seems to pose great limitations to the relevance of its results for everyday-life conditions; nonetheless, electronic excited states are often not important at equilibrium conditions, since thermal energies at temperatures of practical relevance are too small to cause dramatic changes in occupations or, more generally, to the electronic structure. Therefore, DFT is still able to provide reliable predictions if one is able to include in the calculations appropriate atomic thermal displacements, and evaluating the stability of different phases of a material becomes a reachable goal.

In some materials, however, excited electronic states are accessible just by thermal energy: as an example, in metallic systems or doped semiconductors, excited electronic states are at reach just by thermal excitations. Simple electronic finite temperature behavior can be included with the Mermin's functional [36] by including the proper smearing of the wavefunctions, allowing DFT to account for this degree of freedom. The other example of excited states related to electrons and relevant for this thesis involves magnetic degrees of freedom (DOFs), and inclusion of these phenomena in DFT calculations is the topic of Chapter 4.

In this chapter, instead, I will discuss how the thermal motion of atoms can be included in calculations, and how these results can be put together in the framework of thermodynamics and statistical mechanics to evaluate phase stability. The discussion starts from a brief description of the central quantities in thermodynamics, going then to the theoretical and computational methods that enable their calculation. All thermodynamics in this thesis is considered on a classical or semiclassical level.

3.1 Partition function and thermodynamic potentials

In thermodynamics, a system is usually considered under the effect of some constraint. These constraints define the *thermodynamic ensemble* that describes the system at equilibrium, consequently defining the natural variables for the specific situation. The ensembles relevant for this thesis are:

- Canonical ensemble (NVT): the system cannot exchange particles with the outside, and its temperature and volume are fixed. This ensemble is the most commonly simulated for technical reasons.
- Isothermal-isobaric ensemble (NPT): the system cannot exchange particles with the outside, and its temperature and pressure are fixed. This ensemble is often considered as representing experimental conditions for a bulk material.

Other ensembles can be defined, like the microcanonical ensemble (NVE) where number of particles, energy and volume are conserved, or the grand canonical ensemble (μVT) where the chemical potential, the volume and the temperature are conserved. In principle, the microcanonical ensemble would be the easiest ensemble to simulate, however there are some difficulties in maintaining fixed the energy, therefore it is often preferred to simulate the canonical ensemble, for which effective solutions to keep fixed the temperature are available. In the following, the main equations that allow to calculate properties in this ensemble are introduced.

In the canonical ensemble, all properties of the system can be in principle derived from the partition function Z which, for a discrete system, is defined as:

$$Z = \sum_i \exp\left(-\frac{E_i}{k_B T}\right), \tag{3.1}$$

and for a continuous system of N particles is :

$$Z = \frac{1}{N! h^{3N}} \int \exp\left(-\frac{E(\{\mathbf{x}_i\}, \{\mathbf{p}_i\})}{k_B T}\right) d\{\mathbf{x}_i\} d\{\mathbf{p}_i\}. \tag{3.2}$$

In these expressions, the energy E is defined by a label i in the case of a discrete particular microstate, or by the position and momentum of every particle in the system, $\{\mathbf{x}_i\}$ and $\{\mathbf{p}_i\}$ respectively. k_B is Boltzmann's constant, T the temperature, and h is Planck's constant.

The analytical calculation of this quantity is possible only in very simple cases; most often, one needs instead to efficiently explore a representative section of the *phase space* of the system, i.e., the space of all the possible combinations of particles positions and momenta. In the exploration of this space, one realizes that some configurations of $\{\mathbf{x}_i\}$ and $\{\mathbf{p}_i\}$ have a very high energy compared to the thermal energy; therefore, their Boltzmann factor

$\exp\left(-\frac{E(\{\mathbf{x}_i\},\{\mathbf{p}_i\})}{k_B T}\right)$, related to the probability of finding the system in these configurations, is going to be very low. A low Boltzmann factor also means that in equilibrium these configurations are not relevant for the properties of the system. Since the temperature is at the denominator in the exponential, it can be understood that at high temperatures many more microstates become accessible than at low temperatures. Methods to explore efficiently these relevant configurations are available and they will be described in the next section.

The thermodynamic potential that defines equilibrium in the canonical ensemble is the Helmholtz free energy F, in this thesis often referred to simply as free energy, which is given by:

$$F = E - TS = -k_B T \log(Z), \tag{3.3}$$

where E is the total energy of the system, S is the entropy, k_B is the Boltzmann's constant, and Z is the partition function. The equilibrium phase of the system is the one with the lowest free energy, which means that, at a given temperature T, the most favored state is the one with a balance between lowest total energy and highest entropy at the same time. All thermodynamic quantities can be derived from knowledge of the partition function of a system, and therefore from knowledge of F.

In the calculation of free energies, it is common to take advantage of the fact that different DOFs evolve at different time scales. As an example, for a magnetic material, it is often assumed that electronic DOFs are much faster than magnetic ones, which in turn are faster than vibrational ones, so that the free energy can be separated in different contributions:

$$F(V,T) = E_{0\mathrm{K}}(V) + F^{\mathrm{el}}(V,T) + F^{\mathrm{mag}}(V,T) + F^{\mathrm{vib}}(V,T) + F^{\mathrm{ad.\ coup.}}(V,T). \tag{3.4}$$

If these DOFs are adiabatically decoupled in the system at hand, the different contributions can be calculated separately from different models and then put together. It is also possible to include an adiabatic coupling term ($F^{\mathrm{ad.\ coup.}}$), which can only be inferred from simulations that include all effects at the same time.

As earlier mentioned, here I focus on the canonical ensemble because it is the easiest to simulate. In an experiment, though, the volume is not a fixed quantity, rather the pressure p is fixed. Therefore, the thermodynamic quantity of relevance in experiments is the Gibbs free energy G:

$$G = E - TS + pV = H - TS = F + pV, \tag{3.5}$$

where $H = E + pV$ is the enthalpy. The equilibrium state of a system at a certain temperature and pressure is the one with minimum Gibbs free energy. To calculate the Gibbs free energy, one can perform calculations in the

NpT ensemble, for which barostats and thermostats have been developed. However, if the conditions that need to be simulated involve ambient pressure, which can be approximated to be zero, then the Gibbs and Helmholtz free energy coincide and one needs just to make sure that in the simulations the pressure is zero. A last method to calculate the the Gibbs free energy involves calculations in the canonical ensemble on a grid of volumes. If the Helmholtz free energy can be calculated, then the Gibbs free energy can be retrieved by inclusion of the pressure with the relation:

$$p = -\left(\frac{\partial F}{\partial V}\right)_{T,N}. \tag{3.6}$$

3.2 Sampling the phase space

Efficient exploration of the relevant configurations in the phase space of a system is fundamental in the calculation of free energies and phase stabilities. The computational methods employed in this work to sample the phase space are Monte Carlo (MC) and molecular dynamics (MD) simulations. Both techniques have their pros and cons: the former enables the sampling of the phase space efficiently, but is limited to the calculation of static properties; on the contrary, the latter can simulate also dynamics, however it is more difficult to sample energetically unfavourable configurations which are still relevant at the simulated temperature or relevant local minima hidden behind barriers.

An important detail to take into account in both techniques is how the energy of the system is calculated. For long simulations, a model interatomic potential for the system under investigation can be prepared and energies can be calculated from this. These potentials allow to perform simulations with a huge number of atoms, however they lack in accuracy and transferability. Another way is to calculate the energy (and forces in MD) with DFT, making the method *ab initio*. Recently, machine learning (ML) interatomic potentials have been developed to bridge this gap, since they are trained on *ab initio* calculations and they can retain their accuracy, at a cost comparable to model potentials. As always, choice of one or the other method is based on a balance between accuracy and cost, together with the complexity of the method itself: depending on the problem at hand, one method can be more suited than the other.

3.2.1 Ab initio molecular dynamics

Molecular dynamics is a technique that enables to sample phase space of a system by simulating the trajectory of its atoms. It can be in general performed in different ensembles (microcanonical, canonical, and constant-pressure), and potential energy and forces can be calculated either with model potentials (classical MD), or with DFT (*ab initio* MD, AIMD). In both cases, the nuclei are usually considered as classical particles, following Newton's equations of motion:

$$\mathbf{R}_I(t+\mathrm{d}t) = \mathbf{R}_I(t) + \mathbf{v}_I(t)\mathrm{d}t + \frac{\mathbf{f}_I(t)}{2M_I}\mathrm{d}t^2, \tag{3.7}$$

where $\mathbf{R}_I(t)$ and $\mathbf{v}_I(t)$ are the position and velocity of atom I with mass M_I, and $\mathbf{f}_I(t)$ is the force acting on it at time t. This equation is not actually used in MD simulations because it is not stable, so that other algorithms are employed (such as the Verlet or the velocity-Verlet algorithm, see e.g. [7] for a collection of methods). A central quantity in this equation is the timestep $\mathrm{d}t$, which has to be chosen carefully in order to obtain meaningful configurations, with a typical value of 1 fs employed in AIMD.

Forces in AIMD are calculated according to the Hellmann-Feynman theorem:

$$\mathbf{f}_I = -\left\langle \frac{\partial \hat{H}}{\partial \mathbf{R}_I} \right\rangle, \tag{3.8}$$

where $\hat{H}$ is the Hamiltonian of the system, and $\langle\ \rangle$ indicates the expectation value. AIMD gives a very accurate description of the dynamics of the system, however it is very computationally intensive so that only small systems can be simulated (commonly $\sim$ 100 – 200 atoms, at most $\sim$ 1000) and for short timescales ($\sim$ 1 ns). If larger sizes are needed, one can go to classical potentials that can be based on analytical models or fitted to *ab initio* results in order to perform larger scale simulations, or even ML potentials [37].

For calculations in the canonical ensemble, the system needs to be coupled with a thermostat which maintains the temperature of the system roughly constant (the amplitude of thermal fluctuations depend on the size of the system). Several types of thermostat are available, among which the simplest consists in a rescaling of the velocity of the atoms in order to meet the required temperature. Other methods consist in coupling the system with a thermostat that randomly pushes the atoms (Andersen and Langevin thermostats), resulting in a very good sampling of the phase space but with possible destruction of the system physical dynamics. The Nosé-Hoover thermostat, instead, introduces a fictitious system through an extended Lagrangian formulation which keeps the real system at the desired temperature; this is the preferred thermostat when dynamical properties are targeted. The Langevin thermostat was developed for dynamics simulations of liquids, but it has been then realized that it can be employed for simulations of solids. In this method, also known as Langevin dynamics, the equations of motions are modified such that:

$$\dot{\mathbf{p}}_I = \mathbf{f}_I - \gamma_I \mathbf{p}_I + \bar{\mathbf{f}}_I. \tag{3.9}$$

Here, $\mathbf{p}_I$ is the momentum of atom I, $\dot{\mathbf{p}}_I$ its time derivative, $\mathbf{f}_I$ is the interatomic force acting on atom I, γ_I is a friction coefficient (in units of inverse time), and $\bar{\mathbf{f}}_I$ is a random force related to γ_I. Sampling of the canonical ensemble with Langevin dynamics is ensured by the fluctuation-dissipation theorem. The parameter γ_I determines how often the system is "kicked" by the random force, so that for large values of this parameter one can employ large timesteps, obtaining a very good and fast sampling of the phase space, although at the expense of unrealistic dynamics. Nonetheless, it is still possible to recover the proper dynamics by decreasing the value of γ_I.

3.2.1.1 Nonequilibrium molecular dynamics - Color Diffusion algorithm

Direct MD simulations can be employed in the study of mass transport or other physical phenomena that involve dynamics to obtain rate and mechanism of the property under investigation; unfortunately, for rare events, MD might not give a good statistic of the process because of the long sampling times needed, especially in the case of AIMD. Many methods have been developed in the past years in order to overcome this obstacle[38], of which one example is the color diffusion (CD) algorithm [39]. The CD algorithm is part of the broader class of nonequilibrium MD (NEMD) methods, which in general consists in applying a force or perturbation on the system in order to accelerate the physical process of interest. In particular, a revisited version [40] of the original algorithm enables the simulation of vacancy-mediated diffusion with very large migration energies. The main difference between the original and the revisited versions is that in the former the force fields employed are small in order to remain in the linear regime, whereas in the latter an extension to higher force fields has been made.

The CD algorithm in the revisited version establishes a relation between the equilibrium jump rate $\Gamma_E(T)$ and the nonequilibrium jump rates $\Gamma(F,T)$ for different force field intensities F. It can be indeed shown that [40]:

$$\Gamma(F,T) = \Gamma_E(T) \exp\left[\frac{x_{TS0}(T)}{k_B T} F - \alpha(T) F^2\right], \tag{3.10}$$

where $x_{TS0}(T)$ is the distance of the position of the transition state from the equilibrium lattice position of the atom at temperature T and zero force field, α is a system-dependent parameter and k_B Boltzmann's constant.

The nonequilibrium jump rate $\Gamma(F,T)$ for a specific F and T is obtained fitting the vacancy jump times of a set of NEMD simulations at these conditions. In each single NEMD simulation, a force is applied on one of the vacancy's neighbors (the colored atom) so that it will jump faster than in equilibrium conditions (see Fig. 3.1a), and these jump times are fitted with an exponential or a Gamma distribution to obtain the rate (more details on the fitting procedure can be found in Paper I). Once the nonequilibrium rates are calculated for some force field intensities F, the equilibrium jump rate

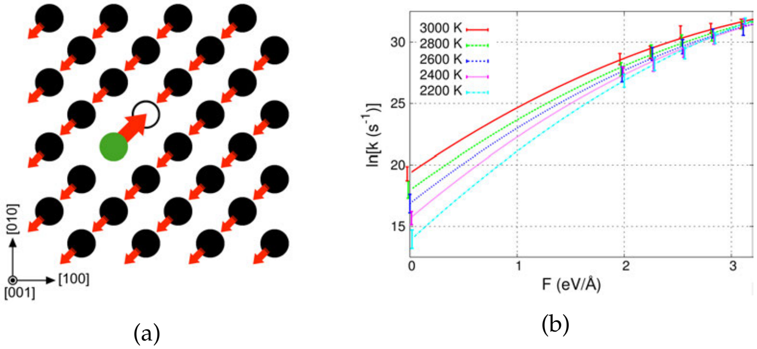

(a) (b)

Figure 3.1: a) Principle of the color diffusion algorithm: the colored atom (green) is pushed towards the vacancy (white) with a force F. An opposite force of intensity $F/(N-1)$, with $N-1$ the number of atoms in the simulation box without counting the colored atom, is applied to all the other atoms in order to maintain the system in mechanical equilibrium. Figure from Paper I. b) Logarithm of the nonequilibrium jump rate as a function of the force field intensity for Ti vacancy diffusion in TiN at different temperatures. The lines indicate the quadratic interpolation with the logarithm of Eq. 3.10. Figure from Paper I.

$\Gamma_E(T)$ at temperature T can be obtained by quadratic interpolation of the logarithm of the rates $\log \Gamma(F,T)$ as a function of force field intensity, where the quadratic behavior becomes obvious when taking the logarithm of Eq. 3.10, and which can be seen from Fig. 3.1b.

3.2.2 Monte Carlo simulations

Monte Carlo (MC) simulations are another method that allows to explore the phase space of a system at finite temperatures. This method relies on the fact that, in the canonical ensemble, we might not be able to calculate the full partition function of the system, however we can calculate the relative probability P of two states $\mathbf{x}_1$ and $\mathbf{x}_2$ knowing their energies E_1 and E_2, which is given by the ratio of the respective Boltzmann's factors:

$$\frac{P(\mathbf{x}_1)}{P(\mathbf{x}_2)} = \frac{\dfrac{\exp\left(-\frac{E_1}{k_B T}\right)}{Z}}{\dfrac{\exp\left(-\frac{E_2}{k_B T}\right)}{Z}} = \exp\left(-\frac{E_1 - E_2}{k_B T}\right). \tag{3.11}$$

In MC, one explores the phase space with random jumps from one state to another, commonly called MC moves, in order to reconstruct the probability distribution of these states thanks to Eq. 3.11.

The Metropolis algorithm, the most famous MC method, consists in performing sequential random jumps to a new state. Focusing on a jump from a configuration $\mathbf{x}_o$ with energy E_o to a new configuration $\mathbf{x}_n$ with energy E_n, then the jump is accepted if:

- $E_n - E_o \leqslant 0$;
- $E_n - E_o > 0$ and $\exp\left(-\frac{E_n - E_o}{k_B T}\right) \geqslant r$, with r being a random number taken in the interval [0,1].

In this way, the algorithm accepts always jumps that lead to lower energies, and it sometimes allows to explore states with higher energies; how often these states will be visited depends both on the energy difference and on the temperature of the system. Performing a large number of such steps, one can reconstruct the probability distribution of the system at temperature T and therefore calculate thermodynamic averages of static properties, since:

$$\langle A \rangle = \sum_i P(\mathbf{x}_i) A_i, \tag{3.12}$$

with A_i being the value of property A calculated on configuration $\mathbf{x}_i$. This also means that by calculating the arithmetic average of the A_i at each MC step, one readily obtains the thermodynamic average of the property A, since the configurations display already the correct distribution.

MC simulations are of course much more complicated than this, since different details concerning detailed balance, random number generation, and MC moves, to name a few, are important to ensure correct results. Nonetheless, it is quite straight-forward to write a code which performs the simple algorithm just described.

A common use of MC simulations is to determine transition temperatures from order to disorder for alloys or magnetic systems, where often one can use an Ising or a Heisenberg Hamiltonian to describe the energy of the system. The simplest way to determine the transition temperature consists in performing MC simulations for the system at different temperatures and calculate the specific heat capacity c_v as:

$$c_v = \frac{\langle E^2 - \langle E \rangle^2 \rangle}{k_B T^2}. \tag{3.13}$$

For these Hamiltonians, c_v will show a pronounced peak at the transition, which is readily seen from MC simulations. More sophisticated methods based on, e.g., the properties of the fourth-order cumulant[41] have been developed when accuracy is of primary importance, nonetheless the specific heat can already give a good estimate of the transition temperature.

3.3 Free energy calculation

Calculation of the free energy of a system is not a trivial task. This can be done analytically for simple models but, for more realistic systems, advanced techniques need to be employed. The free energy contributions that need to be calculated for a material are the vibrational and electronic contributions, together with the magnetic one if the system is magnetic. Electronic entropy can be readily included in *ab initio* simulations, therefore this term does not raise any problem. For what concerns the vibrational part, the phonon free energy is known analytically, which means that knowing the phonon dispersion relations of a system is enough to calculate the free energy. The analytical expression for the vibrational free energy does not include anharmonicity arising at high temperatures, therefore methods to include thermal expansion and intrinsic anharmonicity are needed, many having been developed in recent years to tackle these problems [42, 43]. However, if magnetism is present in the system, its contribution to the free energy is much more difficult to be included.

Methods to calculate the free energy that do not rely only on models and explicit analytical expressions for the entropic contributions are therefore needed. Fortunately, thermodynamic relations which relate derivatives of the free energy to ensemble averages of other quantities, which can be more easily calculated with the help of computer simulations, can be derived from statistical mechanics, enabling the direct calculation of free energies of realistic systems.

For the scope of this thesis, two types of such methods are of interest: thermodynamic integration (TI) and thermodynamic (or free energy) perturbation theory (TPT).

3.3.1 Thermodynamic integration (TI)

TI relies on the fact that some derivatives of the free energy are related to computationally-accessible ensemble averages of other properties. If we consider two systems characterized by the Hamiltonians H_0 and H_1, then one can define a parametric Hamiltonian as:

$$H(\lambda) = \lambda H_1 + (1 - \lambda) H_0, \tag{3.14}$$

so that, for $\lambda = 0$, we recover the Hamiltonian H_0 and, for $\lambda = 1$, the Hamiltonian H_1 is obtained. In this context, system is not necessarily meant as different material system, it can be also the same material but described with two different Hamiltonians. Eq. 3.14 is just the simplest coupling between the two Hamiltonians, but more sophisticated couplings can be useful for efficiency reasons. It can be shown that the free energy difference between system 1 and system 0, ΔF^{1-0}, is:

$$\Delta F^{1-0}(V,T) = \int_0^1 \left\langle \frac{\partial H(\lambda)}{\partial \lambda} \right\rangle_{V,T,\lambda} d\lambda = \int_0^1 \langle H_1 - H_0 \rangle_{V,T,\lambda}\, d\lambda, \tag{3.15}$$

where $\langle\rangle_{V,T,\lambda}$ indicates an ensemble average carried out with the Hamiltonian $H(\lambda)$ for the specific value of λ at temperature T and volume V, and for the last equality the parametric Hamiltonian of Eq. 3.14 has been assumed. The calculation of the free energy difference between the two systems therefore proceeds by performing simulations (MD or MC, depending on the systems under investigation) with different values of λ, and in each of these simulations one calculates the energy with the two Hamiltonians H_1 and H_0 on the atomic configurations generated with $H(\lambda)$. Integrating then this averages for λ going from 0 to 1 gives the free energy difference between the two Hamiltonians.

This procedure is very useful especially if the free energy of one of the two Hamiltonians can be calculated analytically [44–47]

As an example, one can take H_0 to be the Hamiltonian of an Einstein crystal, for which the free energy is known, and H_1 a more realistic Hamiltonian of a particular system, being this based on some interatomic potential or even a DFT Hamiltonian, obtaining therefore the free energy of the realistic system.

3.3.1.1 TI over temperature

If the free energy of a system is known at a certain temperature, one can then exploit the thermodynamic relation:

$$\frac{\partial(F(V,T)/k_BT)}{\partial(1/k_BT)} = \langle H \rangle, \tag{3.16}$$

with H being the Hamiltonian, which integrated leads to:

$$\frac{F(V,T_1)}{k_BT_1} - \frac{F(V,T_0)}{k_BT_0} = -\int_{T_0}^{T_1} \frac{\langle H \rangle_{V,T}}{k_BT^2}\, dT. \tag{3.17}$$

In this type of thermodynamic integration, one starts from a temperature T_0, for which the free energy $F(V,T_0)$ needs to be known, and then simulations at different temperatures are carried out, collecting average total energies; the free energy as a function of temperature (at constant volume) is then obtained by simple integration of this values with Eq. 3.17. If one is not interested in absolute free energies, but only free energy differences ΔF^{B-A} between two structures A and B of the same compound, then equation 3.17 becomes:

$$\Delta F^{B-A}(T_1) = \Delta F^{B-A}(T_0)\frac{T_1}{T_0} - T_1 \int_{T_0}^{T_1} \frac{\langle H_B \rangle_{V_B,T} - \langle H_A \rangle_{V_A,T}}{T^2}\, dT, \tag{3.18}$$

for which the free energy difference at a reference temperature T_0 is known by some other means.

3.3.1.2 Stress-strain TI

Eq. 3.6 relates pressure, volume, and free energy so that, if the dependence of pressure on volume is known, one can calculate the free energy difference at constant temperature. This relation can be generalized to anisotropic deformations of a rotationally-invariant crystal, i.e., which do not involve a simple volume expansion or contraction. This generalization allows to calculate the free energy difference between two structures by deforming one into the other through TI, called from now on stress-strain thermodynamic integration (SSTI) [48, 49].

The differential of the free energy for a rotationally invariant crystal at constant temperature can be written as:

$$dF(\mathbf{X}, \boldsymbol{\eta}) = V(\mathbf{X}) \boldsymbol{\tau} : d\boldsymbol{\eta}, \tag{3.19}$$

where $\mathbf{X}$ is a configuration of the crystal, $V(X)$ its volume, $\boldsymbol{\tau}$ is the second Piola-Kirchoff stress tensor, $\boldsymbol{\eta}$ the Lagrangian strain tensor, and : indicates a contraction over both indices ($\mathbf{A} : \mathbf{B} = \sum_{i,j} A_{ij} B_{ij}$) [48]. For configuration of the crystal here it is meant, e.g., a structure with a particular symmetry. If one wants to calculate the free energy difference between two structures, say structure 0 and structure 1, we start by defining any intermediate structure i with a matrix $\mathbf{h}^i$ made of its supercell lattice vectors $\mathbf{a}^i$, $\mathbf{b}^i$ and $\mathbf{c}^i$, arranged as:

$$\mathbf{h}^i = \begin{pmatrix} a^i_x & b^i_x & c^i_x \\ a^i_y & b^i_y & c^i_y \\ a^i_z & b^i_z & c^i_z \end{pmatrix}. \tag{3.20}$$

If the two structures can be transformed one into the other through an homogeneous transformation, say:

$$\mathbf{h}(\lambda) = \mathbf{h}^0 + \lambda(\mathbf{h}^1 - \mathbf{h}^0), \tag{3.21}$$

then it can be shown that the free energy difference between structures 1 and 0 is:

$$\Delta F^{1-0} = \int_0^1 V(\lambda) \left[\sigma(\lambda) \mathbf{h}^{-T}(\lambda) \right] : \frac{\partial \mathbf{h}(\lambda)}{\partial \lambda} d\lambda, \tag{3.22}$$

where $V(\lambda)$ is the volume of the intermediate configuration with matrix $\mathbf{h}(\lambda)$, $\sigma(\lambda)$ is the stress tensor for the same configuration, and $^{-T}$ indicates the inverse and transposed matrix. These last two tensors are multiplied by each other before performing the contraction. For an $\mathbf{h}(\lambda)$ linear in lambda as in Eq. 3.21, the derivative inside the integral becomes simply $\mathbf{h}^1 - \mathbf{h}^0$.

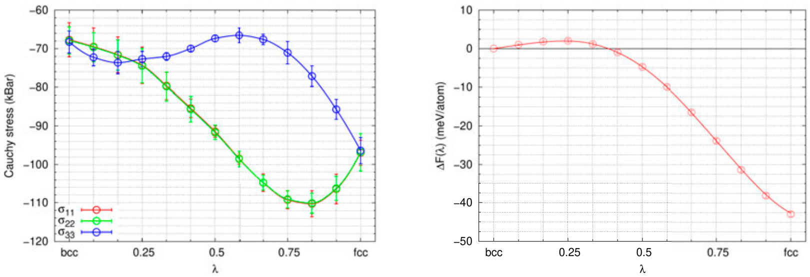

(a) (b)

Figure 3.2: a) Isotropic stresses along the deformation path from bcc to fcc Fe at T=0 K with equilibrium volume at 1000 K calculated from ASD-AIMD. The interpolation of stresses is done with a piece-wise cubic Hermite interpolating polynomial. Error bars indicate two standard deviations of the stresses. b) Resulting (free) energy difference as a function of λ from SSTI with Eq. 3.22. The energy difference from SSTI is -42.9 meV/atom, the same as obtained from direct difference of the fcc and bcc energies.

Simpler expressions for the integrand can be derived depending on the symmetries of the crystal and on the explicit form of the $\mathbf{h}(\lambda)$ tensor.

Details regarding the number of intermediate structures along the deformation path employed, the method of interpolation of the stresses, as well as the numerical integration method can affect the accuracy of the resulting free energy difference.

A quick benchmark of the accuracy of this method can be performed at T=0 K, for which the free energy difference between the initial and the final configuration is just the energy difference between them, and therefore the result of SSTI can be directly compared to the explicit energy difference. To show this correspondence, I calculate the energy difference between fcc and bcc Fe in the paramagnetic state modeled with the magnetic sampling method (MSM, see Sec. 4.4), both with SSTI and direct energy difference. The bcc and fcc structures can be transformed one into the other if one takes tetragonal unit cells, which are:

$$\mathbf{h}^{\mathrm{bcc}} = \begin{pmatrix} a^{\mathrm{bcc}} & 0 & a^{\mathrm{bcc}}/2 \\ 0 & a^{\mathrm{bcc}} & a^{\mathrm{bcc}}/2 \\ 0 & 0 & a^{\mathrm{bcc}}/2 \end{pmatrix}; \mathbf{h}^{\mathrm{fcc}} = \begin{pmatrix} a^{\mathrm{fcc}} & 0 & a^{\mathrm{fcc}}/2 \\ 0 & a^{\mathrm{fcc}} & a^{\mathrm{fcc}}/2 \\ 0 & 0 & a^{\mathrm{fcc}}/\sqrt{2} \end{pmatrix}, \tag{3.23}$$

and using the coupling matrix of Eq. 3.21 with bcc= structure 0 and fcc= structure 1. With such a deformation path, the resulting diagonal components of the stress tensor and integrated $\Delta F^{\text{fcc-bcc}}$ as a function of λ are shown in Fig. 3.2. The total energy difference calculated directly and calculated with SSTI agree to the sub-meV/atom level ($\Delta F^{\text{fcc-bcc}}$=-42.9 meV/atom). In

Fig. 3.2a, one can notice that the initial and final stresses are not zero; this is because calculations are performed with the equilibrium volume at T=1000 K calculated with ASD-AIMD. More details can be found in Sec. 6.2.2 and in Paper XI.

3.3.2 Thermodynamic perturbation theory (TPT)

TPT is a very powerful tool that is based on the same assumptions of TI, but enables calculation of free energy differences between two different model Hamiltonians without incurring in problems with integration error. Starting with a coupled Hamiltonian as in Eq. 3.14, one can show that the free energy difference between models H_0 and H_1 at temperature T and volume V can be calculated as:

$$\Delta F^{1-0}(V,T) = -k_B T \left\langle \exp\left(-\frac{H_1 - H_0}{k_B T}\right)\right\rangle_{V,T,\lambda=0}, \tag{3.24}$$

where $\langle\,\rangle_{V,T,\lambda=0}$ indicates a thermodynamic average at volume V, temperature T, and on the phase-space of Hamiltonian H_0 (equivalent to $\lambda = 0$. This method therefore needs only to perform a simulation (MC or MD) with Hamiltonian H_0, and then calculate the energy on several snapshots of the simulation with both Hamiltonians H_1 and H_0. To be accurate and efficient, the method requires that the phase-spaces spanned by H_1 and H_0 are similar enough, which can be estimated from the magnitude of the standard deviation of $E_1 - E_0$.

4 Microscopic description of magnetism

Magnetism in solids is a collective electronic phenomenon. The exact way to describe this effect would be to take into account the many-body wavefunction of the electrons; this is of course highly unpractical, therefore methods to solve this problem in an easier way have been devised. As mentioned in Chapter 2, DFT enables (sometimes) the calculation of the ground state of magnetic materials, but in general it has to be complemented with other models to describe finite-temperature excitations.

A method that has the theoretical framework to describe appropriately correlation effects and electronic excitations in magnetic materials is dynamical mean field theory (DMFT) [50, 51]. This theory is based on the Hubbard model, where the lattice problem is mapped onto an impurity model of an atom embedded in an electron bath. Even though very successful in the description of strongly correlated systems and excitation spectra, it still is a mean-field theory, therefore inheriting all the common problems of this type of theories; together with this, it is often used in a single site fashion, although there are examples of DMFT studies involving clusters of sites [52]. In addition, being based on a model Hamiltonian, its parameters have to be derived, incurring at times in a loss of *ab initio* character [53]. Moreover, the computational cost of this method, based on a Quantum Monte Carlo solver, is often extremely high, enforces the accurate modeling of only d and f electrons, neglecting possible interatomic interactions with p electrons[54]. Recently, examples of calculation of forces in DMFT have come out [55–58], showing the feasibility of calculation on phonon dispersion relations with this method, although these are still rare and very expensive. To summarize, the extreme computational cost of DMFT simulations underlines the need of developing DFT-based methods that enable an approximate description of all the degrees of freedom of the system (structural, magnetic, vibrational), allowing also to describe critical regions, which can then, if needed, be used as a basis for more sophisticated DFT+DMFT calculations. An example of such a DFT+DMFT investigation will be described in Chapter 6 and can be found in Paper IX.

The aim of this chapter is to introduce the semiclassical theory of spin fluctuations, focusing in particular on the Heisenberg Hamiltonian and its extensions, and describing methods to simulate the high temperature paramagnetic state of a magnetic material with DFT. At last, the approach used in my work to combine vibrations and spin dynamics is reviewed.

4.1 Magnetism in the ground state

The ground state of a magnetic material depends on the details of its electronic structure, which defines what is the mechanism with which the moments on different sites interact with each other. In Sec. 1.2, some examples of magnetic order have been introduced.

The simplest ordering possible is the ferromagnetic order, which means that at 0 K the moments on the magnetic atoms are directed in the same direction, parallel to each other. An example of such ordering are the elemental band ferromagnets Fe, Co and Ni, which are all metals, where the interaction between magnetic moments is mediated by the electron sea that keeps together these materials. The presence of moments is made possible by the partial localization of the *d*-electrons, which means that they are not completely free to go from one atom to the other as the *s*- and *p*-electrons, although they are still involved in conduction. Another way to see to this mechanism involves consideration of the Hamiltonian for a system of nuclei and electrons, Eq. 2.2, that enters the time-independent Schrödinger equation, Eq. 2.3. Because of the Pauli exclusion principle, electrons with the same direction of the spin tend to stay further apart as compared to electrons with the opposite direction of the spin: in other words, electrons with parallel spins have a lower repulsion energy than electrons with antiparallel spins. This effect is counterbalanced by an increased kinetic energy for electrons further apart, and the presence or the absence of magnetic moments in a particular system finally comes from the net balance of these two energy terms. The formation of a magnetic moment on an atom polarizes the electron density on neighboring atoms and results in a splitting of the electronic bands, which leads to a reduction of the energy of the system. A simplified DOS of a band ferromagnet is shown in Fig. 4.1.

On the opposite, an ordering that is more common in insulators and semiconductors is the antiferromagnetic ordering, examples of which are the transition metal oxides like NiO and CrN, to name two examples related to this thesis. In these systems, the localized moments on the transition metals do not interact with each other directly, but through the nonmetallic element in question. The textbook explanation of magnetism in NiO is based on the concept of superexchange, which involves the occupation of the orbitals of

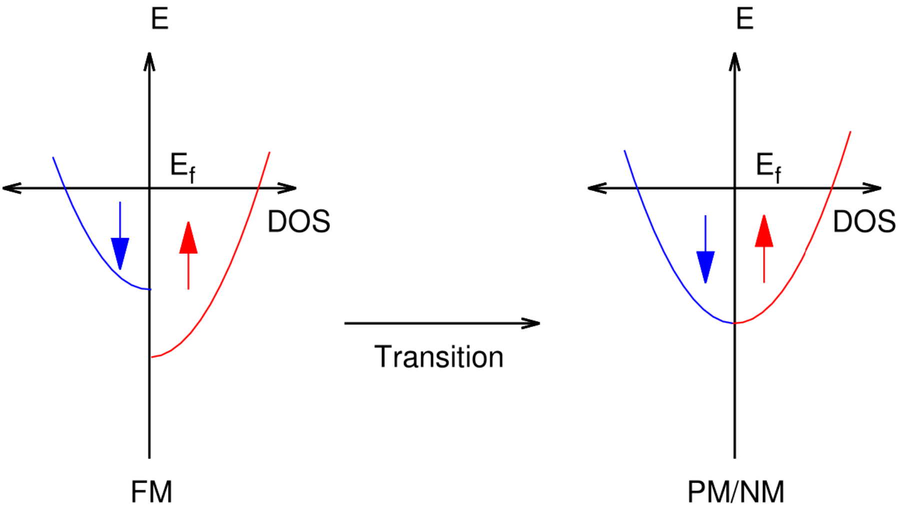

Figure 4.1: Schematic electronic DOS of a ferromagnetic (FM) material displaying band ferromagnetism. Red and blue lines indicate spin-up and spin-down channels, respectively. The left figure shows a schematic DOS in the FM state, with more electrons in the spin-up state than in spin-down. The right figure indicates the DOS of a nonmagnetic (NM) material, which is equivalent to the paramagnetic (PM) state in the Stoner picture.

the metallic element and how the orbitals of the nonmagnetic element are directed. In NiO the orbitals involved in the binding are the $2p$-orbitals of O atoms and the $3d$-orbitals of Ni atoms. Due to the highly directional character of these orbitals and the way they hybridize, an antiparallel ordering of the Ni moments occurs. More complicated arrangements can be present in systems where, as an example, there are competing exchange interactions or just due to geometrical frustration, with the extreme example of spin-glasses where the direction of the moments on different sites in the ground state is random.

4.2 Magnetism at finite temperature

All the ground state arrangements mentioned in the previous section have something in common: the perfect, static arrangement is lost when temperature is increased, and models to simulate and predict the behavior at finite temperatures is crucial for proper modeling. Historically, two models have been employed to describe magnetism at finite temperatures: the Stoner and the Heisenberg model. In the Stoner model, the effect of temperature is simply to redistribute the electrons from the spin-up channel to the spin-down channel (see Fig. 4.1) and, at the transition temperature, the number of spin-up and spin-down electrons is equal in the system, leading to a nonmagnetic (NM) system. This model explains the existence of metallic/itinerant magnetic materials, and it is very good to predict which elements are magnetic in their solid form; however, it completely fails in the prediction of the behavior at finite temperatures. On the contrary, the Heisenberg model predicts the existence of spin waves and it can be used to predict the Curie temperature, often with a good accuracy, but it fails to explain the change of the size of magnetic moments with temperature, for example. These models also reflect the nature of different magnetic materials: Stoner theory can be used only for metallic systems, since the magnetism in this model arises from a disequilibrium between spin-up and spin-down electrons at the Fermi level; Heisenberg theory can in principle be used only on systems with very well localized moments. A spin fluctuation theory (SFT) that interpolates between the two limits was developed by Moriya, being the basis of many new theories developed in the years that try to model the behavior of realistic magnetic systems with temperature. As exemplified in Fig. 4.2, SFT models both the transverse spin fluctuations (TSF) inherent of the Heisenberg model, as well as the longitudinal spin fluctuations (LSF) that are at the base of the Stoner model. The ideas of SFT can be implemented in an extended framework of Heisenberg theory to try to model the intermediate magnetic behavior typical of real magnets.

4.3 The generalized Heisenberg Hamiltonian

.

The semiclassical Heisenberg Hamiltonian describes a static lattice of spins or magnetic moments with a constant magnitude and well defined constant interaction J_{ij}, expressed as:

$$H = -\sum_{i \neq j} J_{ij} \mathbf{e}_i \cdot \mathbf{e}_j. \tag{4.1}$$

In this equation, the sum is over every pair of moments i, j, and $\mathbf{e}_i$ indicates the direction of moment i, $\mathbf{e}_i = \mathbf{m}_i / m_i$. Usually, one defines exchange interactions up to a given coordination shell and sets the other ones to zero. It can be shown that the classical Hamiltonian can be derived from its quantum version (with the moments replaced by the spin operators $\hat{S}$) in the limit of $\hbar \to 0$, $s \to \infty$, where s is the spin quantum number, $\hat{S}^2 |s\rangle = \hbar^2 s(s+1)|s\rangle$. Requiring that $s \to \infty$ corresponds to requiring that the spin can point in any direction in space, going therefore from quantized to continuum regime. An error introduced by neglecting the quantum nature of the spins is that the size of the spins in the semiclassical case is s, whereas in the quantum case is $\sqrt{s(s+1)}$. The other error introduced by neglecting the quantum nature of the spins is related to the occupation of states at finite temperature: spin

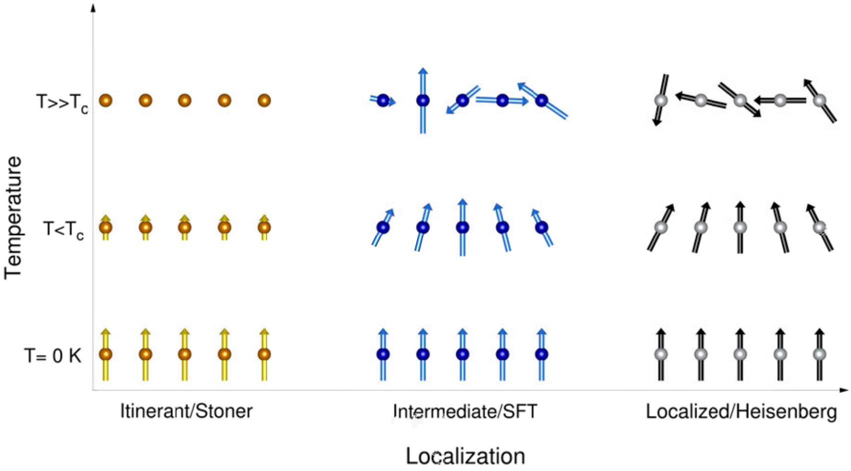

Figure 4.2: Schematic representation of the behavior with temperature of the different types of magnetic system/models of magnetism. At 0 K, all models of a simple ferromagnet provide the same picture. As temperature increases, the Stoner model, which describes a fully itinerant system, predicts that the order of the moments remains the same, while the size decreases, up to the transition temperature where the moments become zero and the system is nonmagnetic. On the opposite side, the Heisenberg model describes fully localized moments which start fluctuating in direction with temperature but keeping the size constant, and above the critical temperature they are completely disordered with respect to each other. The spin fluctuation theory (SFT) describes more realistic systems which are in between the two limits and tries to model fluctuations both in size and in direction with increasing temperature.

excitations are bosonic in nature, therefore the proper statistics to employ is the Bose-Einstein statistics rather than the Boltzmann statistics. Employment of the classical statistics is apparent in the specific heat at low temperatures, as will be shown in Sec. 4.3.1; examples of implementation of the quantum statistics in MC simulations are available in the literature [59].

The exchange interactions J_{ij} define the type of magnetic order of the system: if $J_{ij} > 0$, parallel spins lower the energy of the system and are therefore favored, whereas if $J_{ij} < 0$ antiparallel spins are favored. The exchange interactions are related to the exchange integral that appears in the Schrödinger equation, and in a 2-electrons model they are given by the energy difference between the triplet and the singlet states (where exchange interaction and exchange integral coincide). For solids, the relation is more complex, but several methods for the calculation of these quantities within DFT have been developed in the years [60–62].

Although the basic Heisenberg Hamiltonian of Eq. 4.1 has been proven successful for the prediction of T_C in many metallic systems, one needs to remember that examples of fully localized systems are quite rare, and often the Hamiltonian has to be made more flexible to be able to model accurately a real material. A first example of an approximation that can be lifted in the basic Heisenberg model is related to the magnitude of the moments, which are considered fixed and constant over the whole lattice in the original formulation. However, this might not hold for a realistic system, since the size of the moments depends on the underlying electronic structure and therefore is sensitive to the local environment; one way to improve Eq. 4.1 is then to make the exchange interactions J_{ij} independent of the magnetic moments size:

$$H = -\sum_{i \neq j} \tilde{J}_{ij} \mathbf{m}_i \cdot \mathbf{m}_j, \tag{4.2}$$

with $J_{ij} = |\mathbf{m}_i||\mathbf{m}_j|\tilde{J}_{ij}$. It is important to notice here that $\tilde{J}_{ij}$ does not depend on the size of the moments i and j, whereas J_{ij} does.

Another assumption of the Heisenberg model is that the exchange interaction between two moments does not depend on the environment, so that independently if the system is in, e.g., a ferromagnetic or paramagnetic state, the exchange interaction between atom i and j is always the same. However, this is typically not true, especially if one tries to study ferromagnetic metals with this model. As an example, it has been shown in Ref. [61] that for bcc Fe (which is often considered a Heisenberg system) the exchange interactions considerably change if calculated with a FM or a PM background, with T_c calculated with the FM exchange interactions being 740 K, as compared to 1090 K calculated with the latter Js ($T_c^{\exp} = 1043K$). The success of the PM Js is due to the fact that, near T_C, the magnetic system resembles more a PM phase rather than a FM one, therefore the relevant exchange interactions are the ones calculated with a PM background. For magnetic thermal excitations at low temperatures, instead, the relevant J_{ij}s are the ones calculated with FM background since the system is in this state. One can then imagine that the effect of the environment is even more pronounced when one tries to apply the Heisenberg model to more itinerant systems.

An additional important detail is that the Heisenberg model is based on a static lattice. In reality, of course, atoms vibrate, therefore the J_{ij}s are going to depend on the details of the atomic positions in the local environment. One simple way to include this effect is to parametrize the exchange interactions as a function of the distance between pairs of moments. This parametrization can be a smooth function as observed in CrN [62], but it can also be very complicated, as seen in bcc Fe [63, 64], for which taking into account only the distance between the pair might not be enough.

Further extensions of the Heisenberg Hamiltonian can be applied in order to include anisotropy or spin-orbit effects [65], as well as higher-order interactions between two moments or even clusters of moments. These terms are not employed in the thesis, therefore they will not be discussed.

As a final remark, I would like to stress that the Heisenberg Hamiltonian deals only with the transversal magnetic degrees of freedom (DOFs). However, in systems with a certain degree of itineracy, one needs to find a way to include fluctuations of the longitudinal DOF as well.

4.3.1 Calculation of transition temperature with the Heisenberg model

The framework of statistical mechanics presented in Chapter 3 can be employed with the Heisenberg Hamiltonian to calculate the transition temperature of a magnetic material from ordered to disordered state. It is common to employ MC simulations to calculate these quantities since evaluation of the energy with Eq. 4.1 is computationally cheap, once the exchange interactions have been evaluated using a DFT-based method. The transition temperature T_c can be evaluated tracking the specific heat c_v as a function of temperature which shows a peak at the T_c, as briefly mentioned in Sec. 3.2.2.

It is interesting to see how transition temperatures are affected by the strength of the exchange interactions, as well as the model employed. As an example of this latter case, one can compare the results from the Heisenberg and the Ising models, where the only difference between the two is that in the Heisenberg model the moments/spins are three-dimensional vectors, whereas in the Ising model they are one-dimensional, i.e., they can only point up or down. The specific heat for an fcc lattice with interactions up to second nearest neighbors, with $|J_1| << |J_2|$ and $J_2 < 0$, is shown for both models in Fig. 4.3 as a function of rescaled temperature $T/|J_2|$, together with the short range order parameter (SRO) for second nearest neighbors, generally defined as:

$$\mathrm{SRO}_{\mathrm{NN}S} = \langle\langle \mathbf{e}_i(t) \cdot \mathbf{e}_j(t) \rangle_{\{i,j\}\in S} \rangle_t, \tag{4.3}$$

where the scalar product between the unit vectors $\mathbf{e}_i$, $\mathbf{e}_j$ is averaged over all the pairs i, j in the coordination shell S, and over all configurations t in the simulation. The first thing to notice is the discrepancy in position of the maximum of the c_v, with the Ising T_c being approximately three times larger than the Heisenberg T_c. This plot also shows the previously mentioned shortcoming of the classical Heisenberg Hamiltonian: the specific heat does not go to zero at 0 K, but it converges to a constant value of approximately k_B. This is a well known problem of the classical Heisenberg Hamiltonian, since at low temperatures the appropriate quantum occupation is needed to ensure the correct limit of $c_v \rightarrow 0$ for $T \rightarrow 0$ K. This problem is not seen in the Ising system, since the only states available are just with up and down spins, and the flipping of one single spin at low temperatures is a very unlikely move because of the energy required for this process. From this point of view, the Ising system is "quantized". The absence of spin flips in the Ising system can be clearly seen from the SRO for second nearest neighbors at low temperatures in the plot on the right. Finally, it is interesting to notice that at high temperatures, approximately twice as large as the Ising transition temperature, the specific heat of the two models is very similar, indicating that here the disorder is so much that the dimensionality of the moments does not matter anymore for this quantity. However, a small difference persists even to higher temperatures in the SRO parameter (note the different scale in the x-axis in the two plots).

A final remark concerns the dependence of the transition temperature on the absolute value of the exchange interactions, which also raises an issue in comparing the results of MC simulations with the literature. In Fig. 4.4, the Néel temperature of NiO from MC simulations is plotted against the value of J_2, which is the strongest exchange interaction in this system. In the left plot, the transition temperature from my own simulations (blue diamond) is compared with the transition temperatures from the literature [66–68] as published. One can see immediately that the results from Archer *et al.* and from Gopal *et al.* follow a clear trend, except for two points in the top-left part of the plot which were derived with a much larger value of J_1 compared to all other points; the results from my own calculations and from Fischer *et al.*, instead, are not following the trend. However, from a closer inspection of the articles, one realizes that in the former two articles, the Heisenberg Hamiltonian is defined as:

$$H = -\frac{1}{2}\sum_{i \neq j} \bar{J}_{ij} \mathbf{e}_i \cdot \mathbf{e}_j, \tag{4.4}$$

where, compared to Eq. 4.1, $\bar{J}_{ij} = 2J_{ij}$. Fischer *et al.*, instead, used the same definition of Heisenberg Hamiltonian and exchange interactions as in Eq. 4.1, but they apply a correction term of two to the transition temperature to take into account the quantum nature of the spins, as mentioned previously (the spin quantum number in NiO is $s = 1$). Rescaling exchange interactions and transition temperatures accordingly, the resulting plot is shown on the right of Fig. 4.4, with all the values following the same trend.

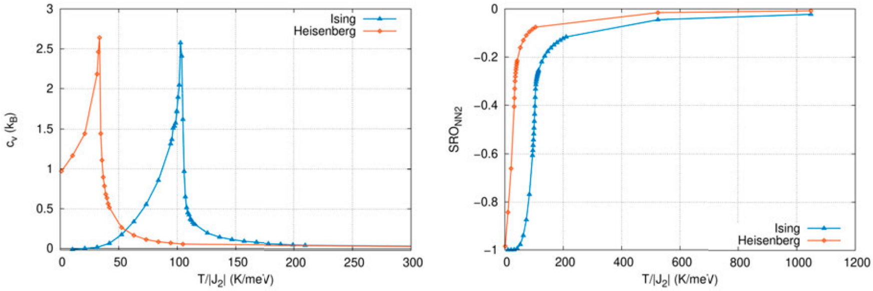

Figure 4.3: Comparison of the specific heat c_v (left) and the SRO for second nearest neighbors SRO_{NN2} (right) as a function of rescaled temperature $T/|J_2|$ from simulations with the Ising (blue triangles) and Heisenberg (red diamonds) Hamiltonians. Notice the different scale of the x-axis in the two plots.

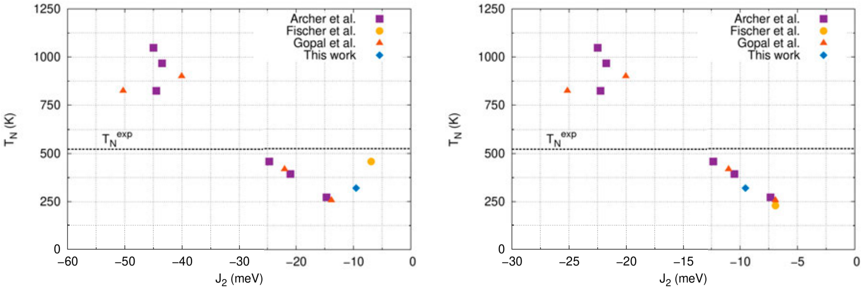

Figure 4.4: Néel temperature T_N of NiO as a function of the exchange interactions between second nearest neighbors J_2 from MC calculations from the my own calculations and from literature. In the left figure, the values of T_N and J_2 are plotted as published. On the right, the values are rescaled according to Eq. 4.1 and removing quantum corrections of the size of the spins.

4.3.2 Longitudinal spin fluctuations

LSF are related to electronic excitations in a more intimate way than magnetic transverse DOFs, and they are typically faster than these last ones; nonetheless, semi-classical models that allow for the approximate inclusion of this effect in the framework of the Heisenberg Hamiltonian have been developed [69, 70]. A common way [70–74] to include this effect in the framework of the generalized Heisenberg Hamiltonian is to add an on-site term which depends on the surrounding only in a mean-field manner:

$$H_{\mathrm{LSF}} = -\sum_{i \neq j} \tilde{J}_{ij} \mathbf{m}_i \cdot \mathbf{m}_j + \sum_i E(m_i). \tag{4.5}$$

The term $E(m_i)$ in the Hamiltonian describes the dependence of the energy of moment i on its own magnitude m_i, which in general depends on the environment; from Landau theory, this term can be expanded in even powers of the moment size:

$$E(m_i) = \sum_{n=0}^{\infty} a_{2n} m_i^{2n}. \tag{4.6}$$

The expansion truncated to 4th order already describes, at least qualitatively, the dependence of the on-site energy on the moment size. The Heisenberg-Landau Hamiltonian of Eq. 4.5 has been used in the past to explain properties of the ferromagnetic elemental solids (bcc Fe, Ni and Co)[70, 72–74] and Heusler alloys [71], to name a few.

Due to the semiclassical nature of this model, the Landau term can be applied in principles only at high temperatures, where electronic spin-flips occur often and they can affect the size of the moments. In the quantum regime, these spin flips need to follow the appropriate quantum statistics, and Eq. 4.5 does not describe well this process. This method has therefore been employed mainly in the PM state, where the spin-spin correlation functions (which are the same as the SRO previously defined) are approximately zero.

How the LSF energy affects the behavior of the system as a function of temperature depends strongly on the nature of the system: in fact, itinerant and localized moments systems in a PM environment show a very different functional dependence of $E(m_i)$, as shown in Fig. 4.5. In the PM regime, itinerant systems (blue dotted line in Fig. 4.5) show a minimum energy for null moment, whereas localized moment systems (red solid line) has minimum energy at some finite value. This means that, at high temperatures, the moments of an itinerant system can be non-zero only because of an entropic advantage of having magnetic moments in the system.

To understand why at high temperatures an itinerant system maintains magnetic moments, we need to employ Eq. 4.5 in the framework of statis-

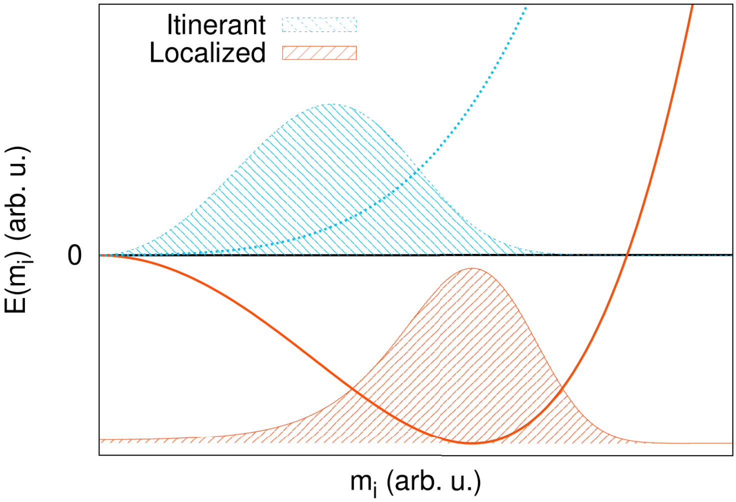

Figure 4.5: Typical on-site LSF energy as a function of the moment size for an itinerant (blue dotted line) and a localized moment (red solid line) systems in a paramagnetic background. The itinerant system has minimum energy for $m = 0$, whereas the localized moment system has it for $m > 0$. Distributions of moments at finite temperature calculated with numerical integration of the partition function from Eq. 4.8 for the itinerant case, and the partition function from Eq. 4.9 for the localized case are also shown, to exemplify the effect of temperature in the two cases. The zero of these distributions is set at the minimum of the corresponding landscape.

tical mechanics. If we consider the system to be in an ideal PM state, for which all spin-spin correlation functions are identically equal to zero, then the Hamiltonian is composed only of the onsite terms $E(m_i)$, Eq. 4.6. Since the Hamiltonian does not depend on terms involving the product of two spins, we can decouple the partition function in the product of the partition functions for each single moment, namely:

$$Z_i = \int \mathrm{d}\mathbf{m}_i \exp\left(-\frac{E(m_i)}{k_B T}\right), \tag{4.7}$$

where the integral is extended to all possible directions and sizes of the moment $\mathbf{m}_i$. Expressing now $\mathbf{m}_i$ in spherical coordinates and integrating out the angular variables, one obtains the expression:

$$Z_i = 4\pi \int \mathrm{d}m_i\, m_i^2 \exp\left(-\frac{E(m_i)}{k_B T}\right). \tag{4.8}$$

The m_i^2 term deriving from the spherical coordinates is called phase space measure (PSM) and contributes in the integral to give more weight to moments with large sizes. Within this model, therefore, moments with larger sizes are more favoured, inducing moments even in an itinerant system. This explanation is based on the assumption of dealing with an itinerant system. In this case, the quasi-parabolic landscape in Fig. 4.5 suggests that moments can appear and disappear in any direction if the temperature is high enough, sampling the phase space very quickly. In the case of a localized moment system, instead, the moments cannot change direction as in the itinerant system, but they involve a rigid rotation of the moment. The problem of LSF can be therefore thought as a one-dimensional problem in this case, where the size of the moments fluctuates in the one-dimensional landscape defined by $E(m_i)$ at each angle, resulting in a decoupling between TSF and LSF and leading to a partition function of the type:

$$Z_i = 4\pi \int \mathrm{d}m_i \, \exp\left(-\frac{E(m_i)}{k_B T}\right), \tag{4.9}$$

where the 4π factor deriving from angular integration is still there, but no m_i^2 is present. In this case, therefore, PSM=1, removing the entropic advantage to large moments. Unfortunately, as mentioned before, realistic systems are never completely itinerant or completely localized: it follows that it is not trivial to choose which PSM to use [75, 76], and also intermediate PSMs have been proposed [74].

A key quantity to calculate in this context is the magnetic entropy. An expression often used is a mean field approximation derived from basic quantum mechanical considerations and translated to the classical moments by taking the proper limits $\hbar \to 0$, $s \to \infty$. In the quantum system, the entropy can be derived counting all the possible states that the spin can assume in the PM state; taking the limits, the entropy becomes [10, 74]:

$$S^{\mathrm{mag}} = k_B \log(m+1). \tag{4.10}$$

Another form of the entropy can be analytically derived assuming an Hamiltonian as in Eq. 4.5 with a quadratic on-site term, which is consistent with an itinerant ferromagnet. In this approximation, and employing PSM=m^2 the entropy reads [72]:

$$S^{\mathrm{mag}} = 3k_B \log m, \tag{4.11}$$

and employing PSM=1 the entropy becomes:

$$S^{\mathrm{mag}} = k_B \log m. \tag{4.12}$$

The second expression can be, in principle, employed for a more localized ferromagnet as bcc Fe if the minimum of the energy landscape is deep and can be approximated with a parabolic term, in a harmonic-approximation fashion. In general, the size of the moment m at a certain temperature T can then be calculated minimizing the free energy including either of these entropic terms, with the underlying assumption that LSFs are adiabatically fast compared to TSFs and vibrations. This entropic contribution can be applied directly within DFT to the single-particles wavefunctions, for which the free energy to minimize includes, together with the Mermin functional for the electronic entropy, the magnetic entropy [72].

4.4 Disordered local moment approach

The semi-classical models described so far rely on model Hamiltonians, for which one needs to calculate the parameters. With the help of constraints (see Sec. 2.3.1), one can employ the magnetic configurations derived with these models within DFT, but this is very computationally intensive. In the past, a computationally cheaper method to model the PM phase in DFT calculations was developed: the disordered local moment (DLM) approach.

The DLM approach is a semi-classical model based on the work of Hubbard and Hasegawa [77–81] and firstly implemented in the coherent potential approximation (CPA) framework by Gyorffy *et al.* [82]; later on, it has been developed also in supercell approaches [83]. Its applicability is motivated by the fact that, most often, the magnetization density can be viewed in the localized moment picture previously described.

In this approach, the PM phase is modeled by distributing up and down magnetic moments on the atoms. In the CPA framework, which was devised to model random alloys, a system in the PM state is thought as a random $A_{0.5}B_{0.5}$ alloy, with A being up and B down moments. In the supercell approach, two methods have been developed: the first one is based on a magnetic special quasirandom structure (SQS), in analogy with the alloy, where up and down moments are distributed in a single supercell in order to mimic a completely disordered magnetic system, with spin-spin correlations approximately zero; the second one, known as magnetic sampling method (MSM), is based on the use of different configurations in which the moments are randomly distributed, and physical properties are then obtained as averages over all the configurations. In this latter case, the SRO for the relevant shells might not be zero for a single configuration, however, if enough of these random configurations are employed, on average the correlation is zero. It has been shown [83] that in the MSM method correlation functions and self-averaging properties converge to SQS and CPA results. The MSM method was used in my work also with noncollinear configurations of the magnetic moments, in order to have a better representation of the magnetic disorder. This method inherits all the advantages of supercell methods related to, e.g., lattice relaxations, at the cost of a higher computational effort.

In general, the DLM approach models an ideal PM phase, which is formally true only at temperatures $T \to \infty$, or at least $J/T \to 0$, with J being the strongest exchange interaction. It is however possible to introduce different degrees of magnetic short range order in this approach, especially in the MSM implementation. The DLM method in its different implementations has been able to reproduce many interesting features due to the change in magnetic properties at high temperature [83–86], without the need to resort to expensive higher-level theories.

It has also been implemented together with MD simulations [87–90] (DLM-MD), where the configuration of the moments is changed every few timesteps. However, in this method, the magnetic and vibrational DOFs are not fully coupled, since the magnetic state is changed randomly, and therefore there is an effect of infinite-temperature magnetism on vibrations. The main assumption of DLM-MD is that the magnetic DOFs are adiabatically fast as compared to vibrational DOFs, which could be a good approximation at very high temperatures, but is definitely not true at temperatures close to the magnetic transition. In order to include the interplay between lattice vibrations and magnetism, one needs to go beyond the decoupling of magnetic and vibrational degrees of freedom.

4.5 Spin dynamics and coupling with lattice vibrations

It is clear from the previous section that the modeling of finite-temperature magnetism with DFT is not easy. The DLM method allows to model an ideal PM state, corresponding to infinite magnetic temperature, whereas in experiments this is never the case. The MC method described in Sec. 3.2.2 and 4.3.1 allows to access finite-temperature properties, although dynamic properties are not available from this method, and often relies on model Hamiltonians with parameters from 0 K DFT calculations. Simulations of the dynamics of the magnetic DOFs is possible, similarly to MD (Sec. 3.2.1), with atomistic spin dynamics (ASD) simulations. The dynamics of magnetic moments at the semi-classical level is based on the Landau-Lifshitz-Gilbert (LLG) equations, a set of equations modeling the precession of magnetic moments under the effect of an effective field $\mathbf{H}_{\text{eff}}$:

$$\frac{\partial \mathbf{e}_i}{\partial t} = -\frac{\gamma}{1+\alpha^2}\mathbf{e}_i \times [\mathbf{H}_{\text{eff}} + \mathbf{f}_i] - \gamma\frac{\alpha}{1+\alpha^2}\mathbf{e}_i \times \{\mathbf{e}_i \times [\mathbf{H}_{\text{eff}} + \mathbf{f}_i]\}, \tag{4.13}$$

where $\mathbf{e}_i$ is the unit vector along the direction of moment $\mathbf{m}_i$, γ and α are the electron gyromagnetic ratio and the phenomenological damping factor, respectively, whereas $\mathbf{f}_i$ is the random force employed in Langevin dynamics (see Sec. 3.2.1). $\mathbf{H}_{\text{eff}}$ is the effective magnetic field experienced by moment $\mathbf{m}_i$, due to all the other moments in the solid, and it is expressed as:

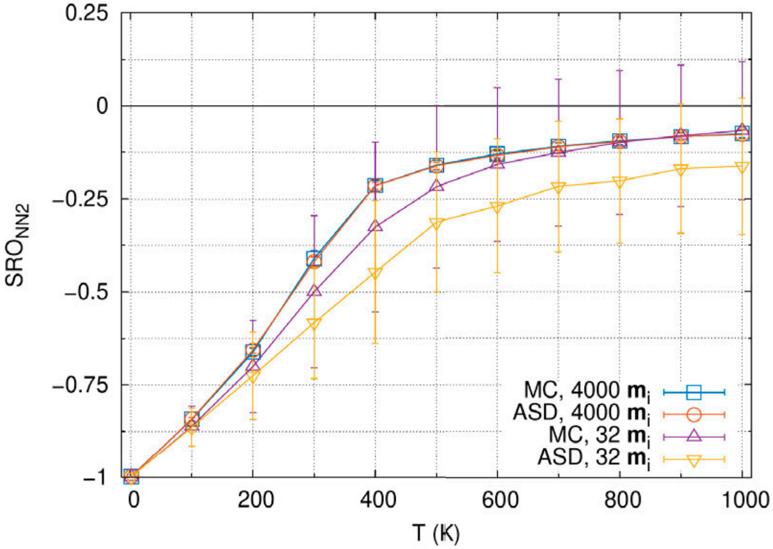

Figure 4.6: Magnetic SRO parameter in NiO for second nearest neighbors from MC and ASD simulations with cell sizes of 2x2x2 and 10x10x10 repetitions of the conventional fcc cell, for a total of 32 and 4000 moments, respectively.

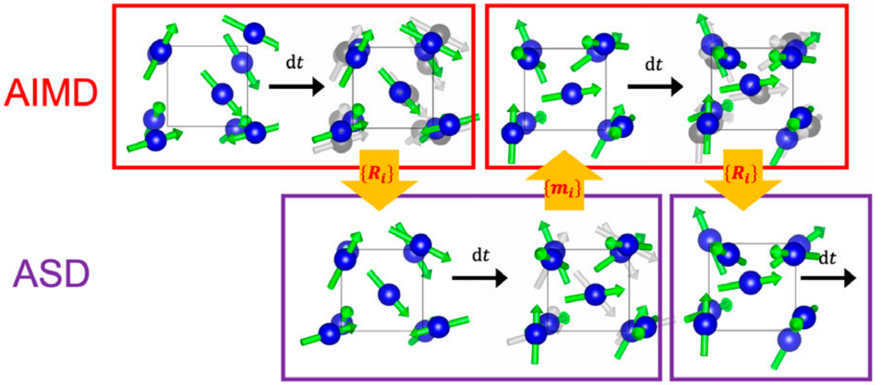

Figure 4.7: Schematic representation of ASD-AIMD simulations [91]. An initial pre-equilibrated magnetic $\{\mathbf{m}_i\}$ and atomic $\{\mathbf{R}_i\}$ configuration is used to perform an AIMD step keeping fixed the magnetic moment directions. From the new atomic positions, the distance-dependent J_{ij}s between each pair of moments are updated and an ASD simulation of the same length as the AIMD step is carried out. The new direction of the moments is fed back into the AIMD step, and the procedure is therefore reiterated for the whole duration of the simulation.

$$\mathbf{H}_{\text{eff}} = -\frac{1}{m_i}\frac{\partial H}{\partial \mathbf{e}_i}. \tag{4.14}$$

The size of the moments m_i enters implicitly in the LLG equations through the $\mathbf{H}_{\text{eff}}$ term and through the Heisenberg Hamiltonian H.

Employment of these equations in ASD simulations gives access to both thermodynamic and dynamic properties [65], commonly carried out on a static lattice. Concerning the thermodynamic properties, ASD gives the same results as MC in the limit of long simulations and large system size. However, finite-size effects are more pronounced in this type of simulation than in MC. As an example of this issue, I show in Fig. 4.6 the magnetic SRO for second nearest neighbor shell in NiO calculated with MC and ASD for two system sizes, 2x2x2 and 10x10x10 repetitions of the conventional fcc cell (only Ni atoms are magnetic, therefore in these simulations the O atoms are neglected) for a total of 32 and 4000 moments, respectively. The error bars in this plot indicate twice the standard deviation of the SRO in the simulation. The results of the two different methods for the large system agree perfectly, and in both cases the standard deviation of the SRO is smaller than the size of the symbols in the plot. Both MC and ASD overestimate the magnitude of the SRO when the small supercell is used, however, interestingly, the two methods do not agree with each other in this case. The reason for this must be in the fact that ASD, following actual dynamics of the moments, does not manage to sample configurations with smaller (in modulus) SRO since these configurations have high energy, therefore remaining in a lower energy state for most of the simulation. In MC this effect occurs on a smaller scale, since even configurations with small SRO have a chance to be sampled thanks to the randomness of the MC moves. Nonetheless, it can be seen that the error bars of the results from the small cells are very large and they contain the value of the large simulations, showing that still some configurations with the correct SRO are sampled.

The LLG equations can be used also in conjunction with Newton's equations of motion in what is known as spin-lattice dynamics. In this method, the Hamiltonian is composed of a lattice part, described often in terms of classical interatomic potentials, and a magnetic part, described with the usual Heisenberg Hamiltonian or its extensions. These simulations include both vibrational and magnetic DOFs; however, they inherit the problems of classical force fields with accuracy and reliability. To tackle the problem of transferability of potentials and accuracy, a coupled atomistic spin dynamics-*ab initio* molecular dynamics (ASD-AIMD) method was developed in Ref. [91].

In ASD-AIMD simulations, the spin and the lattice systems are developed in parallel and intercommunicate with each other. The evolution from ASD comes into the AIMD part with the direction of the moments used in the noncollinear DFT calculation that derives energy and forces. The effect of AIMD, more subtly, enters the ASD part via the distance-dependent exchange interactions, which must be parametrized beforehand. A schematic representation of the algorithm for this method is shown in Fig. 4.7.

A regular simulation starts with a pre-equilibrated configuration of the atoms by means of, e.g., DLM-MD. Then, the distance-dependent exchange interactions are assigned for each pair of atoms according to their distance and fed into a Heisenberg Monte Carlo simulation in order to get an equilibrated starting configuration of the magnetic moments. With this magnetic configuration, an AIMD step is performed, and from the new positions the exchange interactions are fed into the ASD code in order to perform a spin-dynamics simulation of the same duration of the timestep used in AIMD. Then the new magnetic configuration is used for the next AIMD step, and this procedure is reiterated for the whole duration of the simulation. The magnetic configurations from ASD are enforced in the AIMD with the use of the constraint explained in Sec. 2.3.1. One detail that has to be checked is the typical revolution time of the magnetic moments: the faster is the spin dynamics, the smaller will have to be the AIMD timestep in order to have reasonable magnetic component of the forces acting on atoms at each step of the simulation. Nonetheless, in general, a much smaller timestep has to be used in the spin dynamics part of the simulation (e.g., in bcc Fe I use 10^{-2} fs for ASD, compared to 1 fs in the AIMD run) because it leads to better numerical convergence of spin trajectories; this is not a computational problem since ASD simulations are much cheaper than AIMD ones.

5 | Structural disorder

The exponential increase of computational power of the last 30 years has enabled DFT calculations of systems with always growing number of atomic sites. This is very important for the proper description of magnetic and vibrational disorder, as well as defects and substitutional disordered alloys from first principles, since for these type of problems the unit cell of a material cannot be used and one needs to resort to supercells of considerable size, unless mean-field methods such as the coherent potential approximation (CPA) are used.

In this chapter, I will introduce the classification of defects and the methods used to investigate them in the context of DFT and thermodynamic models. In particular I will focus on point defects and dislocations, the defects investigated in this thesis. In addition, the role of vacancies in mass transport and another, more complex diffusion mechanism is described. The chapter ends with a small section on the definition and modeling of random alloys, which are not one of the main topic of this thesis, but are still very important also for the notions that are extended to the magnetic problem of paramagnetism.

5.1 Defects in crystalline materials

Every real material has regions in it that depart from the ideal crystalline arrangement of their symmetric lattice. These regions are known as defects, and they can manifest in many different forms. A common classification of defects is based on the dimensionality of the defective region at the atomic scale, with the three resulting categories:

1. Point defects: zero-dimensional defects where the defective region is of the size of one or a few atoms. They can be extrinsic or intrinsic, where the former involves the presence of foreign species to the crystal and the latter involves only atoms already present.

2. Line defects: the defective region in this type of defects has a one-dimensional character, with dislocations being the most prominent defects in this category. They enable plastic deformation in real materials.

3. Planar defects: two-dimensional imperfections in the crystalline lattice, different varieties are possible: grain boundaries, stacking faults, twin boundaries, to name a few. These defects are not investigated in this thesis, therefore they will not be discussed anymore.

Sometimes a fourth category of three-dimensional defects is included, however from the atomistic point of view these defects are not different from bulk materials or nanoparticles, therefore are excluded from the present list.

The technological importance of defects has already been stressed in Sec. 1.3. In the following, the discussion will focus on the description of these phenomena in the framework of Chapter 2 and 3.

5.1.1 Point defects

The first and foremost point defect that must be introduced is the vacancy: this consist of the absence of an atom on a lattice site, and is therefore an intrinsic point defect. Vacancies are thermodynamic defects, *i.e.*, they appear in the system just because of the rules of thermodynamics. These defects indeed increase the entropy of the system and therefore, with increasing temperature, they make the crystal more stable. The equilibrium concentration of vacancies c_{vac} at temperature T can be estimated from simple thermodynamic arguments to be:

$$c_{\text{vac}} = \exp\left(-\frac{G^f_{\text{vac}}}{k_B T}\right), \tag{5.1}$$

where G^f_{vac} is the Gibbs free energy of formation of a vacancy, which expresses the energy cost of forming such a defect in the crystal. This term is often approximated with the bare formation energy assuming that the other contributions in the Gibbs free energy of formation are negligible, although at temperatures approaching melting this approximation might not hold [46]. The equilibrium vacancy concentration in a material is usually very small: for a vacancy formation energy of 1 eV, the concentration of vacancies at 1000 K is of the order of 10^{-5}, and for a formation energy of 2 eV this value reduces to 10^{-10} at the same temperature. Often real materials will have a larger concentration of such defects due to the particular synthesis method or other external conditions.

The other types of intrinsic point defects are self-interstitial atoms and antisite defects. The former consists of an atom that has left its lattice position to go to some position in between other lattice sites, but this type of defect has usually very high formation energy compared to vacancies and therefore is not as important, except for extreme conditions as in nuclear reactors where they do become important due to radiation damage [92, 93]. They can also be part of more complex defects known as crowdion [94] that involve a few

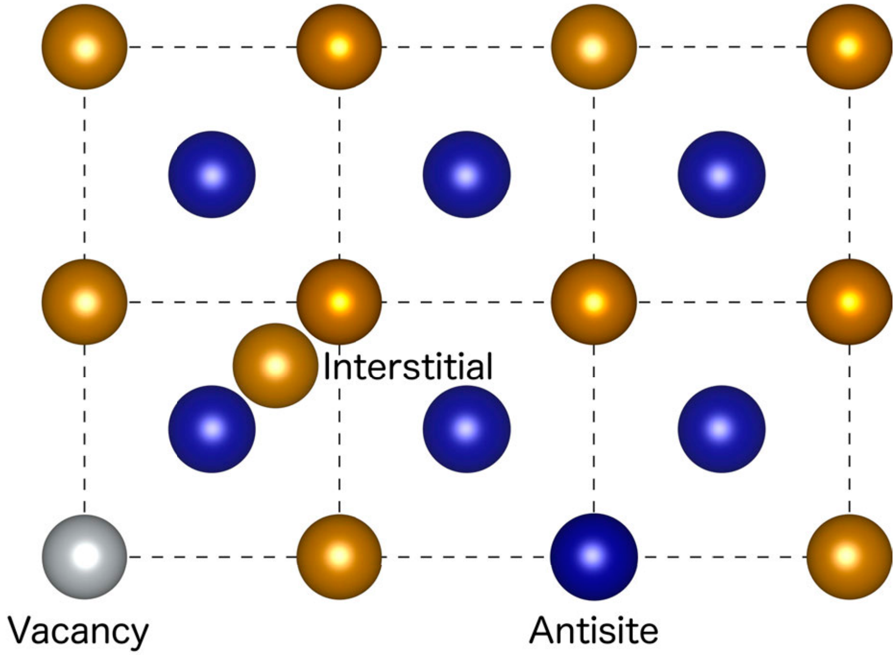

Figure 5.1: Schematic 2D projection of a CsCl structure with typical intrinsic defects: vacancy (white ball), interstitial and antisite defects. In this projection, the golden atoms are at position (0,0,1) and symmetrically equivalent, and the blue atoms are at position (1/2,1/2,1/2) and symmetrically equivalent. The interstitial defect is at position (3/4,3/4,3/4). The dashed lines indicate the conventional CsCl cells. No lattice relaxations around the defects are displayed in this figure.

atoms, or form at high temperatures promoting collective diffusion events, as is seen in Paper IV. The latter is possible only in compounds: if we think of an AB compound in which element A and element B belong to two distinct sublattices, then an antisite defect would be an A atom sitting in the B sublattice.

In addition to these defects, another important category of point defects is represented by extrinsic defects, where a foreign element is included in the crystal structure of the compound. Examples of these defects are the previously mentioned H impurities in Fe, which induce embrittlement, as well as doping of semiconductors with other elements to tailor conduction properties. These defects typically occupy the energetically least unfavourable positions available in the lattice, either substituting one atom from the compound on a lattice site (substitutional defect) or sitting in one of the interstitial positions mentioned earlier: which position the foreign atom takes depends on its size and the structure of the host material. As an example, in FM bcc Fe, the lowest energy position for an H interstitial is a tetrahedral site [95], for a B atom it is in a substitutional site, whereas for a C, N, or O atom it is an octahedral site [96].

For what concerns first principles calculations of defect properties, accurate modeling requires particular care for certain details to avoid spurious contributions deriving from the technical details of the computational method employed. As mentioned in Sec. 2.1, Bloch's theorem and periodic boundary conditions (PBC) enable the calculation of properties of a perfect infinite crystal by taking into account only the unit cell. Often point defects are present in the crystal at very low concentrations, the dilute limit, and without displaying an ordered arrangement; Bloch's theorem and PBC seems therefore incompatible with the modeling of defects. However, calculation of the properties of a defect in the dilute limit can be achieved by taking a supercell made of several repetitions of unit cells in all directions and introduce one defect in this simulation box. The validity of this method is ensured by the principle of "nearsightedness" [97], which states that a change in the potential at a point far away has a small effect on the region of interest. This seems to contradict quantum mechanics, for which eigenstates of a particle depend on the potential at any other point and on boundary conditions; however, for a many-body system, destructive interference between the wavefunctions of many particles reduces this nonlocal effect. An important thing to test therefore in calculations of defect properties is the size of the supercell: this means that the quantity of interest, say the formation energy of the defect, should be checked for convergence against the supercell size. Once convergence against system size is reached, one can assume that the point defect is not interacting anymore with its periodic images and the formation energy can be taken as the formation energy in the dilute limit.

It is important to consider as well the nature of the host material. For defects in metals, it is clear that only neutrally charged defects can be created, since any charge deriving from the defect would be delocalized in the material. However, this is not the case for a semiconductor or an insulator, therefore one should take into account also the possibility of charged defects in order to predict if the most stable defect is charged or neutral. In case of charged defects, even more careful convergence with supercell size is required since electrostatic interactions are long-ranged, and interaction with periodic images has to be avoided or explicitly compensated. Long-range interactions between defects might be present in metals as well: as an example, if magnetic impurities are placed in a nonmagnetic metal, these can indirectly interact with each other through spin-polarization of the conduction electrons of the host. This coupling is known as Ruderman-Kittel-Kasuya-Yosida (RKKY) interaction [10], and in supercells calculations it must be taken into account.

The formation energy of a defect E_{d}^{f} is defined with respect to the relevant chemical potentials μ_i, and it takes the general form (including the possibility of charged defects) [98, 99]:

$$E_{\mathrm{d}}^{f} = E_{\mathrm{d}} - E_{\mathrm{bulk}} - \sum_{i} n_i \mu_i + qE_{\mathrm{F}} + E_{\mathrm{correction}}, \tag{5.2}$$

where E_{d} is the energy of a supercell with the defect, E_{bulk} is the energy of a corresponding defect free supercell, and n_i is the number of atoms of type i removed or added in the defective supercell. For a defect of charge q, the chemical potential for electrons, i.e. the Fermi energy E_{F}, has to be included as well. A final correction term can be added, e.g., to remove strain energies [100] or electrostatic interactions [101, 102] due to periodic boundary conditions. It is good to stress at this point that the chemical potential of species i is the energy that an atom gains when it is added or removed from the reservoir that the system is in contact with. As an example, for a vacancy in an elemental solid such as bcc Fe, the chemical potential is of course the energy of bulk bcc Fe. If the system is, instead, a binary compound, the chemical potential can be trickier to calculate; in order to compare with experimental results one needs to know what is the reservoir in the experiment itself. The formation energy defined in this way can then be used to estimate the equilibrium concentration of a defect in the system at temperature T in the dilute limit with an Arrhenius equation as in Eq. 5.1.

Another important detail to take into account in the study of defects is structural relaxation. As it can be imagined, a defect in the lattice will lead to a local rearrangement of the surrounding atoms, and this is fundamental in the estimation of formation energies. Relaxations can be quite long ranged, therefore the size of the supercell plays an important role also on this effect. As an example, for C interstitials in FM bcc Fe, it is well known that a strong strain field is induced in the lattice [103], therefore large supercells and correction schemes [100] are needed in order to obtain accurate solubilities.

5.1.2 Dislocations

In this thesis, dislocations are yet another defect investigated in PM bcc Fe, trying to highlight the coupling between structural and magnetic disorder. A detailed presentation of this type of defects would require a lengthy description that is not particularly relevant for the scope of this work, therefore just a brief introduction to this topic is going to be given in this section. For a more accurate treatment, the reader is referred to, for example, Ref. [8, 104, 105].

As mentioned in the beginning of this chapter, dislocations are line defects known to govern plastic deformations in metals [104]. Their existence was speculated to solve a discrepancy between the theoretical and experimental shear stress needed to plastically deform a metal. Dislocations are characterized by their Burger's vector **b**, a vector indicating the displacement of the atoms in the defective structure from the ideal crystalline positions, which can assume different orientations with respect to the dislocation line: b can be perpendicular to the dislocation line, in which case the dislocation is called an *edge* dislocation, or parallel to the dislocation line, which is known as a *screw* dislocation; dislocations with orientations of b with respect to the dislocation line in between these two limits are called *mixed* dislocations.

Different crystal systems present predominance of different types of dislocations, since the symmetry of the system defines which are the close-packed planes and therefore the planes that can more easily slip with respect to each other. These planes are known as slip planes. In bcc metals, the close packed directions are the $\langle 111 \rangle$ directions, with shortest Burger's vector $\frac{1}{2}\langle 111 \rangle$. The slip planes in this system can be multiple, all containing the $\langle 111 \rangle$ direction.

Particularly important is the dislocation core, *i.e.*, the region in proximity of the dislocation line, since it governs the mobility of the dislocation in which elasticity theory fails. The description of dislocation cores requires atomistic simulations [105]; classical interatomic potentials have been shown to give very different answers regarding the stability of different configurations of the dislocation cores [104, 105], it is therefore desirable to employ first principles methods to establish the relative stability of the different configurations.

Ab initio methods are currently used to investigate core regions, although some precautions are required regarding the geometries and the PBC employed. Although it is customary to employ PBC in all directions to simulate a bulk system even with point defects, one single dislocation cannot be introduced under these conditions because the interaction with the periodic images would be too strong. For screw dislocations, two dislocations with opposite Burger's vectors are needed in the simulation box: this arrangement is known as a dislocation dipole. A particular choice of the simulation box vectors and of the dipole enables, under the application of PBC, the simulation of a quadrupolar arrangement that minimizes the interaction energy between periodic images [105]. This arrangement makes so that each dislocation is surrounded by dislocations with opposite Burger's vector in symmetrically equivalent positions, decreasing the long range elastic forces induced by the single dislocation. The importance of reducing as much as possible the elastic energy induced by the dislocation lies in both the need to avoid interaction with the periodic images and the availability of accurate methods based on elasticity theory to model this energy, whereas the intrinsic energy of the dislocation core can be calculated only with atomistic methods.

5.2 Diffusion in bulk systems

As often stressed in this thesis, atoms do not stand still in reality. One particularly important phenomenon concerning defects is their diffusion. This effect is particularly important for the strength of materials, as diffusion regulates the formation of clusters of defects (segregations) in the host material that could affect the properties of a device. In bulk close-packed systems, self-diffusion is known to happen through a vacancy: the exchange of two atoms in a close packed system is a very energetically expensive mechanism, whereas the jump of an atom onto a neighboring vacant site is a much more favourable process. Nonetheless, such a jump onto a vacant site requires overcoming an energy barrier. This barrier is generally large enough to make this process happen with a very low frequency as compared to the typical atomic vibrational frequencies, falling in the category of rare events; from the point of view of thermodynamics, in rare events the energy barrier is much larger than the thermal energy in the system.

The calculation of energy barriers by first principles is very often carried out with the nudged elastic band (NEB) method [106], which enables to find the minimum energy path to go from the initial to the final state. In this method, several images of the system are created, each with the diffusing atom in different positions going from the initial to the final state. The diffusing atom in one image is connected with fictitious springs to its replica in the neighboring image, in order to avoid the collapse of one image onto the other; all atoms in the supercell in each replica are allowed to relax. In addition, the component of the fictitious spring force perpendicular to the path is projected out, so that it does not influence the relaxation of the the diffusing atom in the direction perpendicular to the path. Several implementations [106, 107] of this method have been developed, as well as other methods that enable the calculation of minimum energy path or minimum free energy paths [108, 109]. Once the energy barrier is calculated, the diffusion rate D of a defect can be calculated employing transition state theory [110] using an Arrhenius equation:

$$D = A \exp\left(-\frac{\Delta G_d^a}{k_B T}\right), \tag{5.3}$$

where ΔG_d^a is the defect activation Gibbs free energy, and A a prefactor that takes into account the availability of sites for jumps, the jump attempt frequency and the jump distance. The activation free energy differs between extrinsic defects and thermodynamic defects: in the former case, this is just the migration free energy for diffusion, correspondent to the free energy of the transition state relative to the equilibrium state, whereas in the latter case is the sum of the migration free energy and the formation free energy. The entropic contribution to the activation free energy is often separated in Eq.

5.3 to arrive to the following expression:

$$D = A \exp\left(\frac{\Delta S_d^a}{k_B}\right) \exp\left(-\frac{\Delta E_d^a}{k_B T}\right) = D_0 \exp\left(-\frac{\Delta E_d^a}{k_B T}\right). \tag{5.4}$$

ΔE_d^a is the quantity that can be readily obtained with NEB calculations, and possibly including also the formation energy in case of intrinsic defects. Equation 5.4 enables the calculation of diffusion coefficients with *ab intio* NEB calculations combined with harmonic or quasi-harmonic phonon calculations through Vineyard transition state theory [111].

5.2.1 Diffusion close to the melting point: Ti vacancy diffusion in TiN investigated with the color diffusion (CD) algorithm

A problem that one can incur into when using Vineyard transition state theory is that at high temperatures, close to melting, anharmonicity becomes important. This effect cannot be included directly in transition state theory, but the issue can be in principle fixed with direct molecular dynamics simulations, although the problem of statistics arises when *ab initio* accuracy is wanted for rare events diffusivities. To fix the issue of statistics at high temperatures, I used in Paper I the CD algorithm described in Sec. 3.2.1.1 to calculate the jump rate of Ti vacancies in TiN. Ti vacancies in TiN are a good test case for this algorithm since the estimated energy barrier at 0 K is 4.26 eV, which is a very large barrier in this context. From the calculation of the jump rate for different temperatures (2200-3000 K) with the CD algorithm, and after fitting with Eq. 5.4, the resulting energy barrier is 3.78 ± 0.56 eV, which is slightly higher than the energy barriers obtained with NEB calculations with the 2200 and 3000 K lattice parameter, 3.67 and 3.50 eV respectively. The values calculated without explicit thermal vibrations are within the statistical uncertainty of the value from the CD simulations, and it seems to indicate that for Ti vacancies in TiN the main factor that changes the energy barriers at finite temperatures is thermal expansion, which can be easily included in calculations within the quasi-harmonic approximation.

5.2.2 Concerted migration in bcc Ti

The vacancy mechanism studied for TiN is not the only mechanism that can contribute to mass transport. In Paper IV, it was shown that a complex mechanism for self-diffusion occurs in bcc Ti at high temperatures. In this system, in fact, it was found that atoms collectively migrate through the crystal in lines or chains, or even by simple atom exchange (see Fig. 5.2 for a visual example of such migrations). This is of course not the only mechanism with which mass transport occurs, but it is present together with the usual vacancy-mediated jump and, at temperatures close to melting, it becomes the predominant mechanism of diffusion. This mechanism was first observed in

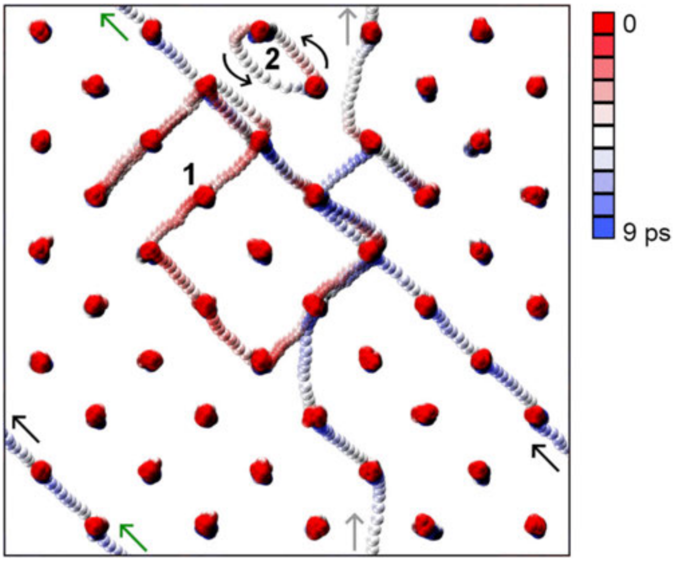

Figure 5.2: Examples of collective diffusion mechanisms in bcc Ti projected on the (001) plane from AIMD. The collective diffusion labelled "1" involves several atoms and atomic sites and the jumps are both on nearest and next-nearest neighbors sites, whereas the mechanism "2" is a simple exchange between two atoms. The color scale indicates when the diffusion occurred, over a total of 9 ps. Figure from Paper IV.

simulations of bcc Fe at pressures and temperatures believed to take place in the inner core of Earth [112], and later on it was observed in other bcc systems [113] and in simple cubic systems as well [114], suggesting that this mechanism is much more common than previously thought.

5.3 Random alloys

The theoretical modeling with first principles calculations of a random substitutional alloy requires great care due to lack of long range order, stochastic occupation of lattice sites, and presence of many different local environments. The first way that could come to mind to model such a system is to use several supercells with unbiased random number generated distributions of the different chemical species in the material, and then average the results over the different samples. This approach is in practice found to often require very large statistics, and much cheaper methods are available. Here we need to distinguish between two types of approaches: supercell methods and Green's function methods based on scattering theory. The latter include the CPA method previously mentioned, which consists in replacing the disordered lattice with an effective medium that reproduces the average scattering properties of the real atoms as embedded in the medium. This technique is much more elaborated than this easy explanation, but it has not been used in this work, therefore I redirect the interested reader to more detailed descriptions [115].

For what concerns supercell methods, the most efficient approach to represent chemical disorder is the so-called special quasi-random structure (SQS) [116]. In this method, the atoms of the substitutional disordered alloy are placed in the lattice so that the correlation function between each type of atom mimics the average correlation function in an infinite lattice, at least for the first few coordination shells. To be more clear, consider the simple example example of a random binary alloy $A_{0.5}B_{0.5}$. In such an alloy, one can expect that the nearest neighbors to an A atom will be on average half A atoms and half B atoms, and the same consideration can be done for every coordination shell included in the calculation. Therefore, one way to mimic this behavior is to populate the supercell under consideration so that the correlation functions are as close as possible to the result expected for an infinite lattice. Of course, this method is affected by the size of the supercell, since all the important interactions between shells need to be included [117]; however, it turns out to be much more efficient then the random distribution of atoms in a supercell of the same size. With a generalization of this method, one can as well reproduce different degrees of short range order.

One advantage of the SQS method over the CPA approach is that in the former structural relaxations can be easily performed. In a real crystal, the chemical disorder will induce local lattice relaxations, and this will affect the energetics of the system, similarly to what happens in calculations with defects (Sec. 5.1.1). If one then thinks to investigate the effect of a defect, say a vacancy, in a random alloy, then several SQS supercells with the vacancy positioned in different local environments need to be employed in order to have a proper modeling of the defect. A statistical average of the results from the several configurations can be then performed in order to improve the description.

Another method that has been developed in the past to study configurational disorder is the cluster-expansion method [118]. In this formalism, an alloy is described in terms of a collection of clusters, which can be univocally defined taking an orthonormal basis founded on discrete spin variables σ_i, defining the occupancy of a particular site i in the cluster. With this method, any property of an alloy can be decomposed in components along the orthonormal cluster basis functions, and once the relevant cluster interactions are obtained, thermodynamical properties can be obtained with the use of a generalized Ising Hamiltonian. For a more detailed presentation of the cluster expansion method, the reader is referred to, e.g., Ref. [117].

6 Magnetic disorder coupled with structural and vibrational degrees of freedom

The decoupling of different DOFs has been historically an important tool to pinpoint the origin of different effects. The most prominent example of such a decoupling is the Born-Oppenheimer approximation described in Sec. 2, with which the separation between electronic and nuclear DOFs has become a rule in the investigation of materials. However, this is still an approximation that was introduced to be able to solve the Schrödinger equation, and later on methods to lift this approximation in first-principles calculations were introduced [119]. Similarly, magnetism has been decoupled from the vibrational DOFs, and sometimes even from the electronic DOFs. The decoupling has been based on the fact that electronic DOFs are faster than magnetic (transversal) DOFs, which are faster than vibrational DOFs. This hierarchy of timescales suggests how to adiabatically separate the different effects. Nonetheless, the interplay between the different DOFs need to be investigated to resolve the question of whether or not the full coupling should be considered or not. This is the main aim of this thesis, and in this chapter I present the methods I developed and the main results from my own work. The chapter is divided in two parts, to stress the two types of coupling that I have investigated: the coupling of magnetic disorder with lattice structure, and with lattice vibrations.

The first part starts with the presentation of the DLM relaxation method, developed in Paper II, which enables the relaxation of the internal coordinates of a structure in the PM phase, modeled here with the DLM-MSM method [83]. The initial tests of the method are introduced, namely the single vacancy and the single C interstitial atom in octahedral and tetrahedral position in PM bcc Fe, as well as PM bcc $Fe_{1-x}Cr_x$ random alloys. After these benchmark tests, application of the DLM relaxation method to different systems in the PM state is presented. The first application is to a $1/2\langle 111 \rangle$ screw dislocation in bcc Fe in the PM state, in order to assess the effect of the change of magnetic state on this type of extended defect (Paper VI). The application of the DLM relaxation in the investigation of intrinsic and extrinsic point defects in CrN is then presented, with the aim of calculating electronic properties of this system of relevance for thermoelectric applications (Paper VII and VIII). Finally, the investigation of the compound Fe_3CO_7, newly synthesized at high pressures and believed to be important for Earth's mantle, is introduced (Paper IX).

The second part is concerned with the investigation of the coupling between magnetic disorder and lattice vibrations at high temperature. Initially I discuss the effect of lattice vibrations on LSF energy landscapes and moment sizes, studied in Paper V, in bcc Fe around T_C, liquid Fe just above melting, and liquid and solid bcc at Earth's outer and inner core conditions, respectively; starting from this work, a method to predict the LSF energy landscapes with a machine learning algorithm was developed in Paper X and it will be briefly discussed here. Finally, the calculation of free energy differences between bcc and fcc Fe with ASD-AIMD and thermodynamic integration is discussed, showing the delicate importance of finite temperature magnetism, vibrations, and their coupling, in the calculation of such quantity; these results are taken from Paper XI.

6.1 Local lattice relaxations in the paramagnetic phase

6.1.1 DLM relaxation

The magnetic state of a material can affect considerably its structure by changing the interatomic forces. A proof of this effect was shown in Ref. [85] for bcc Fe, where the interatomic force constants soften when going from the FM to the PM phase. This effect suggests that the magnetic state could affect local lattice relaxations around defects, in addition to vibrational properties.

Several approximations to the investigation of defects in the PM state in Fe and other systems have been employed in the years. One possible approximation is to carry out MSM calculations on FM-relaxed atomic positions [120], neglecting possible relaxations deriving from the PM state. Another method involved partial relaxation of the atomic positions employing different MSM configurations and averaging then the results obtained from these different coupled magnetic-atomic configurations [121]. The relaxations are allowed only partially in this case, to reflect the different timescales of magnetic and structural DOFs. Another approximation consisted in performing DLM-MD simulations on defective supercells, so that in this way also the effect of vibrations is taken into account [86, 89]. Finally, spin-wave calculations have also been developed [122, 123] for the representation of the PM phase; structural relaxations are here completely allowed for each spin-wave considered, but the description of this method is beyond the scope of this thesis. From a computational perspective, it would be good to have one single configuration of the atoms relaxed with the relevant magnetic state, on which one can then perform static calculations in line with what is routinely done for nonmagnetic systems.

For this reason, in Paper II we have developed a method to perform structural relaxations in the PM phase based on the DLM model (DLM relaxation). In particular, we use the MSM approach to represent the PM phase. In Fig. 6.1 a schematic representation of the relaxation algorithm is shown. In this method, the structural relaxation is started taking into account some initial positions of the atoms in a supercell containing the defect and drawing a random MSM configuration, either collinear or noncollinear (see top right part of Fig. 6.1). The initial positions could be the ideal lattice positions with the defect or positions pre-relaxed in the FM state, which can be often a good starting point. Forces are calculated with the present MSM configuration and symmetrized according to the symmetry of the underlying lattice in a spin-space average (SSA) fashion [85], and the atoms are moved according to these symmetrized forces. A new random MSM configuration is then taken, and the procedure is repeated, changing at every step the MSM configuration, until the atoms reach a regime in which they fluctuate around some mean value. This regime is shown in the bottom right part of Fig. 6.1, where the projection on the x-y plane of the position of one of the nearest neighbors to the vacancy in PM bcc Fe during the DLM relaxation is shown. In this figure, both a relaxation with full account of symmetry (solid lines and points) and and without account of symmetry (semitransparent lines and points) are shown. The green diamond indicates the position of this atom after FM relaxation, whereas the blue and the light blue diamonds mark the position after DLM relaxation with and without imposition of symmetry, respectively. These latest two positions are obtained from averaging the positions indicated with red circles, which correspond to the steady-displacement regime. It is striking how close the relaxed positions with and without symmetry are: this is due to the fact that the MSM configuration is changed at every step, acting on average according to the underlying symmetry also when forces are not symmetrized. More details can be found in Paper II.

More recently, Hegde *et al*. [124] developed a method similar to the present DLM relaxation, but based on the use of magnetic SQS supercells and the SSA averaging of the forces. In this SSA relaxation method, several relaxations of a magnetic SQS supercell with the vacancy placed in different positions are run in parallel, and at each step the forces from each calculation are averaged together and symmetrized according to the SSA method. The positive aspect of Hegde's method is that the final positions are obtained when the average forces are close to zero, which does never happen if one uses a single MSM configuration as done in the present DLM relaxation method. Nonetheless, the results on the vacancy formation energy in PM bcc Fe are

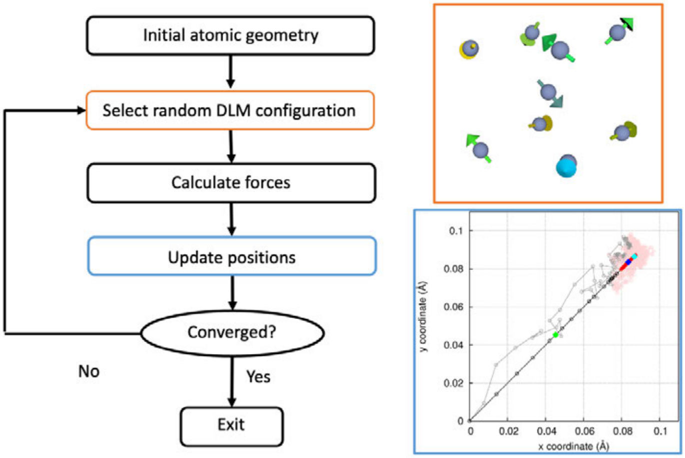

Figure 6.1: Schematic representation of the DLM relaxation algorithm. An initial atomic geometry is taken into account, and on these positions a calculation with a single MSM configuration (shown in the top right) is carried out. The forces are calculated and symmetrized, if needed, and the positions are updated (see bottom right part of the figure). This procedure is repeated with new MSM configurations at each step, and it is stopped when the displacements in the cell reach a steady state, fluctuating around a mean value (red empty circles in the bottom right figure). The final position (blue and light blue diamonds for symmetrized and non-symmetrized forces, respectively) is obtained as an average over this steady state regime. As a comparison, also the FM relaxed position is shown (green diamond). Bottom right figure adapted from Paper II.

virtually identical between the two methods, confirming the results obtained in Paper II.

6.1.2 Application to defects in bcc Fe and to $Fe_{1-x}Cr_x$

The DLM relaxation method was initially tested on the vacancy in PM bcc Fe. The local lattice relaxations around the vacancy are consistent, and there is a non-negligible difference between FM relaxed and DLM relaxed positions, as can be seen for the first nearest neighbor positions in the bottom right part of Fig. 6.1. For what concerns the formation energy, the strongest effect is still due to the change of magnetic state: the formation energy calculated on FM-relaxed positions with FM and PM state differs of approximately 0.5 eV, going from 2.2 to 1.7 eV. Employment of the DLM relaxation method induces a further decrease in the formation energy, going down to $\approx$ 1.6 eV. This result agrees with an average of experimental results, which should anyway

Table 6.1: Vacancy and C interstitial formation energy for FM and PM bcc Fe. PM bcc Fe is modeled in the present work with the DLM-MSM approach, and the formation energy is calculated on FM- and DLM-relaxed positions. The other theoretical values from literature are from DFT+DMFT calculations [56], collinear DLM calculations on FM-relaxed positions [120], and with the spin-wave (SW) method [123]. The experimental values here reported are an average of several experimental results [125–129]. For C interstitial, we are not aware of any other calculation in the PM phase. All values are in eV.

	FM (eV)	PM (eV)	
	FM-relaxed	FM-relaxed	DLM-relaxed
Vacancy			
This work	2.20	1.70 ± 0.06	1.61 ± 0.06
DFT+DMFT [56]	2.45	1.66 ± 0.15	1.56 ± 0.13
DLM [120]	2.15	1.54 ± 0.16	
SW [123]	2.13	1.98	
SSA [124]	2.15	1.71	1.62
Exp. [125–129]	1.8	1.6	
C interstitial			
Octahedral site	0.68	0.59 ± 0.07	0.41 ± 0.06
Tetrahedral site	1.55	1.04 ± 0.07	0.62 ± 0.06

be taken cautiously as show in Ref. [46], but more interestingly agrees with the vacancy formation energy from DFT+DMFT calculations with some local lattice relaxations allowed [56] and, as previously mentioned, with the SSA relaxation method of Hegde *et al.* [124]. These results and the results from literature are summarized in Table 6.1.

In Table 6.1 the results of the formation energy of a C interstitial in octahedral and tetrahedral positions are also shown. In the cases, a stronger effect of the DLM relaxation is observed: it can be seen that the formation energy in octahedral position decreases more due to the DLM-relaxed positions than from the change of magnetic state. The formation energy of the C interstitial in tetrahedral position shows an even larger decrease than the octahedral position, and the final formation energy is only 0.2 eV larger than for this latter site. This similarity in formation energies could have implications on the high-temperature phase of steels, but no further implications are discussed here.

An interesting effect on thermodynamic properties arises in bcc $Fe_{1-x}Cr_x$ random alloys at the magnetic transition. It is known that in this system the change of magnetic state induces a qualitative change in the mixing enthalpy as a function of x [84, 130], with the alloy in FM state displaying a small region with negative mixing enthalpy, while it is positive for all concentrations

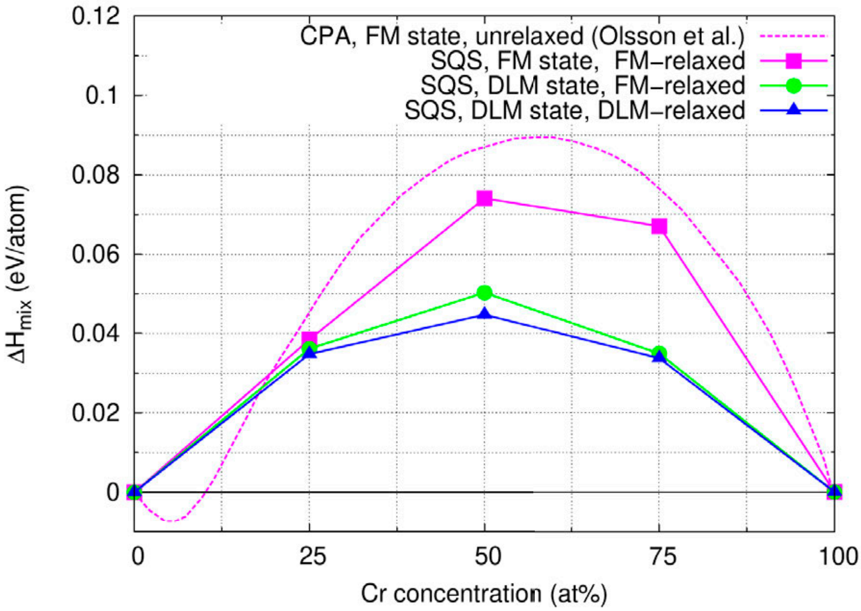

Figure 6.2: Mixing enthalpy of bcc $Fe_{1-x}Cr_x$ random alloys from Olsson *et al*. [130] (purple dashed line) and from Paper II (solid lines and symbols). Purple lines and squares mark results in the FM state, whereas green and blue symbols and lines for the DLM state. The dashed line corresponds to EMTO-CPA calculations on unrelaxed positions. Solid lines and symbols are results from Paper II, where chemical disorder was modeled with SQS supercells. In particular, green circles are from DLM calculations on FM-relaxed positions, and blue triangles to DLM calculations on DLM-relaxed positions. The DLM-MSM method was employed to model the magnetic disorder.

in the PM state. This effect makes the bcc $Fe_{1-x}Cr_x$ system a perfect candidate to test the DLM relaxation method. Nonetheless, the inclusion of relaxation in the DLM state does not change qualitatively this picture but only quantitatively, with a small reduction of the mixing enthalpy compared to the DLM results on FM-relaxed positions, as shown in Fig. 6.2. In this figure, the result for FM alloys from Ref. [130] (dashed line) were calculated modeling the chemical disorder with the CPA approach, whereas in my calculations (solid lines and symbols) I used the SQS method described in Sec. 5.3. In the former method, lattice relaxations are not taken into account, partly motivating the discrepancy with the results from my work. Another possible source of discrepancy is due to the different methods employed in the calculations, the exact muffin-tin orbitals (EMTO) in Olsson *et al*. [130] as opposed to the PAW method in my calculations.

After testing this method on simple cases, one can turn the attention to more complex defects like dislocations. Since the DLM state has an impact on the local lattice relaxations in the case of point defects, it is required to test if a similar effect occurs in the case of dislocations, which was investigated in Paper VI. In bcc Fe and, more in general, in bcc metals, the $1/2\langle 111 \rangle$ screw dislocation is known to be the main type of dislocation, although there is no general agreement in the literature on the structure of the core [105]. We investigated therefore the easy and the hard core configurations of this dislocation in the FM and the PM states, the latter modeled with the DLM-MSM method and relaxed consistently with the DLM relaxation method. In the FM state, it is known that the stable configuration is the easy core configuration, whereas the hard core results unstable. In our calculations, the hard core configuration becomes stable in the DLM state, although still at higher energy compared to the easy core configuration. The energy difference between the two configurations slightly reduces as compared to the FM state, from 40 meV/b to 26 ± 20 meV/b, although the FM result is within a 95% confidence interval of the DLM result. In addition to the considerable effect of the change of magnetic state on the structure and energetics of the dislocation core, there is an interesting change of trend in terms of magnetic moment sizes around the core. In the FM state, the atoms closest to the dislocation line are the ones with the largest moments, as expected due to a larger Voronoi volume of these atoms deriving from the defective structure. In the PM state, on the contrary, the atoms near the dislocation line are the ones with the smallest moments. This difference could have important effects in the case of magnetic impurities segregated at the dislocation.

6.1.3 Intrinsic and extrinsic defects in CrN for thermoelectric applications

The thermoelectric effect consists in the generation of an electric potential difference under the effect of a temperature gradient (and viceversa) [8]. Thermoelectric devices, which harvest thermal energy into electricity, are nowadays employed in several applications when requirements on the efficiency of the device are not fundamental but small sizes are needed, or where there is a consistent heat waste that can be turned into electrical power [131]. Thermoelectric coolers are also widely employed in many applications. The efficiency of a thermoelectric material at temperature T is defined with its dimensionless figure of merit ZT:

$$ZT = \frac{S^2\sigma}{\kappa_e + \kappa_l} T, \tag{6.1}$$

where S is the Seebeck coefficient, σ is the electrical conductivity, κ_e and κ_l are the electronic and lattice thermal conductivities, respectively. The numerator $S^2\sigma$ is often referred to as power factor. The Seebeck coefficient is defined as the voltage difference per unit temperature gradient, $S = \Delta V/\Delta T$; on the microscopic level, this coefficient can be connected with the slope of the DOS at the Fermi level [132]. Improvement of the figure of merit requires maximization of the numerator and simultaneous minimization of the denominator, although the different quantities are interconnected and often improvement in one factor leads to a deterioration of another factor. As an example, it is easy to imagine that an increase in electrical conductivity due to a higher concentration of carriers can lead to an increased electronic thermal conductivity, leaving the figure of merit unchanged. In addition, a too large increase of the electrical conductivity reduces the Seebeck coefficient, cancelling out any improvement in the power factor.

Nitrides have been in the last years investigated for their thermoelectric properties [131]. In particular, CrN has received considerable attention due to its promising properties like its intrinsically high power factor [131] and low thermal conductivity, where the latter is originating both from its crystal structure [133] and from enhanced scattering of phonons due to magnetic disorder [91]. CrN is an antiferromagnetic semiconductor, with a low temperature orthorombic structure. Around 280 K [134], the system transitions to a PM phase and rock-salt structure, with the two transitions correlated with each other [134]. N vacancies are the most common defect in this material, and they are known to induce a n-type behavior [89] (see left figure in Fig. 6.3), which could partially explain the tendency of CrN to display negative Seebeck coefficient.

The introduction of point defects in structures to enhance the thermoelectric properties of a material is a well-known procedure [135] that generally aims at increasing the charge carrier concentration and reduce the lattice thermal conductivity due to phonon scattering by defects. One method to improve the thermoelectric properties is by alloying with other elements: for this reason, in Paper VII, we investigated the effect of V alloying in CrN thin films. Since CrN is in its PM phase at operating temperatures, we investigated the effect of V substitutional defects on the metal sublattice with the DLM relaxation method and MSM calculations. In addition, we took into account also the possibility of having a N vacancy in the vicinity of the V atoms. In the presence of a V impurity, we observe the appearance of a small peak in the partial DOS around the Fermi level, due to the V 3d-states. This peak shifts to lower energies when also a N vacancy is present in the system (Fig. 6.3, right figure), however it is found in its vicinity, and we argue that it could have a role in the experimentally observed large Seebeck coefficient for (Cr,V)N alloys.

On the other hand, in Paper VIII we investigated with the same theoretical means the effect of intrinsic defects on the electronic properties of CrN thin films. Experimentally, it was found that CrN overstoichiometric in N displays a p-type behavior, which is uncommon for this semiconductor since it is often synthesized understoichiometric and with n-type character. To try

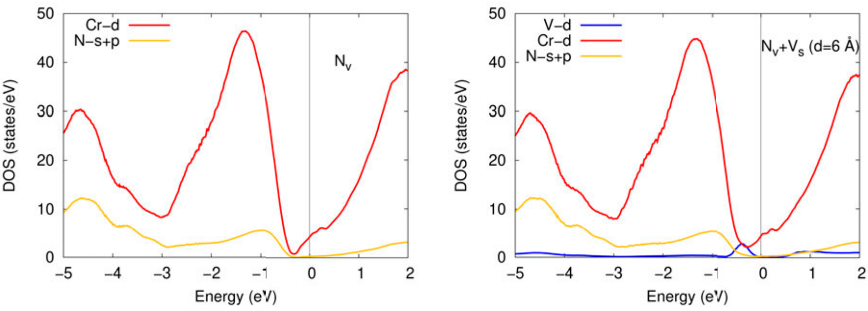

(a) (b)

Figure 6.3: Partial DOS of CrN with a N vacancy (top) and with a V substitutional atom on the metal sublattice and simultaneously a N vacancy. The red lines are the partial DOS of Cr 3d-orbitals, the yellow line of N 2s- and 2p-orbitals, and the blue line of V 3d-orbitals. Figures from Paper VII.

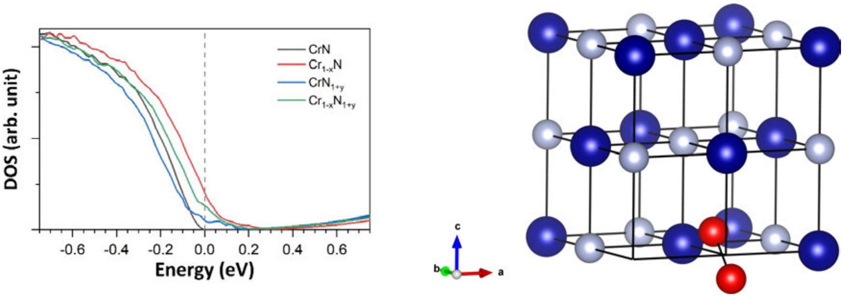

(a) (b)

Figure 6.4: (Left) Total electronic DOS of defect free CrN (black), CrN with a Cr vacancy ($Cr_{1-x}N$, red), CrN with a N_2 dumbbell (CrN_{1+y}, blue), and CrN with both defects ($Cr_{1-x}N_{1+y}$, green). The configuration of the combined defect is shown in the right part of the figure, where the Cr vacancy is positioned at the (0,0,0) position and the N_2 dumbbell is positioned at the neighboring lattice site (1/2,0,0). Blue balls are Cr atoms, grey and red balls are N atoms. Figures from Paper VIII

to explain these experimental findings, we investigated with DLM relaxation and MSM calculations the relative stability of defects that can induce the N overstoichiometry, namely the Cr vacancy, the N interstitial in the form of a N_2 dumbbell (referred simply as N_2 dumbbell, see *e.g.* Fig. 6.4b), and some combinations of these two defects. We have found that the Cr vacancy is energetically the most stable among the considered defects, and in addition this defect pushes the Fermi level into the valence band, making the system p-type (left plot in Fig. 6.4a, red line). However, experimentally, the lattice parameter and the Seebeck coefficient increase with increasing N content, whereas the Cr vacancy induces a reduction of the lattice parameter. Since the experimental synthesis is performed at conditions far from equilibrium, we cannot rule out the presence of N_2 dumbbells in the system, which could explain the lattice parameter increasing with N content. However, the N_2 dumbbells provoke a slight n-type behavior in this system, as seen from the blue curve in Fig. 6.4a. To try to explain the experimental findings, we tested the possibility of having both a Cr vacancy and a N_2 dumbbell nearby in the lattice. First of all, we found that this combination of defects in a particular disposition, shown in Fig 6.4b, has a particularly strong interaction energy, suggesting that the two defects want to be near each other. In addition, the effect of the combined defect on the DOS (green line in Fig. 6.4a) is similar to the single Cr vacancy, shifting the valence band to higher energies as compared to the defect free system (black line). In this investigation only four combinations of the Cr vacancy and the N_2 dumbbell were considered, however more complicated combinations could be present in this system; nonetheless, our results suggest that the Cr vacancy and the N_2 dumbbell are the main protagonist in this effect, in particular together.

6.1.4 Fe_3CO_7

High pressure physics is a branch of physics which allows to unravel fundamental principles of solid state matter and enables the investigation of systems that are otherwise not directly accessible. Examples of this latter scope of high pressure physics involve the study of compounds that are believed to be found inside the Earth, in its core or in its mantle, for example. Under the Earth's crust, high pressures and high temperatures are found, with increasing intensity the deeper inside one looks. The Earth's inner core, made mainly of Fe, is believed to be at temperatures of 6000 K and pressures of about 300 GPa [136], inconceivable values compared to everyday life conditions.

This type of temperatures and pressures can be accessed in laboratory only with laser-heated diamond anvil cells [137], although the samples that can be employed in these experiments are usually of micrometer size. Nonetheless, this experimental technique has been able to shine light on interesting phenomena happening at high pressures.

DFT calculations are very valuable in this context. Because of the complicated experimental setup, only certain quantities can be measured, and therefore theoretical calculations are needed to interpret the results of these experiments [138]. As an example of such an investigation, in Paper IX we reported the synthesis of several polymorphs in the Fe-C-O system and the theoretical study of one of these structures, the previously unknown compound Fe_3CO_7. This compound was synthesized at 47 GPa and 2000 K, and it was detected after quenching to low temperatures. *In situ* X-ray diffraction revealed that the structure is monoclinic and the stoichiometry suggests uncommon valencies of the elements. Further spectroscopic measurements hinted at Fe_3CO_7 being in the PM state.

To show that the experimentally determined atomic positions are of relevance, a DLM relaxation of the structure was performed with a modified version of the DLM relaxation algorithm. In this case, a method more similar to the one by Hegde *et al.* [124] was employed, using at each step of the relaxation ten different MSM configurations randomly drawn and averaging the forces from these calculations at each atomic site without account of symmetry. The final structure displays local relaxations that are virtually undetectable by experimental techniques, although the atomic forces strongly decrease during the relaxation, supporting the experimental conclusions on the structure of this compound.

The Fe atoms in this compound occupy two inequivalent positions in the structure and show distinct properties. From DFT+U calculations, one type of Fe shows a very large magnetic moment of $\approx 4\mu_B$ and it is compatible with a high-spin, insulating state, whereas the other type has a lower moment of $\approx 2\mu_B$, indication of a intermediate/low spin state and of metallic character. In addition, DFT+DMFT calculations showed that some O atoms do not posses the usual valency of 2-, rather they are more compatible with a formal charge of 1.5-: this result motivates the unusual stoichiometry, with oxidation states of the atoms different from usual chemical reasoning. The DFT+U results are in very good agreement with DFT+DMFT calculations carried out on the experimentally-determined positions. The electronic DOS calculated with DFT+U and DFT+DMFT are in fairly good agreement, considering the strong differences in the methodology.

6.2 Coupling of magnetic disorder and vibrations

The second main topic of this thesis concerns the coupling of magnetic disorder with vibrations. Magnetism is in principle a manifestation of the underlying electronic structure, as seen in Chapter 4, but in practice it can be treated as a separate DOF. However, simultaneous treatment of magnetic and electronic DOFs as a function of temperature is not trivial with DFT calculations. Vibrations add on top of this a further level of complexity by inducing different atomic local environments as compared to ideal lattice position: the change in local environment induces therefore a change to the local electronic and magnetic properties of the material. A hierarchy of timescales can be established to simplify the treatment of the different DOFs: electronic DOFs are faster than magnetic DOFs, which in turn are faster than vibrational DOFs. This separation of timescales allows to consider an adiabatic coupling between the different DOFs. Discussion of inclusion of the coupling of all the mentioned DOFs is the main goal of this section, where I will describe how vibrations affect the LSF energy landscapes and therefore the finite-temperature size of the magnetic moments, and how the calculation of free energy differences in Fe can be carried out with the full coupling of magnetic and vibrational DOFs.

6.2.1 LSF on a vibrating lattice and prediction of LSF landscapes with a machine learning algorithm

The theory of LSF was introduced in Sec. 4.3.2 for a static lattice. In Paper V, we investigated the effect of vibrations on the energy landscapes of Eq. 4.6 in Fe at very different conditions: we investigated bcc Fe just above the Curie temperature and liquid Fe just above the melting point at ambient pressure, as well as liquid Fe at conditions expected in Earth's outer core ($P \approx 200$ GPa, $T \approx 6000$ K), and solid bcc Fe at conditions of the Earth's inner core ($P \approx 300$ GPa, $T \approx 6000$ K). Motivated by the high temperatures at play, the study is conducted in the PM state so that the part of the Hamiltonian with the exchange interactions, Eq. 4.5, can be neglected in the thermodynamic treatment of the moment's size, although this is an approximation since SRO effects are to be expected in some of the cases under consideration.

Taking bcc Fe around the Curie temperature as the test case, we investigated the effect of vibrations on the landscape by taking a snapshot from an ASD-AIMD simulation at $T \approx T_C = 1043$ K and we calculated the dependence of the on-site energy $E_i(m_i)$ on the moment size m_i, corresponding to the energy landscapes shown in Fig. 4.5, for each moment in the supercell (54 atoms). The calculation of the landscapes was performed by focusing on one moment at a time and carrying out constrained calculations where the size of all the moments in the cell was kept constant to the initial value obtained from ASD-AIMD, together with their direction, and varying the size of the moment under investigation. The energy-moment size data were then interpolated with a quartic polynomial with only even powers, and the resulting energy landscapes for this system are shown in the top left part of Fig. 6.5. Inspection of this plot reveals a close connection between the local Voronoi volume of the atom and the shape of the landscape: more itinerant-like moments are associated with smaller Voronoi volumes, more localized moments occur for larger volumes. A striking feature is related to the appearance of two itinerant landscapes, with minimum energy for $m_i = 0\mu_B$, showing that lattice vibrations can have such a strong effect on local properties that they can change the landscape of a Fe moment from localized, as it usually is in bcc Fe, to itinerant.

Once the landscapes are calculated for each moment, one can apply the thermodynamic model explained in Sec. 4.3.2 to calculate the size of the magnetic moments at the simulated temperature according to the instantaneous landscape. Since we employ a thermodynamic model, there is no real dynamics in the longitudinal DOF, therefore the best choice for the output size

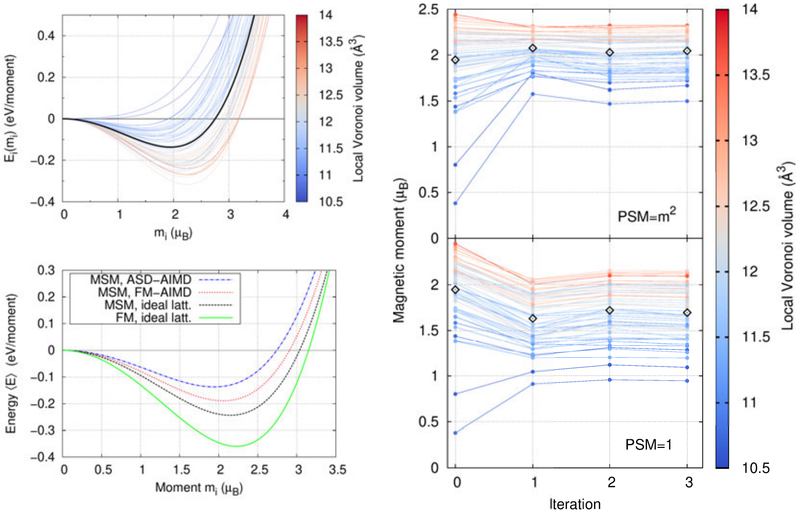

Figure 6.5: (Top left) Energy landscapes for each moment in a snapshot from ASD-AIMD of bcc Fe at $T \approx T_C$. The color scale indicates the local Voronoi volume of the moment, and the black line is the average landscape. (Right) Moments' sizes at finite temperature from the LSF thermodynamic model through the the whole optimization procedure for both PSM. Selfconsistency is reached when the moment sizes change for less than $0.01\mu_B$ from one iteration to the other. (Bottom left) Average landscapes from the first iteration of the top-right figure (MSM, ASD-AIMD, blue dashed-dotted line), from MSM calculations on atomic positions from FM-AIMD (red dotted line), from MSM calculations on ideal lattice positions (black dashed line), and from FM calculations on ideal lattice positions (green solid line). The average landscape becomes shallower and shallower with increasing degree of disorder. Figures from Paper V.

of the moment is to employ the average moment for the given landscape, calculated as:

$$\langle m_i(T)\rangle = \frac{1}{Z_i}\int_0^\infty \mathrm{d}m_i \; \mathrm{PSM}\; m_i e^{-\frac{E_i(m_i)}{k_B T}}, \tag{6.2}$$

where all the quantities were introduced in Sec. 4.3.2. Employing the average moment, in this case, is an approximation based on the assumption that the longitudinal DOFs are adiabatically coupled to the landscape: on the timescales of a typical MD timestep, the moment is able to experience the whole landscape, and therefore employment of the average moment as an expectation value is justified. It should be stressed here that each single moment has a different landscape, therefore the average moment is different for each atom due to its unique environment. Nonetheless, this is an assumption, and the dynamics of the longitudinal DOF should be investigated with higher-level theories, such as time-dependent DFT or quantum Monte Carlo methods, to have a direct confirmation of the validity of this assumption.

At this point, all the moments in the cell have a slightly different size as compared to the initial configuration. We therefore reiterated the procedure until every moment does not change of more than $0.01\mu_B$ as compared to the previous iteration. In order to obtain the average moment, one needs to choose a PSM: for a localized moment, this should be the one-dimensional PSM$=1$, but for an itinerant moment it should be the three-dimensional PSM$=m^2$. Since in the present case we found both itinerant and localized landscapes, we tested both PSM. The three-dimensional PSM leads to slightly larger moments compared to the initial ASD-AIMD result (top right of Fig. 6.5), whereas with PSM=1 this tendency is inverted (bottom right of Fig. 6.5). Nonetheless, also in this second case, particularly small moments are enhanced. On average, we observe that an increasing degree of disorder in the system leads to shallower and shallower landscapes. In the bottom left part of Fig. 6.5, the average landscapes from calculations with different degrees of disorder on the magnetic and lattice degrees of freedom are shown: the deepest landscape is found for FM moments on ideal lattice positions, followed by MSM landscapes on ideal lattice positions. The shallowest landscape is found for MSM calculations on ASD-AIMD positions, and slightly below this we find the landscape for MSM calculations on positions obtained from a FM-AIMD simulation.

Application of this scheme to the other systems leads to a general increase in the magnetic moments size compared to straightforward DFT calculations, even in the case of solid and liquid Fe at Earth's core conditions, for which straightforward DFT calculations predict absence of any magnetic effect.

The previous results show the need of knowing the LSF landscapes at every step of a dynamic simulation. Nonetheless, such a tedious calculation of energy landscapes cannot be performed at every step, since tens of thousands of such steps are often needed. For this reason, we developed a machine learning (ML) algorithm that aims at predicting the energy landscapes for each moment in the system taking as input the atomic and magnetic structure at a given timestep. The ML scheme can be included in ASD-AIMD simulations where each moment is constrained at every step to the instantaneous average moment of Eq. 6.2 for its own landscape, as predicted by ML. A schematic representation of such ASD-AIMD-MLLSF simulation is presented in Fig. 6.6.

The choice of the descriptor entering as input in the ML algorithm is of particular importance. The descriptor should have all the information about the local environment of a particular atom, both in terms of lattice and magnetic DOFs. We tested several types of descriptors, and the best performances were obtained for a descriptor that included the Voronoi volume of the atom under consideration (the central atom), the position of its first

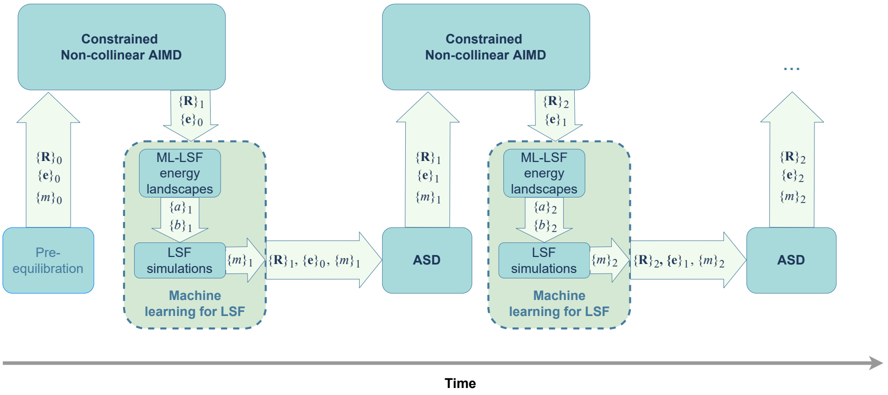
Constrained Non-collinear AIMD
{R}_0 {e}_0 {m}_0
Pre-equilibration
{R}_1 {e}_0
ML-LSF energy landscapes
{a}_1 {b}_1
LSF simulations
{m}_1
Machine learning for LSF
{R}_1, {e}_0, {m}_1
{R}_1 {e}_1 {m}_1
ASD
Constrained Non-collinear AIMD
{R}_2 {e}_1
ML-LSF energy landscapes
{a}_2 {b}_2
LSF simulations
{m}_2
Machine learning for LSF
{R}_2, {e}_1, {m}_2
{R}_2 {e}_2 {m}_2
ASD
...
Time

Figure 6.6: Schematic representation of a ASD-AIMD simulation with moment sizes predicted with the ML algorithm. Figure from Paper X.

nearest neighbors, and the sum of the scalar products between the magnetic moment of the central atom and the moments on the neighboring atoms. The other descriptors tested included more information than this, like the full direction of the neighboring moments or all the scalar products rather than just the sum; nonetheless this descriptor worked better. The reason for its better performance is probably due to the fact that some symmetry properties are taken into account when employing just the sum of the scalar products of the moments, whereas more detailed descriptors can recognize environments related by symmetry transformations as very different environments. In addition, the size of the training data set could also affect the performances of the different descriptors. In addition, the sum of the scalar products has a direct connection with the effective field experienced by the central atom, which can be obtained from the Heisenberg Hamiltonian (Eq. 4.2 and Eq. 4.14:

$$\mathbf{H}_{\text{eff}}(\mathbf{m}_i) = \sum_j \tilde{J}_{ij}\mathbf{m}_j \tag{6.3}$$

The ML algorithm to predict the LSF landscapes was then used in combination with ASD-AIMD simulations (ASD-AIMD-MLLSF) to carry out a finite temperature simulation for bcc Fe around T_C and for bcc Fe at Earth's inner core conditions. In the former case, we see a strong effect of the ASD-AIMD-MLLSF scheme on the mean square displacement of the atoms as compared to FM-AIMD; in the latter, a comparison of the pressure from NM-AIMD and ASD-AIMD-MLLSF reveals a discrepancy of approximately 40 GPa between the two different simulations, with possible implications regarding the understanding of the density of Earth's inner core.

6.2.2 Phase stability in Fe

The calculation of Gibbs free energy differences with first principles methods is a particularly challenging task to carry out, even more with magnetic materials, since in this case a further DOF has to be taken into account. Fe is the archetype of magnetic materials, and therefore methods are often tested on this system in order to show their accuracy. In addition, in Fe a double transition $\alpha \rightarrow \gamma \rightarrow \delta$ occurs at ambient pressure as a function of temperature, making it the ideal candidate to benchmark methods for the calculation of free energy differences.

The Gibbs free energy difference at ambient pressure ($P \approx 0$ GPa) can be expressed as:

$$\begin{aligned} \Delta G^{\text{fcc-bcc}}(P=0,T) = \Delta F^{\text{fcc-bcc}}[V_{\text{eq}}(T_0),T] + \Delta F^{\text{fcc}}[V_{\text{eq}}(T),V_{\text{eq}}(T_0)] \\ - \Delta F^{\text{bcc}}[V_{\text{eq}}(T),V_{\text{eq}}(T_0)], \end{aligned} \tag{6.4}$$

where $\Delta F^{\text{fcc-bcc}}[V_{\text{eq}}(T_0),T]$ is the free energy difference at the constant volume V_{eq}, which is the equilibrium volume at temperature T_0, and $\Delta F^{\text{struct}}[V_{\text{eq}}(T),V_{\text{eq}}(T_0)]$ is a correction to the free energy due to volume expansion, which is given by:

$$\Delta F^{\text{struct}}[V_{\text{eq}}(T),V_{\text{eq}}(T_0)] = -\int_{V_{\text{eq}}(T_0)}^{V_{\text{eq}}(T)} P(T,V)\mathrm{d}V. \tag{6.5}$$

This correction is needed to achieve zero pressure, where G and F coincide. We calculate the Gibbs free energy difference between fcc and bcc Fe as a function of temperature by carrying out ASD-AIMD simulations at temperatures from 800 to 1800 K, in steps of 100 K. The simulations are performed at constant volume, employing the equilibrium volume of each structure at temperature $T_0 = 1000$ K, for which both bcc and fcc Fe are already in the PM state in our model. Experimentally, bcc Fe has a Curie temperature of 1043 K, however with the exchange interactions employed here the magnetic transition results to be a bit below 800 K. It is well known that the α to γ transition, occurring at 1185 K [139] is driven by the magnetic transition [55], therefore we cannot expect to obtain the α to γ transition correctly due to the underestimation of the Curie temperature.

The problem is now to calculate the free energy difference $\Delta F^{\text{fcc-bcc}}[V_{\text{eq}}(T_0),T]$ as a function of temperature. Since we are mainly interested in free energy differences, rather than absolute values, we decide to employ the SSTI method of Sec. 3.3.1.2. The problem that raises here concerns the magnetism of the intermediate structures employed in this method: how does one define the exchange interactions for such intermediate structures without carrying out long and tedious calculations of the distance dependent J_{ij}s? One possible way to overcome this problem is to perform the SSTI in the DLM state, carrying out DLM-MD simulations rather than ASD-AIMD simulations, and then connect the free energy difference in the DLM state to its finite temperature magnetism (FTM) counterpart. To connect the DLM and FTM states, we propose to calculate the free energy difference between them for each structure, $\Delta F^{\text{struct}}_{\text{DLM-FTM}}[V_{\text{eq}}(T_0), T]$, with a magnetic TPT (mTPT) method.

To explain the mTPT method proposed here, one can start by neglecting the atomic displacements at finite temperature and consider only the magnetic DOFs. The DLM approach represents an ideal PM state where all the correlation functions are zero, corresponding to the limit $J/T \to 0$: in principle this can be modeled either by reducing the exchange interactions to zero or increasing the temperature to infinity $T \to \infty$. Considering the former of these two ways, the magnetic Hamiltonian for a DLM state results to be:

$$H_1 = H_{\text{DLM}} = 0, \tag{6.6}$$

which means that for any arrangement of the magnetic moments, the energy is always zero. The FTM system can be represented with the Heisenberg Hamiltonian:

$$H_0 = -\sum_{i \neq j} J_{ij} \mathbf{e}_i \cdot \mathbf{e}_i. \tag{6.7}$$

These two Hamiltonians can then be employed in the TPT equation, Eq. 3.24, where the sampling of the phase space is done with the Heisenberg Hamiltonian. To test the feasibility of this method, we carried out MC simulations for a simple cubic structure with only first nearest neighbor interactions, $J_1 = 10$ meV, and we calculated the free energy difference between DLM and FTM system with TPT. The free energy difference from the DLM state can be also obtained by calculating the entropy difference by integration of the specific heat:

$$\begin{aligned}\Delta F_{\text{DLM-FTM}}(T) &= \Delta E_{\text{DLM-FTM}}(T) - T\Delta S_{\text{DLM-FTM}}(T)\\ &= \Delta E_{\text{DLM-FTM}}(T) - T\int_T^{\infty} \frac{c_v}{T'} dT'.\end{aligned} \tag{6.8}$$

We cannot carry out simulations to infinite temperature, therefore we assume that at the highest temperature employed, the entropy difference from the DLM state is zero. The free energy difference calculated with these two methods is shown in Fig. 6.7, only for temperatures above the transition temperature. We observe a 5% discrepancy between the value calculated with mTPT and with Eq. 6.8 from T_C up to temperatures of $\approx 3T_C$, and above this temperature the discrepancy decreases. We employ this method for the actual Fe system using as reference state the FTM state, which means that H_0 is the DFT energy of the ASD-AIMD snapshots, and H_1 is the DFT energy of the DLM state, which is represented with the MSM approach. In particular, to have better DLM energies, we carry out 5 calculations on each snapshots from ASD-AIMD, each with a different MSM magnetic configuration. The

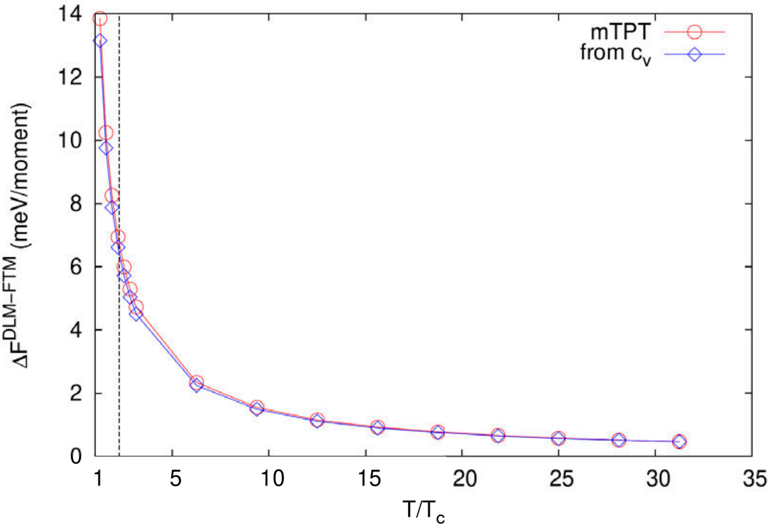

Figure 6.7: Free energy difference between DLM and FTM states from mTPT and and from Eq. 6.8 as a function of reduced temperature T/T_C with MC simulations. The dashed vertical line indicates a temperature corresponding to 1800 K in the Fe system, taking as reference the calculated T_C in this system.

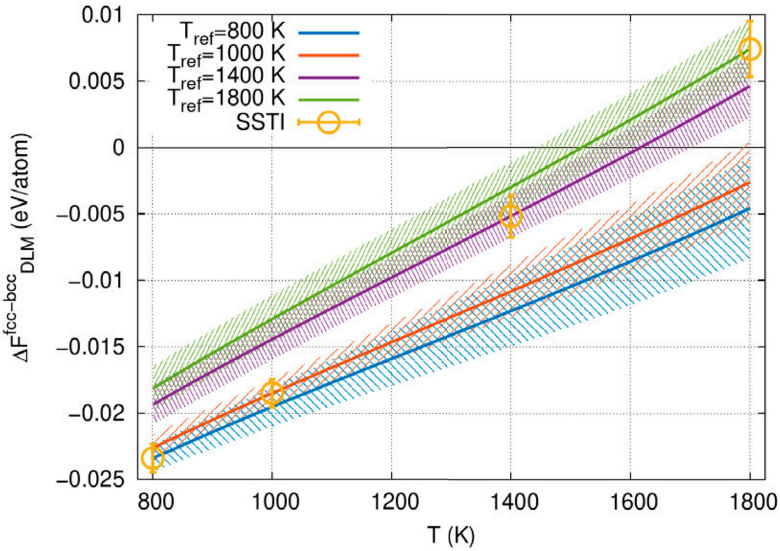

Figure 6.8: Free energy difference between fcc and bcc Fe as a function of temperature in the DLM state.

MSM magnetic configurations are generated with MC simulations employing $J = 0$ for every shell, and then picking the configurations with spin-spin correlation functions as small as possible for the first two coordination shells. The mTPT free energy difference is calculated at temperatures of 800, 1000, 1400 and 1800 K.

Knowing how to connect the FTM and DLM states, we perform DLM-AIMD simulations with five different structures to calculate the fcc-bcc free energy difference with SSTI: bcc, fcc, and three intermediate structures along the Bain path generated by linear interpolation of the matrices in Eq. 3.23. We perform the SSTI in the DLM state at temperatures of 800, 1000, 1400 and 1800 K, and we observe a linear increase of the free energy difference as a function of temperature (see Fig. 6.8). Since we have total energies for bcc and fcc Fe, and we have several reference free energy differences, we calculate $\Delta F^{\text{fcc-bcc}}_{\text{DLM}}[V_{\text{eq}}(T_0), T]$ also with the TTI method, Eq. 3.18. It is interesting to notice here that the two different TI methods do not agree on the temperature dependence of the free energy difference.

Finally, all the results obtained so far can be put together. The Gibbs free energy is now obtained as:

$$\begin{aligned}\Delta G^{\text{fcc-bcc}}(P=0,T) = {} & \Delta F^{\text{fcc-bcc}}_{\text{DLM}}[V_{\text{eq}}(T_0), T] \\ & - \Delta F^{\text{fcc}}_{\text{DLM-FTM}}[V_{\text{eq}}(T_0), T] + \Delta F^{\text{fcc}}[V_{\text{eq}}(T), V_{\text{eq}}(T_0)] \\ & + \Delta F^{\text{bcc}}_{\text{DLM-FTM}}[V_{\text{eq}}(T_0), T] - \Delta F^{\text{bcc}}[V_{\text{eq}}(T), V_{\text{eq}}(T_0)].\end{aligned} \tag{6.9}$$

Also here there are two ways to obtain $\Delta G^{\text{fcc-bcc}}(P=0,T)$: using all the values from SSTI and the mTPT results at each of these temperature, or using a single value from SSTI and the corresponding mTPT value, and then integrate with TTI in temperature. In Fig. 6.9, the results of both approaches are shown, and for the TTI curves we use as the reference free energy difference in the DLM state $\Delta F^{\text{fcc-bcc}}_{\text{DLM}}[V_{\text{eq}}(T_0), T]$ the values at $T = 1800$ K from each of the curves from Fig. 6.8. Of course, the curves do not agree with each other, nonetheless two of them predict the double transition $\alpha \to \gamma \to \delta$, whereas the other two do not predict any transition in the temperature range shown here, although it can be argued that there is a bcc to fcc transition at a temperature lower than 800 K. The other big difference is with the results where only SSTI and mTPT are employed, which predict bcc Fe to be always stable, although very close to transition. At high temperatures, this latest approach agrees with the two highest curves from the TTI, but going down in temperature, the discrepancy becomes very large. From the initial tests on mTPT, we know that at lower temperatures the method will have larger absolute errors (not accounted for in the error bars in the plot), therefore one cannot trust completely the lowest two points in temperature.

Nonetheless, the results of the SSTI+mTPT approach are surprisingly close to both experimental and theoretical results from literature, shown in Fig. 6.10. The blue curve in this figure is from a spin-lattice dynamics study

[139], whereas the green experimental curve, obtained with the CALPHAD method, was extracted from Ref. [140]. At T=800 K, there is a considerable difference between our results and the results from literature. We know that at this temperature mTPT is less accurate, nonetheless the small exchange interactions employed for bcc Fe should take down this value, but this does not happen.

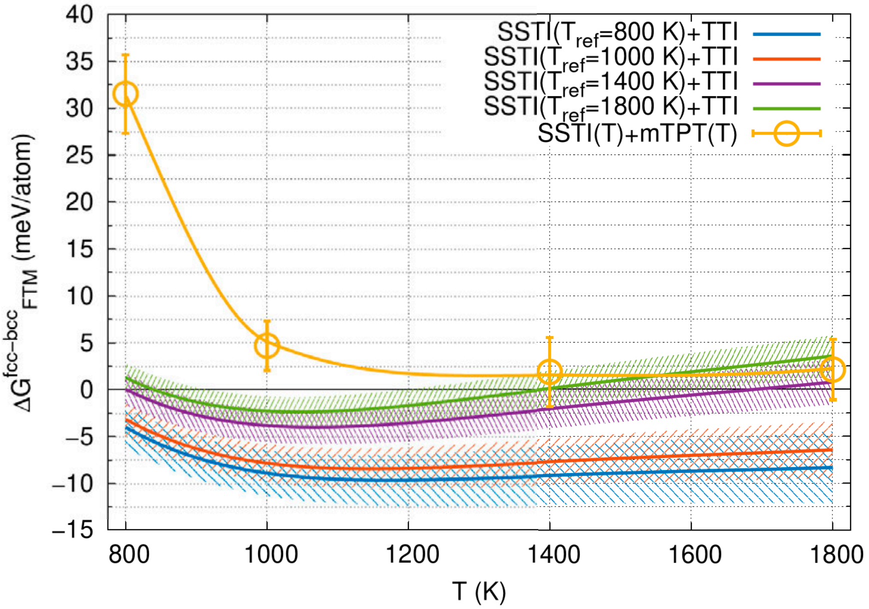

Figure 6.9: Gibbs free energy difference between fcc and bcc Fe as a function of temperature in the FTM state.

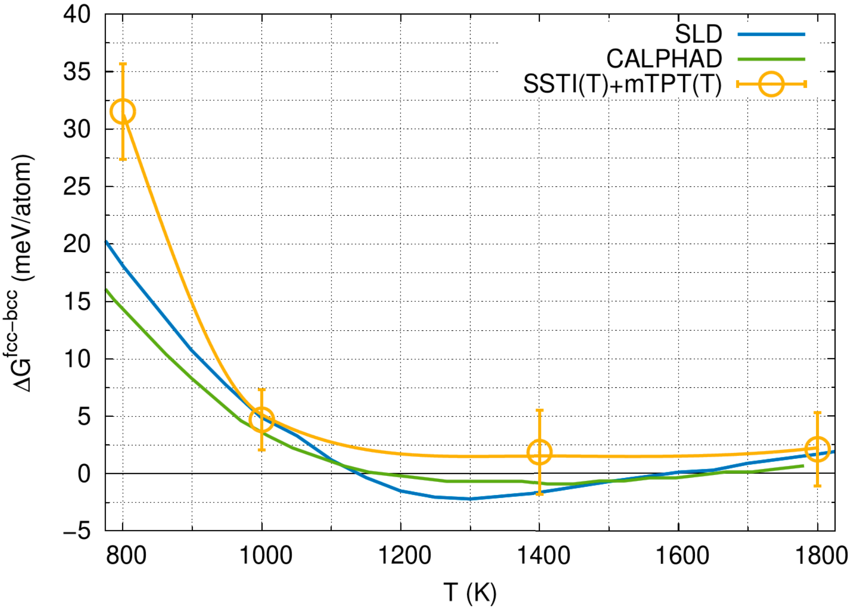

Figure 6.10: Gibbs free energy difference between fcc and bcc Fe as a function of temperature in the FTM state from SSTI+mTPT and from literature.

7 | Conclusions and outlook

Accurate modeling of magnetic materials in their high-temperature paramagnetic phase with first principles methods is a challenging task. With this thesis, I hope to have contributed to fill some gaps to achieve a more realistic description of these systems with density functional theory calculations and statistical mechanics methods. The most challenging part of the modeling is related to the coupling between different degrees of freedom.

The coupling between magnetic and structural degrees of freedom is the first topic in this thesis, and to improve the description of this interplay I have developed a method which enables the structural relaxation of the atomic positions in the paramagnetic state, described here with the disordered local moment approach. This method was tested on point defects in paramagnetic bcc Fe and on $Fe_{1-x}Cr_x$ random alloys, showing a small but non-negligible effect on the energetics of these systems. Nonetheless, this method allows a consistent calculation of materials properties in the paramagnetic state, therefore it should be used whenever one is dealing with magnetic materials in this state. This relaxation method was then employed in different cases, such as the $1/2\langle 111\rangle$ screw dislocation in paramagnetic bcc Fe, extrinsic and intrinsic defects in CrN for thermoelectric applications, and a newly synthesized compound, Fe_3CO_7, with interesting stoichiometry and possible implications for the chemistry of the Earth's mantle.

The other main topic of the thesis is the coupling between magnetism and vibrations. The investigation of this interplay requires employment of advanced statistical mechanics method, thermodynamic models, and expensive computer simulations. Initially, I have focused on the effect of vibrations on the longitudinal degree of freedom of magnetic fluctuations, known as longitudinal spin fluctuations, which affect the size of the moments in magnetic metals at finite temperatures. The energy landscapes that govern this degree of freedom were calculated in bcc Fe at the Curie temperature with vibrations, and a strong effect of the thermal disorder was observed on these landscapes. Inclusion of the longitudinal spin fluctuations in calculations of liquid and solid bcc Fe at temperatures and pressures expected in the Earth's core gives rise to local moments also at these incredible pressures, unexpectedly. In addition, the results of this work served as a basis to develop a machine learning algorithm that can predict the longitudinal spin fluctuations energy landscapes taking as input the local environment of the atom. The machine learning algorithm was then employed in combination with coupled atomistic spin dynamics-*ab initio* molecular dynamics simulations to include the effect of longitudinal spin fluctuations on the size of the moments at each timestep. Finally, the difficult task of calculating the Gibbs free energy difference between fcc and bcc Fe as a function of temperature was described. This investigation required the employment of different dynamical simulation and statistical mechanics methods. A path to the calculation of the free energy difference goes through the employment of stress-strain thermodynamic integration in the disordered local moment state and then connection to finite temperature magnetism with a magnetic version of the thermodynamic perturbation theory method. Some issues remain in this method, especially regarding the discrepancies between the free energy differences calculated with different methods; nonetheless, the thermodynamic path defined in this work is worth of consideration when only free energy differences are needed.

The investigation of both these different types of coupling needs further technical and theoretical developments. The disordered local moment approach models an ideal paramagnetic state, which is in principle the real state of a magnetic material only at infinite temperatures. In addition, lattice vibrations are always present, therefore accurate investigation of defects should pass by dynamic simulations as well, with a full coupling of magnetic, structural and vibrational degrees of freedom. This in principle could be presently done with atomistic spin dynamics-*ab initio* molecular dynamics simulations, although at present this would require calculation of exchange interactions also with the defect, which is possible but not trivial. A better method would be to perform also *ab initio* spin dynamics, which does not require any assumption on the evolution of the magnetic degrees of freedom. This method was tested many years ago, but never employed in realistic situations. This method would of course also help in the stress-strain thermodynamic integration method, since with it one could bypass the simulations in the disordered local moment state, and therefore carry out less simulations and with less uncertainties. It is probably now time to implement this *ab initio* spin dynamics method together with *ab initio* molecular dynamics in efficient codes so that coupled simulations can be carried out fully from first principles. On the point of view of coupled simulations, another path to go through would be the employment of machine learning methods to simulate both magnetic and atomic degrees of freedom. These methods would be less accurate than first principles calculations, however they would enable the study of much larger systems and for much longer time, which could allow to calculate properties of extended defects or nucleation process, as an example, including the best possible interatomic potential with almost DFT accuracy. From the point of view of fundamental research, I find always unsatisfactory discussions on longitudinal spin fluctuations and the typical thermodynamic treatment of this degree of freedom: there seems to be a lack of basic understanding of the timescales on which this degree of freedom evolves, and therefore high-level theories should be employed to try to pinpoint more accurately this effect, so that the thermodynamic models can be benchmarked on these results. Finally, I can see that the methods presented in this thesis need to be employed on more systems with relevant technological applications. An example here was given by the investigation of CrN, however employment of these methods in the investigation of magnetocaloric materials, for example, could help in the design of new materials with tailored properties for real world applications that also contribute to lower the impact of technologies on the environment.

Bibliography

[1] J. D. Martin. *When condensed-matter physics became king*, **Physics Today 72**, 30–37 (2019).

[2] *Boosting materials modelling*, **Nature Materials 15**, 365–365 (2016).

[3] J. J. de Pablo, N. E. Jackson, M. A. Webb, L.-Q. Chen, J. E. Moore, D. Morgan, R. Jacobs, T. Pollock, D. G. Schlom, E. S. Toberer, J. Analytis, I. Dabo, D. M. DeLongchamp, G. A. Fiete, G. M. Grason, G. Hautier, Y. Mo, K. Rajan, E. J. Reed, E. Rodriguez, V. Stevanovic, J. Suntivich, K. Thornton, and J.-C. Zhao. *New frontiers for the materials genome initiative*, **npj Computational Materials 5**, 41 (2019).

[4] R. M. Martin. *Electronic Structure: Basic Theory and Practical Methods*, Cambridge University Press, (2004).

[5] P. Hohenberg and W. Kohn. *Inhomogeneous Electron Gas*, **Phys. Rev. 136**, B864–B871 (1964).

[6] W. Kohn and L. J. Sham. *Self-Consistent Equations Including Exchange and Correlation Effects*, **Phys. Rev. 140**, A1133–A1138 (1965).

[7] D. Frenkel and B. Smit. *Understanding molecular simulation. from algorithms to applications.* Computational science series: 1. Academic Press, (2002).

[8] N. W. Ashcroft and N. D. Mermin. *Solid state physics.* Saunders College, (1976).

[9] J. B. Carlson. *Lodestone Compass: Chinese or Olmec Primacy?*, **Science 189**, 753–760 (1975).

[10] S. Blundell. *Magnetism in condensed matter.* Oxford master series in condensed matter physics. Oxford Univ. Press, (2001).

[11] O. Barrera, D. Bombac, Y. Chen, T. D. Daff, E. Galindo-Nava, P. Gong, D. Haley, R. Horton, I. Katzarov, J. R. Kermode, C. Liverani, M. Stopher, and F. Sweeney. *Understanding and mitigating hydrogen embrittlement of steels: a review of experimental, modelling and design progress from atomistic to continuum*, **Journal of Materials Science 53**, 6251–6290 (2018).

[12] Y. Wu, Y. Wang, X. Qin, X. Rong, and J. Du. *A programmable two-qubit solid-state quantum processor under ambient conditions*, **npj Quantum Information 5**, 9 (2019).

[13] J. Davidsson. *Color Centers in Semiconductors for Quantum Applications : A High-Throughput Search of Point Defects in SiC*, PhD thesis. Linköping University, Faculty of Science & Engineering, (2021), 72.

[14] P. A. M. Dirac. *Quantum mechanics of many electron systems*, **123**, 714–733 (1929).

[15] K. T. Williams, Y. Yao, J. Li, L. Chen, H. Shi, M. Motta, C. Niu, U. Ray, S. Guo, R. J. Anderson, J. Li, L. N. Tran, C.-N. Yeh, B. Mussard, S. Sharma, F. Bruneval, M. van Schilfgaarde, G. H. Booth, G. K.-L. Chan, S. Zhang, E. Gull, D. Zgid, A. Millis, C. J. Umrigar, and L. K. Wagner. *Direct Comparison of Many-Body Methods for Realistic Electronic Hamiltonians*, **Phys. Rev. X 10**, 011041 (2020).

[16] J. J. Eriksen. *The Shape of Full Configuration Interaction to Come*, **The Journal of Physical Chemistry Letters 12**, 418–432 (2021).

[17] T. E. Markland and M. Ceriotti. *Nuclear quantum effects enter the mainstream*, **Nature Reviews Chemistry 2**, 0109 (2018).

[18] I. Poltavsky, R. A. DiStasio, and A. Tkatchenko. *Perturbed path integrals in imaginary time: Efficiently modeling nuclear quantum effects in molecules and materials*, **The Journal of Chemical Physics 148**, 102325 (2018).

[19] L. H. Thomas. *The calculation of atomic fields*, **Mathematical Proceedings of the Cambridge Philosophical Society 23**, 542–548 (1927).

[20] E. Fermi. *Un Metodo Statistico per la Determinazione di alcune Priopriet̀a dell'Atomo*, **Rendiconti dell'Accademia Nazionale dei Lincei 6**, 602–607 (1927).

[21] P. E. Blöchl. *Projector augmented-wave method*, **Phys. Rev. B 50**, 17953–17979 (1994).

[22] P.-W. Ma and S. L. Dudarev. *Constrained density functional for noncollinear magnetism*, **Phys. Rev. B 91**, 054420 (2015).

[23] D. M. Ceperley and B. J. Alder. *Ground State of the Electron Gas by a Stochastic Method*, **Phys. Rev. Lett. 45**, 566–569 (1980).

[24] J. P. Perdew, K. Burke, and M. Ernzerhof. *Generalized Gradient Approximation Made Simple*, **Phys. Rev. Lett. 77**, 3865–3868 (1996).

[25] J. A. Pople. *Quantum Chemical Models (Nobel Lecture)*, **Angewandte Chemie International Edition 38**, 1894–1902 (1999).

[26] J. P. Perdew and K. Schmidt. *Jacob's ladder of density functional approximations for the exchange-correlation energy*, **AIP Conference Proceedings 577**, 1–20 (2001).

[27] F. Dorner, Z. Sukurma, C. Dellago, and G. Kresse. *Melting Si: Beyond Density Functional Theory*, **Phys. Rev. Lett. 121**, 195701 (2018).

[28] V. I. Anisimov, J. Zaanen, and O. K. Andersen. *Band theory and Mott insulators: Hubbard U instead of Stoner I*, **Phys. Rev. B 44**, 943–954 (1991).

[29] A. I. Liechtenstein, V. I. Anisimov, and J. Zaanen. *Density-functional theory and strong interactions: Orbital ordering in Mott-Hubbard insulators*, **Phys. Rev. B 52**, R5467–R5470 (1995).

[30] S. L. Dudarev, G. A. Botton, S. Y. Savrasov, C. J. Humphreys, and A. P. Sutton. *Electron-energy-loss spectra and the structural stability of nickel oxide: An LSDA+U study*, **Phys. Rev. B 57**, 1505–1509 (1998).

[31] M. Cococcioni and S. de Gironcoli. *Linear response approach to the calculation of the effective interaction parameters in the* $\mathrm{LDA}+\mathrm{U}$ *method*, **Phys. Rev. B 71**, 035105 (2005).

[32] J. Sun, A. Ruzsinszky, and J. P. Perdew. *Strongly Constrained and Appropriately Normed Semilocal Density Functional*, **Phys. Rev. Lett. 115**, 036402 (2015).

[33] Y. Zhang, D. A. Kitchaev, J. Yang, T. Chen, S. T. Dacek, R. A. Sarmiento-Pérez, M. A. L. Marques, H. Peng, G. Ceder, J. P. Perdew, and J. Sun. *Efficient first-principles prediction of solid stability: Towards chemical accuracy*, **npj Computational Materials 4**, 9 (2018).

[34] A. H. Romero and M. J. Verstraete. *From one to three, exploring the rungs of Jacob's ladder in magnetic alloys*, **The European Physical Journal B 91**, 193 (2018).

[35] Y. Fu and D. J. Singh. *Applicability of the Strongly Constrained and Appropriately Normed Density Functional to Transition-Metal Magnetism*, **Phys. Rev. Lett. 121**, 207201 (2018).

[36] N. D. Mermin. *Thermal Properties of the Inhomogeneous Electron Gas*, **Phys. Rev. 137**, A1441–A1443 (1965).

[37] J. Behler. *Perspective: Machine learning potentials for atomistic simulations*, **The Journal of Chemical Physics 145**, 170901 (2016).

[38] C. Dellago and P. G. Bolhuis. *Transition Path Sampling and Other Advanced Simulation Techniques for Rare Events*, In: **Advanced Computer Simulation Approaches for Soft Matter Sciences III**. Ed. by C. Holm and K. Kremer. Berlin, Heidelberg: Springer Berlin Heidelberg, (2009), 167–233.

[39] P. C. Aeberhard, S. R. Williams, D. J. Evans, K. Refson, and W. I. F. David. *Ab initio Nonequilibrium Molecular Dynamics in the Solid Superionic Conductor* $\mathrm{LiBH_4}$, **Phys. Rev. Lett. 108**, 095901 (2012).

[40] D. G. Sangiovanni, O. Hellman, B. Alling, and I. A. Abrikosov. *Efficient and accurate determination of lattice-vacancy diffusion coefficients via non equilibrium ab initio molecular dynamics*, **Phys. Rev. B 93**, 094305 (2016).

[41] D. P. Landau and K. Binder. *A Guide to Monte Carlo Simulations in Statistical Physics*, 4th ed. Cambridge University Press, (2014).

[42] O. Hellman, I. A. Abrikosov, and S. I. Simak. *Lattice dynamics of anharmonic solids from first principles*, **Phys. Rev. B 84**, 180301 (2011); O. Hellman and I. A. Abrikosov. *Temperature-dependent effective third-order interatomic force constants from first principles*, **Phys. Rev. B 88**, 144301 (2013); O. Hellman, P. Steneteg, I. A. Abrikosov, and S. I. Simak. *Temperature dependent effective potential method for accurate free energy calculations of solids*, **Phys. Rev. B 87**, 104111 (2013).

[43] I. Errea, M. Calandra, and F. Mauri. *First-Principles Theory of Anharmonicity and the Inverse Isotope Effect in Superconducting Palladium-Hydride Compounds*, **Phys. Rev. Lett. 111**, 177002 (2013); I. Errea, M. Calandra, and F. Mauri. *Anharmonic free energies and phonon dispersions from the stochastic self-consistent harmonic approximation: Application to platinum and palladium hydrides*, **Phys. Rev. B 89**, 064302 (2014); R. Bianco, I. Errea, L. Paulatto, M. Calandra, and F. Mauri. *Second-order structural phase transitions, free energy curvature, and temperature-dependent anharmonic phonons in the self-consistent harmonic approximation: Theory and stochastic implementation*, **Phys. Rev. B 96**, 014111 (2017); L. Monacelli, I. Errea, M. Calandra, and F. Mauri. *Pressure and stress tensor of complex anharmonic crystals within the stochastic self-consistent harmonic approximation*, **Phys. Rev. B 98**, 024106 (2018).

[44] B. Cheng and M. Ceriotti. *Computing the absolute Gibbs free energy in atomistic simulations: Applications to defects in solids*, **Phys. Rev. B 97**, 054102 (2018).

[45] B. Grabowski, L. Ismer, T. Hickel, and J. Neugebauer. *Ab initio up to the melting point: Anharmonicity and vacancies in aluminum*, **Phys. Rev. B 79**, 134106 (2009).

[46] A. Glensk, B. Grabowski, T. Hickel, and J. Neugebauer. *Breakdown of the Arrhenius Law in Describing Vacancy Formation Energies: The Importance of Local Anharmonicity Revealed by Ab initio Thermodynamics*, **Phys. Rev. X 4**, 011018 (2014).

[47] Y. Gong, B. Grabowski, A. Glensk, F. Körmann, J. Neugebauer, and R. C. Reed. *Temperature dependence of the Gibbs energy of vacancy formation of fcc Ni*, **Phys. Rev. B 97**, 214106 (2018).

[48] D. Wallace. *Thermodynamics of Crystals*, Wiley & Sons, (1972).

[49] J. Klarbring and S. I. Simak. *Phase Stability of Dynamically Disordered Solids from First Principles*, **Phys. Rev. Lett. 121**, 225702 (2018).

[50] W. Metzner and D. Vollhardt. *Correlated Lattice Fermions in $d = \infty$ Dimensions*, **Phys. Rev. Lett. 62**, 324–327 (1989).

[51] A. Georges and G. Kotliar. *Hubbard model in infinite dimensions*, **Phys. Rev. B 45**, 6479–6483 (1992).

[52] A. I. Poteryaev, A. I. Lichtenstein, and G. Kotliar. *Nonlocal Coulomb Interactions and Metal-Insulator Transition in* $\mathrm{Ti_2O_3}$*: A Cluster* LDA + DMFT *Approach*, **Phys. Rev. Lett. 93**, 086401 (2004).

[53] I. Abrikosov, A. Ponomareva, P. Steneteg, S. Barannikova, and B. Alling. *Recent progress in simulations of the paramagnetic state of magnetic materials*, **Current Opinion in Solid State and Materials Science 20**, 85–106 (2016).

[54] P. Hansmann, N. Parragh, A. Toschi, G. Sangiovanni, and K. Held. *Importance ofd–pCoulomb interaction for high TCcuprates and other oxides*, **New Journal of Physics 16**, 033009 (2014).

[55] I. Leonov, A. I. Poteryaev, Y. N. Gornostyrev, A. I. Lichtenstein, M. I. Katsnelson, V. I. Anisimov, and D. Vollhardt. *Electronic correlations determine the phase stability of iron up to the melting temperature*, **Scientific Reports 4**, 5585 EP - (2014).

[56] P. Delange, T. Ayral, S. I. Simak, M. Ferrero, O. Parcollet, S. Biermann, and L. Pourovskii. *Large effects of subtle electronic correlations on the energetics of vacancies in α-Fe*, **Phys. Rev. B 94**, 100102 (2016).

[57] K. Haule and G. L. Pascut. *Forces for structural optimizations in correlated materials within a DFT+embedded DMFT functional approach*, **Phys. Rev. B 94**, 195146 (2016).

[58] K. Haule and G. L. Pascut. *Forces for structural optimizations in correlated materials within a DFT+embedded DMFT functional approach*, **Phys. Rev. B 94**, 195146 (2016).

[59] L. Bergqvist and A. Bergman. *Realistic finite temperature simulations of magnetic systems using quantum statistics*, **Phys. Rev. Materials 2**, 013802 (2018).

[60] A. Liechtenstein, M. Katsnelson, V. Antropov, and V. Gubanov. *Local spin density functional approach to the theory of exchange interactions in ferromagnetic metals and alloys*, **Journal of Magnetism and Magnetic Materials 67**, 65–74 (1987).

[61] A. V. Ruban, S. Shallcross, S. I. Simak, and H. L. Skriver. *Atomic and magnetic configurational energetics by the generalized perturbation method*, **Phys. Rev. B 70**, 125115 (2004).

[62] A. Lindmaa, R. Lizárraga, E. Holmström, I. A. Abrikosov, and B. Alling. *Exchange interactions in paramagnetic amorphous and disordered crystalline* CrN*-based systems*, **Phys. Rev. B 88**, 054414 (2013).

[63] J. Yin, M. Eisenbach, D. M. Nicholson, and A. Rusanu. *Effect of lattice vibrations on magnetic phase transition in bcc iron*, **Phys. Rev. B 86**, 214423 (2012).

[64] A. V. Ruban and O. E. Peil. *Impact of thermal atomic displacements on the Curie temperature of* 3*d transition metals*, **Phys. Rev. B 97**, 174426 (2018).

[65] B. Skubic, J. Hellsvik, L. Nordström, and O. Eriksson. *A method for atomistic spin dynamics simulations: implementation and examples*, **Journal of Physics: Condensed Matter 20**, 315203 (2008).

[66] T. Archer, C. D. Pemmaraju, S. Sanvito, C. Franchini, J. He, A. Filippetti, P. Delugas, D. Puggioni, V. Fiorentini, R. Tiwari, and P. Majumdar. *Exchange interactions and magnetic phases of transition metal oxides: Benchmarking advanced ab initio methods*, **Phys. Rev. B 84**, 115114 (2011).

[67] G. Fischer, M. Däne, A. Ernst, P. Bruno, M. Lüders, Z. Szotek, W. Temmerman, and W. Hergert. *Exchange coupling in transition metal monoxides: Electronic structure calculations*, **Phys. Rev. B 80**, 014408 (2009).

[68] P. Gopal, R. D. Gennaro, M. S. dos Santos Gusmao, R. A. R. A. Orabi, H. Wang, S. Curtarolo, M. Fornari, and M. B. Nardelli. *Improved electronic structure and magnetic exchange interactions in transition metal oxides*, **Journal of Physics: Condensed Matter 29**, 444003 (2017).

[69] N. M. Rosengaard and B. Johansson. *Finite-temperature study of itinerant ferromagnetism in Fe, Co, and Ni*, **Phys. Rev. B 55**, 14975–14986 (1997).

[70] A. V. Ruban, S. Khmelevskyi, P. Mohn, and B. Johansson. *Temperature-induced longitudinal spin fluctuations in Fe and Ni*, **Phys. Rev. B 75**, 054402 (2007).

[71] L. M. Sandratskii. *Thermal magnetic properties of the Ni sublattice in half-metallic NiMnSb: A theoretical study based on first-principles calculations*, **Phys. Rev. B 78**, 094425 (2008).

[72] A. V. Ruban, A. B. Belonoshko, and N. V. Skorodumova. *Impact of magnetism on Fe under Earth's core conditions*, **Phys. Rev. B 87**, 014405 (2013).

[73] Z. Dong, W. Li, D. Chen, S. Schönecker, M. Long, and L. Vitos. *Longitudinal spin fluctuation contribution to thermal lattice expansion of paramagnetic Fe*, **Phys. Rev. B 95**, 054426 (2017).

[74] S. Khmelevskyi. *Longitudinal integration measure in classical spin space and its application to first-principle based simulations of ferromagnetic metals*, **Journal of Magnetism and Magnetic Materials 461**, 14–18 (2018).

[75] A. L. Wysocki, J. K. Glasbrenner, and K. D. Belashchenko. *Thermodynamics of itinerant magnets in a classical spin-fluctuation model*, **Phys. Rev. B 78**, 184419 (2008).

[76] F. Pan, J. Chico, A. Delin, A. Bergman, and L. Bergqvist. *Extended spin model in atomistic simulations of alloys*, **Phys. Rev. B 95**, 184432 (2017).

[77] J. Hubbard. *The magnetism of iron*, **Phys. Rev. B 19**, 2626–2636 (1979).

[78] J. Hubbard. *Magnetism of iron. II*, **Phys. Rev. B 20**, 4584–4595 (1979).

[79] J. Hubbard. *Magnetism of nickel*, **Phys. Rev. B 23**, 5974–5977 (1981).

[80] H. Hasegawa. *Single-Site Functional-Integral Approach to Itinerant-Electron Ferromagnetism*, **Journal of the Physical Society of Japan 46**, 1504–1514 (1979).

[81] H. Hasegawa. *Single-Siet Spin Fluctuation Theory of Itinerant-Electron Systems with Narrow Bands*, **Journal of the Physical Society of Japan 49**, 178–188 (1980).

[82] B. L. Gyorffy, A. J. Pindor, J. Staunton, G. M. Stocks, and H. Winter. *A first-principles theory of ferromagnetic phase transitions in metals*, **Journal of Physics F: Metal Physics 15**, 1337 (1985).

[83] B. Alling, T. Marten, and I. A. Abrikosov. *Effect of magnetic disorder and strong electron correlations on the thermodynamics of CrN*, **Phys. Rev. B 82**, 184430 (2010).

[84] P. Olsson, I. Abrikosov, L. Vitos, and J. Wallenius. *Ab initio formation energies of Fe–Cr alloys*, **Journal of Nuclear Materials 321**, 84–90 (2003).

[85] F. Körmann, A. Dick, B. Grabowski, T. Hickel, and J. Neugebauer. *Atomic forces at finite magnetic temperatures: Phonons in paramagnetic iron*, **Phys. Rev. B 85**, 125104 (2012).

[86] B. Alling, L. Hultberg, L. Hultman, and I. A. Abrikosov. *Strong electron correlations stabilize paramagnetic cubic* $Cr_{1-x}Al_xN$ *solid solutions*, **Applied Physics Letters 102**, 031910 (2013).

[87] P. Steneteg, B. Alling, and I. A. Abrikosov. *Equation of state of paramagnetic CrN from ab initio molecular dynamics*, **Phys. Rev. B 85**, 144404 (2012).

[88] N. Shulumba, B. Alling, O. Hellman, E. Mozafari, P. Steneteg, M. Odén, and I. A. Abrikosov. *Vibrational free energy and phase stability of paramagnetic and antiferromagnetic CrN from ab initio molecular dynamics*, **Phys. Rev. B 89**, 174108 (2014).

[89] E. Mozafari, B. Alling, P. Steneteg, and I. A. Abrikosov. *Role of N defects in paramagnetic CrN at finite temperatures from first principles*, **Phys. Rev. B 91**, 094101 (2015).

[90] B. Alling, F. Körmann, B. Grabowski, A. Glensk, I. A. Abrikosov, and J. Neugebauer. *Strong impact of lattice vibrations on electronic and magnetic properties of paramagnetic Fe revealed by disordered local moments molecular dynamics*, **Phys. Rev. B 93**, 224411 (2016).

[91] I. Stockem, A. Bergman, A. Glensk, T. Hickel, F. Körmann, B. Grabowski, J. Neugebauer, and B. Alling. *Anomalous Phonon Lifetime Shortening in Paramagnetic CrN Caused by Spin-Lattice Coupling: A Combined Spin and Ab Initio Molecular Dynamics Study*, **Phys. Rev. Lett. 121**, 125902 (2018).

[92] G. R. Odette and G. E. Lucas. *Embrittlement of nuclear reactor pressure vessels*, **JOM 53**, 18–22 (2001).

[93] T. Diaz de la Rubia and M. W. Guinan. *New mechanism of defect production in metals: A molecular-dynamics study of interstitial-dislocation-loop formation in high-energy displacement cascades*, **Phys. Rev. Lett. 66**, 2766–2769 (1991).

[94] P. M. Derlet, D. Nguyen-Manh, and S. L. Dudarev. *Multiscale modeling of crowdion and vacancy defects in body-centered-cubic transition metals*, **Phys. Rev. B 76**, 054107 (2007).

[95] D. E. Jiang and E. A. Carter. *Diffusion of interstitial hydrogen into and through bcc Fe from first principles*, **Phys. Rev. B 70**, 064102 (2004).

[96] A. F. Bialon, T. Hammerschmidt, and R. Drautz. *Ab initio study of boron in α-iron: Migration barriers and interaction with point defects*, **Phys. Rev. B 87**, 104109 (2013).

[97] W. Kohn. *Density Functional and Density Matrix Method Scaling Linearly with the Number of Atoms*, **Phys. Rev. Lett. 76**, 3168–3171 (1996).

[98] S. B. Zhang and J. E. Northrup. *Chemical potential dependence of defect formation energies in GaAs: Application to Ga self-diffusion*, **Phys. Rev. Lett. 67**, 2339–2342 (1991).

[99] C. G. Van de Walle, D. B. Laks, G. F. Neumark, and S. T. Pantelides. *First-principles calculations of solubilities and doping limits: Li, Na, and N in ZnSe*, **Phys. Rev. B 47**, 9425–9434 (1993).

[100] C. Varvenne, F. Bruneval, M.-C. Marinica, and E. Clouet. *Point defect modeling in materials: Coupling ab initio and elasticity approaches*, **Phys. Rev. B 88**, 134102 (2013).

[101] C. Freysoldt, J. Neugebauer, and C. G. Van de Walle. *Fully Ab Initio Finite-Size Corrections for Charged-Defect Supercell Calculations*, **Phys. Rev. Lett. 102**, 016402 (2009).

[102] C. Freysoldt, J. Neugebauer, and C. G. Van de Walle. *Electrostatic interactions between charged defects in supercells*, **Physica Status Solidi (b) 248**, 1067–1076 (2011).

[103] D. E. Jiang and E. A. Carter. *Carbon dissolution and diffusion in ferrite and austenite from first principles*, **Phys. Rev. B 67**, 214103 (2003).

[104] D. Hull and D. J. Bacon. *Introduction to dislocations*, English. Fifth Edition. Oxford: Butterworth-Heinemann, (2011).

[105] D. Rodney, L. Ventelon, E. Clouet, L. Pizzagalli, and F. Willaime. *Ab initio modeling of dislocation core properties in metals and semiconductors*, **Acta Materialia 124**, 633–659 (2017).

[106] H. Jónson, G. Mills, and K. W. Jacobsen. *Nudged elastic band method for finding minimum energy paths of transitions*, In: **Classical and Quantum Dynamics in Condensed Phase Simulations**, 385–404.

[107] G. Henkelman, B. P. Uberuaga, and H. Jónsson. *A climbing image nudged elastic band method for finding saddle points and minimum energy paths*, **The Journal of Chemical Physics 113**, 9901–9904 (2000).

[108] W. E, W. Ren, and E. Vanden-Eijnden. *String method for the study of rare events*, **Phys. Rev. B 66**, 052301 (2002).

[109] W. E, W. Ren, and E. Vanden-Eijnden. *Finite Temperature String Method for the Study of Rare Events*, **The Journal of Physical Chemistry B 109**, 6688–6693 (2005).

[110] H. Eyring. *The Activated Complex in Chemical Reactions*, **The Journal of Chemical Physics 3**, 107–115 (1935).

[111] G. H. Vineyard. *Frequency factors and isotope effects in solid state rate processes*, **Journal of Physics and Chemistry of Solids 3**, 121–127 (1957).

[112] A. B. Belonoshko, T. Lukinov, J. Fu, J. Zhao, S. Davis, and S. I. Simak. *Stabilization of body-centred cubic iron under inner-core conditions*, **Nature Geoscience 10**, 312–316 (2017).

[113] E. Fransson and P. Erhart. *Defects from phonons: Atomic transport by concerted motion in simple crystalline metals*, **Acta Materialia 196**, 770–775 (2020).

[114] Y. Wang, J. Wang, A. Hermann, C. Liu, H. Gao, E. Tosatti, H.-T. Wang, D. Xing, and J. Sun. *Electronically Driven 1D Cooperative Diffusion in a Simple Cubic Crystal*, **Phys. Rev. X 11**, 011006 (2021).

[115] B. L. Gyorffy. *Coherent-Potential Approximation for a Nonoverlapping-Muffin-Tin-Potential Model of Random Substitutional Alloys*, **Phys. Rev. B 5**, 2382–2384 (1972).

[116] A. Zunger, S.-H. Wei, L. G. Ferreira, and J. E. Bernard. *Special quasirandom structures*, **Phys. Rev. Lett. 65**, 353–356 (1990).

[117] A. V. Ruban and I. A. Abrikosov. *Configurational thermodynamics of alloys from first principles: effective cluster interactions*, **Reports on Progress in Physics 71**, 046501 (2008).

[118] J. Sanchez, F. Ducastelle, and D. Gratias. *Generalized cluster description of multicomponent systems*, **Physica A: Statistical Mechanics and its Applications 128**, 334–350 (1984).

[119] F. Giustino. *Electron-phonon interactions from first principles*, **Rev. Mod. Phys. 89**, 015003 (2017).

[120] N. Sandberg, Z. Chang, L. Messina, P. Olsson, and P. Korzhavyi. *Modeling of the magnetic free energy of self-diffusion in bcc Fe*, **Phys. Rev. B 92**, 184102 (2015).

[121] A. V. Ponomareva, Y. N. Gornostyrev, and I. A. Abrikosov. *Ab initio calculation of the solution enthalpies of substitutional and interstitial impurities in paramagnetic fcc Fe*, **Phys. Rev. B 90**, 014439 (2014).

[122] A. V. Ruban and V. I. Razumovskiy. *Spin-wave method for the total energy of paramagnetic state*, **Phys. Rev. B 85**, 174407 (2012).

[123] H. Ding, V. I. Razumovskiy, and M. Asta. *Self diffusion anomaly in ferromagnetic metals: A density-functional-theory investigation of magnetically ordered and disordered Fe and Co*, **Acta Materialia 70**, 130–136 (2014).

[124] O. Hegde, M. Grabowski, X. Zhang, O. Waseda, T. Hickel, C. Freysoldt, and J. Neugebauer. *Atomic relaxation around defects in magnetically disordered materials computed by atomic spin constraints within an efficient Lagrange formalism*, **Phys. Rev. B 102**, 144101 (2020).

[125] H.-E. Schaefer, K. Maier, M. Weller, D. Herlach, A. Seeger, and J. Diehl. *Vacancy formation in iron investigated by positron annihilation in thermal equilibrium*, **Scripta Metallurgica 11**, 803–809 (1977).

[126] S. M. Kim and W. J. L. Buyers. *Vacancy formation energy in iron by positron annihilation*, **Journal of Physics F: Metal Physics 8**, L103 (1978).

[127] H. Matter, J. Winter, and W. Triftshäuser. *Phase transformations and vacancy formation energies of transition metals by positron annihilation*, **Applied physics 20**, 135–140 (1979).

[128] L. De Schepper, D. Segers, L. Dorikens-Vanpraet, M. Dorikens, G. Knuyt, L. M. Stals, and P. Moser. *Positron annihilation on pure and carbon-doped α-iron in thermal equilibrium*, **Phys. Rev. B 27**, 5257–5269 (1983).

[129] H.-E. Schaefer. *Investigation of Thermal Equilibrium Vacancies in Metals by Positron Annihilation*, **Physica Status Solidi (a) 102**, 47–65 (1987).

[130] P. Olsson, I. A. Abrikosov, and J. Wallenius. *Electronic origin of the anomalous stability of Fe-rich bcc Fe-Cr alloys*, **Phys. Rev. B 73**, 104416 (2006).

[131] P. Eklund, S. Kerdsongpanya, and B. Alling. *Transition-metal-nitride-based thin films as novel energy harvesting materials*, **J. Mater. Chem. C 4**, 3905–3914 (2016).

[132] J. R. Sootsman, D. Y. Chung, and M. G. Kanatzidis. *New and Old Concepts in Thermoelectric Materials*, **Angewandte Chemie International Edition 48**, 8616–8639 (2009).

[133] C. X. Quintela, J. P. Podkaminer, M. N. Luckyanova, T. R. Paudel, E. L. Thies, D. A. Hillsberry, D. A. Tenne, E. Y. Tsymbal, G. Chen, C.-B. Eom, and F. Rivadulla. *Epitaxial CrN Thin Films with High Thermoelectric Figure of Merit*, **Advanced Materials 27**, 3032–3037 (2015).

[134] L. M. Corliss, N. Elliott, and J. M. Hastings. *Antiferromagnetic Structure of CrN*, **Phys. Rev. 117**, 929–935 (1960).

[135] Y. Zheng, T. J. Slade, L. Hu, X. Y. Tan, Y. Luo, Z.-Z. Luo, J. Xu, Q. Yan, and M. G. Kanatzidis. *Defect engineering in thermoelectric materials: what have we learned?*, **Chem. Soc. Rev.** - (2021).

[136] A. B. Belonoshko, R. Ahuja, and B. Johansson. *Stability of the body-centred-cubic phase of iron in the Earth's inner core*, **Nature 424**, 1032–1034 (2003).

[137] N. Dubrovinskaia, L. Dubrovinsky, N. A. Solopova, A. Abakumov, S. Turner, M. Hanfland, E. Bykova, M. Bykov, C. Prescher, V. B. Prakapenka, S. Petitgirard, I. Chuvashova, B. Gasharova, Y.-L. Mathis, P. Ershov, I. Snigireva, and A. Snigirev. *Terapascal static pressure generation with ultrahigh yield strength nanodiamond*, **Science Advances 2** (2016).

[138] E. Koemets, I. Leonov, M. Bykov, E. Bykova, S. Chariton, G. Aprilis, T. Fedotenko, S. Clément, J. Rouquette, J. Haines, V. Cerantola, K. Glazyrin, C. McCammon, V. B. Prakapenka, M. Hanfland, H.-P. Liermann, V. Svitlyk, R. Torchio, A. D. Rosa, T. Irifune, A. V. Ponomareva, I. A. Abrikosov, N. Dubrovinskaia, and L. Dubrovinsky. *Revealing the Complex Nature of Bonding in the Binary High-Pressure Compound* $\mathrm{FeO_2}$, **Phys. Rev. Lett. 126**, 106001 (2021).

[139] P.-W. Ma, S. L. Dudarev, and J. S. Wróbel. *Dynamic simulation of structural phase transitions in magnetic iron*, **Phys. Rev. B 96**, 094418 (2017).

[140] F. Körmann. *Magnetic Systems studied by First-Principles Thermodynamics*, PhD thesis. Paderborn: Paderborn University, (2011).

[141] D. Gambino, D. G. Sangiovanni, B. Alling, and I. A. Abrikosov. *Nonequilibrium ab initio molecular dynamics determination of Ti monovacancy migration rates in B*1 *TiN*, **Phys. Rev. B 96**, 104306 (2017).

[142] D. Gambino and B. Alling. *Lattice relaxations in disordered Fe-based materials in the paramagnetic state from first principles*, **Phys. Rev. B 98**, 064105 (2018).

[143] M. Ekholm, D. Gambino, H. J. M. Jönsson, F. Tasnádi, B. Alling, and I. A. Abrikosov. *Assessing the SCAN functional for itinerant electron ferromagnets*, **Phys. Rev. B 98**, 094413 (2018).

[144] D. G. Sangiovanni, J. Klarbring, D. Smirnova, N. V. Skripnyak, D. Gambino, M. Mrovec, S. I. Simak, and I. A. Abrikosov. *Superioniclike Diffusion in an Elemental Crystal: bcc Titanium*, **Phys. Rev. Lett. 123**, 105501 (2019).

[145] D. Gambino, M. Arale Brännvall, A. Ehn, Y. Hedström, and B. Alling. *Longitudinal spin fluctuations in bcc and liquid Fe at high temperature and pressure calculated with a supercell approach*, **Phys. Rev. B 102**, 014402 (2020).

[146] L. Casillas-Trujillo, D. Gambino, L. Ventelon, and B. Alling. *Screw dislocation core structure in the paramagnetic state of bcc iron from first-principles calculations*, **Phys. Rev. B 102**, 094420 (2020).

[147] M. Gharavi, D. Gambino, A. le Febvrier, F. Eriksson, R. Armiento, B. Alling, and P. Eklund. *High thermoelectric power factor of pure and vanadium-alloyed chromium nitride thin films*, **Materials Today Communications 28**, 102493 (2021).

[148] A. le Febvrier, D. Gambino, F. Giovanelli, B. Bakhit, S. Hurand, G. Abadias, B. Alling, and P. Eklund. *P-type behavior of CrN thin films by control of point defects*, **In Manuscript**.

[149] E. Koemets, I. Koemets, I. Leonov, D. Gambino, B. Alling, T. Fedotenko, S. Khandarkhaeva, S. Chariton, S. Dominijanni, C. Melai, G. Aprilis, N. Dubrovinskaia, K. Glazyrin, H.-P. Liermann, A. Rosa, I. A. Abrikosov, and L. Dubrovinsky. *Direct synthesis of carbonates from elements at extreme pressures and temperatures: evidence for oxidized carbon in Earth's lower mantle and unusual Fe-C-O chemistry*, **In Manuscript**.

[150] M. A. Brännvall, D. Gambino, R. Armiento, and B. Alling. *A machine learning approach for longitudinal spin fluctuation effects in bcc Fe at* T_C *and under Earth-core conditions*, **In Manuscript**.

[151] D. Gambino, J. Klarbring, and B. Alling. *Phase stability of Fe from atomistic spin dynamics coupled with ab initio moleculardynamics simulations and thermodynamic integration*, **In Manuscript**.

8 List of included articles and contributions

[I] **Nonequilibrium ab initio molecular dynamics determination of Ti monovacancy migration rates in B1 TiN.**
D. Gambino, D. G. Sangiovanni, B. Alling, and I. A. Abrikosov
Physical Review B ***96****, 104306 (2017)*
I took part in planning of the project, performed all the calculations, participated in the analysis of the results, and was responsible for writing the manuscript.

[II] **Lattice relaxations in disordered Fe-based materials in the paramagnetic state from first principles.**
Davide Gambino and Björn Alling
Physical Review B ***98****, 064105 (2018)*
I took part in planning of the project, implemented the code for performing relaxation, performed all the calculations, participated in the analysis of the results, and was responsible for writing the manuscript.

[III] **Assessing the SCAN functional for itinerant electron ferromagnets.**
M. Ekholm, D. Gambino, H. J. M. Jönsson, F. Tasnádi, B. Alling, and I. A. Abrikosov
Physical Review B ***98****, 094413 (2018)*
I did all the calculations, and took part in the analysis of the results.

[IV] **Superioniclike Diffusion in an Elemental Crystal: bcc Titanium**
D. G. Sangiovanni, J. Klarbring, D. Smirnova, N. V. Skripnyak, D. Gambino, M. Mrovec, S. I. Simak, and I. A. Abrikosov
Physical Review Letters ***123****, 105501 (2019)*
I helped in the set up of the calculations, participated in the analysis of the results, and commented on the manuscript.

[V] **Longitudinal spin fluctuations in bcc and liquid Fe at high temperature and pressure calculated with a supercell approach**
D. Gambino, M. A. Brännvall, A. Ehn, Y. Hedström, and B. Alling

Physical Review B ***102****, 014402 (2020)*
I took part in the conception and planning of the project, performed part of the calculations, analyzed the results, and wrote the manuscript.

[VI] **Screw dislocation core structure in the paramagnetic state of bcc iron from first-principles calculations**
L. Casillas-Trujillo, D. Gambino, L. Ventelon, and B. Alling
Physical Review B ***102****, 094420 (2020)*
I helped in the set up of the calculations and in the preliminary analysis of the results, and commented on the manuscript.

[VII] **High thermoelectric power factor of pure and vanadium-alloyed chromium nitride thin films**
M. A. Gharavi, D. Gambino, A. le Febvrier, F. Eriksson, R. Armiento, B. Alling, and P. Eklund
Materials Today Communications ***28****, 102493 (2021)*
I performed the calculations for the project and I wrote the theory part of the manuscript.

[VIII] **P-type behavior of CrN thin films by control of point defects**
A. le Febvrier, D. Gambino, F. Giovanelli, B. Bakhit, S. Hurand, G. Abadias, B. Alling, and P. Eklund
In manuscript
I jointly conceived the project, performed all calculations, and I was responsible to write the theory part of the manuscript.

[IX] **Direct synthesis of carbonates from elements at extreme pressures and temperatures: evidence for oxidized carbon in Earth's lower mantle and unusual Fe-C-O chemistry**
E. Koemets , I. Koemets , I. Leonov , D. Gambino , B. Alling , T. Fedotenko , S. Khandarkhaeva , S. Chariton , S. Dominijanni , C. Melai , G. Aprilis , N. Dubrovinskaia , K. Glazyrin , H.-P. Liermann , A.D. Rosa , I. A. Abrikosov , L. Dubrovinsky
In manuscript
I performed part of the calculations and wrote the related part of the manuscript.

[X] **A machine learning approach for longitudinal spin fluctuation effects in bcc Fe at $\mathbf{T_C}$ and under Earth-core conditions**
M. A. Brännvall, D. Gambino, R. Armiento, and B. Alling
In manuscript
I helped in the set up of the calculations and in the analysis of the results, and commented on the manuscript.

[XI] **Phase stability of Fe from atomistic spin dynamics coupled with ab initio molecular dynamics simulations and thermodynamic integration**

D. Gambino, J. Klarbring, and B. Alling
In manuscript
I jointly conceived the project, performed all calculations, and wrote the manuscript.

9 Related, not included publications

Effect of dispersion corrections on ab initio predictions of graphite and diamond properties under pressure.
I. Mosyagin, D. Gambino, D. G. Sangiovanni, I. A. Abrikosov, and N. M. Caffrey.
Physical Review B, **98**, 174103 (2018).

Papers

The papers associated with this thesis have been removed for copyright reasons. For more details about these see:

http://urn.kb.se/resolve?urn=urn:nbn:se:liu:diva-178214

FACULTY OF SCIENCE AND ENGINEERING

Linköping Studies in Science and Technology,
Dissertation No. 2159, 2021
Department of Physics, Chemistry and Biology (IFM)

Linköping University
SE-581 83 Linköping, Sweden

www.liu.se

LINKÖPING
UNIVERSITY